論文 / 著書情報
Article / Book Information

題目(和文)	オーステナイト系耐熱鋼のTCP Laves相による長時間クリープ強度に対する新概念
Title(English)	Novel Concept for Long-Term Creep Strengthening by TCP Laves Phase in Austenitic Heat Resistant Steels
著者(和文)	IMANUELTARIGAN
Author(English)	IMANUELTARIGAN
出典(和文)	学位:博士（工学）, 学位授与機関:東京工業大学, 報告番号:甲第9425号, 授与年月日:2014年3月26日, 学位の種別:課程博士, 審査員:竹山　雅夫,中村　吉男,熊井　真次,藤居　俊之,里　達雄,寺田　芳弘
Citation(English)	Degree:Doctor (Engineering), Conferring organization: Tokyo Institute of Technology, Report number:甲第9425号, Conferred date:2014/3/26, Degree Type:Course doctor, Examiner:,,,,,
学位種別(和文)	博士論文
Type(English)	Doctoral Thesis

Novel Concept for Long-Term Creep Strengthening by TCP Laves Phase in Austenitic Heat Resistant Steels

A Dissertation for the Degree
Doctor of Engineerring

By
Imanuel Tarigan

Supervised by
Masao Takeyama

Department of Metallurgy and Ceramics Science
Tokyo Institute of Technology

March 2014

Contents

Chapter 1

General Introduction

1.1 Background

In the 21st century, the world faces two major challenges of overcoming the energy crisis and at the same time preventing global warming due to CO_2 pollution. The rapid economic growth and increasing population of the emerging countries have significantly increased the demand of electric power. The global need of electricity is estimated to become double in the next 30 years, growing at annual rate of 2.4% [1]. Unfortunately, 70% of this total energy is still provided by fossil-fueled thermal power generation, which emits the largest proportion of CO_2 gas into the environment [2]. While there are many renewable energy sources that would make substantial reductions in CO_2 emission, most of these energy systems have low-energy flux intensity compared to fossil-fueled plants [3]. The cost of implementation of this technology will be much higher than that of the fossil-fueled plants and thus it may not become the best economical solution at the present.

One possible solution receiving attention worldwide recently is to increase the energy efficiency of coal-fired power plant. In power plant design, this improvement of energy efficiency could be achieved by increasing the operating temperature and pressure of the steam. In Japan, the recent target is to develop the advanced ultra supercritical (A-USC) thermal power plant operated at 35 MPa in pressure and 973 K in temperature, as shown in **Figure 1-1**. It is estimated that under this condition the efficiency can be raised into 48% from the current 43%, with considerable amount reduction of CO_2 emission [4].

To be able to be operated in the A-USC condition, the power plants require materials with 10^5 h creep rupture strength of more than 100 MPa at 973K. The best candidate materials for this condition are the metals with face-centered cubic (fcc) structure since it has high stability at high temperatures. **Figure 1-2** shows the allowable stress of current commercial heat resistant alloys at high temperatures, along with the requirements for the A-USC [5-7]. None of the current commercial austentic heat resistant steels are strong enough to meet the requirements. Even the 347 HTB steel, which is considered one of the strongest among these steels, can only be used at stress less than half that required by the A-USC. On the other hand, the Ni-based superalloys such as Inconel-740, which are strengthened by stable intermetallic phases, are strong enough to meet the requirement, but they are very expensive. Thus, as far as the cost performance is concerned, the best way to solve this issue is to develop new austenitic heat resistant steels capable to be used at A-USC conditions.

1.2 Design concept of austenitic heat resistant steels strengthened by intermetallics

The main reason why the current austenitic heat resistant steel has low creep rupture strength is the poor stability of metallic carbides that are used as strengthener in these steels. The metallic carbides readily coarsen at high temperature and cause rapid drop in strength at long-term application. On the other hand, the Ni-based superalloys use intermetallic compounds such as Ni_3(Al, Ti)-γ', which have higher thermal stability than the carbides. It becomes our great interest to know whether the intermetallics strengthener

can also be used in the austenitic steels to improve their creep rupture strength.

Figure 1-3 shows compositions of several commercial austenitic heat resistant steels and Ni-based superalloys in Fe-Ni-Cr ternary diagram at 1473K [8]. Along 20 at% Cr., all of the Ni-based superalloys that strengthened by stable intermetallic compounds are located on the Ni-rich side, while austenitic heat resistant steels with carbides strengthener are located on the Fe-rich side. It is noteworthy that there are no austenitic heat resistant steels with intermediate compositions between Fe-rich and Ni-rich sides. This is the composition region where intermetallic Fe_2M Laves phase forms. It is generally believed that the Laves phase is detrimental to creep for causing embrittlement and thus it is common practice in steel design to avoid using compositions where this phase can form.

Takeyama [9] has suggested that the Fe_2M TCP (Topologically close-packed) compounds are potential strengthener over carbides because it has high thermal stability at elevated temperatures. If it is possible to make the Laves in equilibrium with the matrix at the service temperature, it will give a significant improvement for the creep strength of the steel. **Figure 1-4** shows a schematic illustration how to design an alloy using Laves phase as strengthener in Fe-Ni-M ternary systems at elevated temperature [8,9]. In the Fe-rich corner, there is a large $\gamma+Fe_2M$ two-phase region neighboring to the three-phase tie triangle of $\alpha+\gamma+Fe_2M$. Since the M element also forms GCP phase of Ni_3M in the Ni-rich side, the three-phase tie triangle of $\gamma+Fe_2M+Ni_3M$ showed by dotted line would exist in this system. In order to use Fe_2M Laves as a strengthener, the Fe_2M single-phase region should be extended toward equi-Nb concentration, which will enlarge the $\gamma+Fe_2M$ two phase region into the direction shown by the arrow. The existence of large $\gamma+Fe_2M$ region is very important to control the morphology of the precipitated Laves phase in γ matrix.

Based on phase equilibrium studies in Fe-M binary systems [10-12], the Fe_2M phases can be classified into three types as shown in **Fig. 1-5**:

1. Stable up to melting temperature and in equilibrium with γ-Fe only at high temperature. The typical M elements of this type are Zr, Hf, Nb and Ta.
2. Stable up to melting temperature and never in equilibrium with γ-Fe at any temperature. The typical M element of this type is Ti.
3. Decomposes into α and Fe_7M_6 (μ) phases below the melting temperature. The typical M elements of this type are Mo and W.

Note that highest α stabilizing elements among them are Mo and W, which corresponds to type 3. Therefore, based on these studies, the Fe_2Nb (ε) phase with the C14 structure is the most promising to be used as a strengthener among the other transition metals since it has high congruent melting temperature (1914 K) and a wide composition homogeneity region and equilibrium with γ-Fe above 1228 K.

Based on these concepts, the ternary phase equilibria of Fe-Ni-Nb systems at elevated temperature has been systematically examined. **Figure 1-6** shows the isothermal section of Fe-Ni-Nb systems at 973K, which was calculated by using the ternary interaction parameters of each elements for reproducing their isothermal sections at 1473 and 1373 K.

There is wide γ+ε+δ three-phase coexisting region in this system, which stretched out toward Fe-rich region [14-17]. A terminal composition of γ-Fe phase in the three-phase coexisting region is Fe-19%Ni-0.04%Nb. These results give an indication of the possible composition range to design austenitic steels strengthened by Fe_2Nb Laves phase.

In considering the Fe_2Nb as a strengthener for austenitic heat resistant steels, Cr addition is necessarily required, thus the phase diagram study was extended into a quartenary system with the addition of 20 at.% Cr. **Figure 1-7** shows calculated vertical section of quartenary Fe-Ni-Cr-Nb systems cut along 20 at.% Cr with 1-3 at.% Nb compositions [17]. At 1 at.% Nb, the γ+ε+δ three-phase coexisting region exists at Ni-rich region (more than 26 at.% Ni) and temperature of 950 ~ 1150 K. By increasing the Nb content, this region further expands toward higher temperature and Ni concentration direction. At Ni concentration of 30 at.%, the supersaturation of Nb at 973K slightly increases with increasing Nb, however at 3 at.% Nb the γ single phase region could not be achieved. Therefore, in order to have precipitation of Laves phase in γ matrix at 973K, Fe-20Cr-30Ni-2Nb (at.%) was selected as a model steel.

1.3 Precipitation Behavior of Fe-20Cr-30Ni-2Nb Austenitic Heat Resistant Steel

Figure 1-8 shows the transmission electron micrographs (TEM) showing the precipitates in the Fe-20Cr-30Ni-2Nb steel after aged for 973K for 1200 h. The bright field image (Fig. 1-8(a)) reveals two different precipitates, one with large elongated shape (domain A) and the other with fine stick-shaped morphology (domain B). Selected area diffraction pattern (SADP) analysis was done on each of the precipitates by using **B**=110 of γ matrix. Figure 1-8(b) shows the diffraction pattern in the domain A, which was identified as superposition of **B**=$10\bar{1}0$ diffraction of Fe_2Nb (ε) with hexagonal C14 structure on the **B**=110 diffraction of γ. The orientation relationship (OR) between the precipitate and the matrix in this domain can be described as follow:

$$[110]_\gamma \parallel \langle 10\bar{1}0 \rangle$$
$$\{111\}_\gamma \parallel (0001)$$

Figure 1-8(b) shows the diffraction pattern in the domain B, which shows superlattice diffraction on the 110 pattern with an OR of $\{001\}_\gamma \parallel (001)_{\gamma''}$ and $\langle 010 \rangle_\gamma \parallel [010]_{\gamma''}$. Thus, the precipitate shown in B-domain is clearly the Ni_3Nb-γ" ($D0_{22}$) phase. These results confirm our calculated phase diagram that predicts the precipitation of both intermetallics TCP Fe_2Nb Laves and GCP Ni_3Nb-γ" (metastable) phases in the Fe-20Cr-30Ni-2Nb steel at 973K.

Figure 1-9 (a)-(d) show the microstructures of Fe-20Cr-30Ni-2Nb at.% steel after aged at 1073K up to 3600 h. Geometrically Close-Packed (GCP) Ni_3Nb-γ" phase ($D0_{22}$) precipitates coherently within grains, in addition to the precipitation of the Laves phase.

After 240h, the metastable γ" phase starts to transform into stable but coarse Ni_3Nb-δ ($D0_a$) phase (Fig. 1-9(d)). The microstructure at 3600 h aging shows fully precipitation of Ni_3Nb-δ precipitates at grain interior that has lower precipitation density compared to fine γ" precipitates at 240 h. This confirms the calculated Fe-Cr-Ni-Nb quoternary phase diagram at 973 K.

On the other hand, at 1073 K only Fe_2Nb-ε Laves phase finely precipitates at grain boundaries (GB) and grain interior (GI) of the steel, as shown in Fig. 1-9(e)-(h). The precipitation at GB continues to increase with increasing aging time up to 1200 h, while at GI it becomes saturated after 240h. At 3600h, the microstructure consists of high fraction of Laves phase at GB and fine, homogenous precipitation on γ-matrix (Fig. 1-9 (d)). The fine morphology of the Laves phase even after long period of aging, demonstrates the stability of this phase at high temperature.

Based on these microstructure observations up to 1223 K and 3600 h, we have constructed the Time-Temperature-Precipitation (TTP) diagram as shown in **Fig. 1-10**. The precipitation start (Ps) line of Laves phase at GB always precedes that in GI. Both lines show "c"-shaped curve with the nose temperature of about 1200 K. At 1073K, only Laves phase precipitates at both GB and GI, with the Ps line of GI lies about 1 order magnitude behind that of GB. At 973K, the γ" simultaneously precipitates in GI along with the precipitation of Laves at GB. After 500 h of aging, the γ" starts to transform into δ phase. The Ps line of Laves at GI is significantly delayed at this temperature due to the precipitation of the Ni_3Nb phases, which reduces the supersaturation of Nb in γ matrix.

In order to examine quantitatively the precipitation kinetics of Laves phase at grain boundary, the area fraction of Laves phase over the total grain boundary area, termed as area fraction (ρ), was measured. **Figure 1-11** shows the change in ρ of Laves phase with aging time at temperature of 973–1173K. At 1173K, the GB Laves starts to precipitate shortly after few seconds of aging and continues to increase until becomes constant at 67% of ρ after 10h. On the other hand, at 1073K, the GB Laves continues to increase even after 3600 h of aging, with ρ of 54%. The precipitation kinetics in 973K is slower to that of 1073 K but shows similar trend where the Laves phase continues to increase even after 3600 h, with ρ of 42%.

Figure 1-12 shows the change in hardness of grain interior of the steel with aging time at temperature of 973-1173K. The hardness change at 1173K and 1073K shows similar trends, where it starts to increase gradually after few seconds and then reaches 1.8 GPa at 10 h and becomes constant with further aging. However, at 1173K, the hardness slightly decreases after 240 h aging, which might be due to coarsening of the Laves phase. On the other hand, at 973 K, the hardness starts to increase rapidly after 10 h of aging until reaches 2.2 GPa at 1000 h and it becomes constant with further aging. These results indicate that Fe_2Nb precipitates within GI are not effective as a strengthener for the steel.

Figure 1-13 shows a change in solid solution of Nb in γ matrix with aging at 1073K. The concentration of Nb remains almost unchanged till 24 h aging, but afterwards it

decreases significantly from about 1.8 to 1.2 at.% at 240 h. At 1200 h , the concentration of solute Nb become less than 0.7 at.%. The concentration near the GB shows similar trend to that at center of grain up to 3 h of aging. However, it decreases at faster rate with further aging up to 1200h. It is in good agreement with the TTP diagram that precipitation of Laves phase at gain boundaries is much faster than that in grain interior, which results much higher consumption of Nb around this area. The difference in concentration between these 2 regions might also become the driving force for diffusion of solute Nb into the grain boundaries, which can explain the retardation of precipitation of Laves phase at grain interior after 24 h of aging, as suggested by hardness test results in **Fig. 1-12**.

1.4 Creep Behavior of Fe-20Cr-30Ni-2Nb Steel at 973K

The creep behavior of the model steel strengthened by Laves phase has been examined under stresses of 120, 140 and 200 MPa [18]. **Figure 1-14** shows the creep rate-time curve of the solution treated steel at 973 K. Regardless of the stress level, the creep rate decreases by several orders of magnitude until reaching a minimum creep rate of 10^{-6} h^{-1} after several hundreds of hours. After the minimum, the creep rate increases significantly at 200 MPa stress, leading to rupture at 340 h. By reducing the applied stress into 140 MPa, the creep acceleration stage is extended for more than 1000 h, which increases the rupture life into 1600 h. At 120 MPa creep test, the creep rate at the acceleration stage becomes constant for almost half of its life (2000 h), which substantially extends the rupture time into 4594 h.

Figure 1-15 shows the microstructures of the steel after creep rupture tests at (a) 200 MPa, (b) 140 MPa and (c) 120 MPa at temperature of 973 K. In 200 MPa ruptured specimen, very fine γ" precipitates were observed within grain interior, which explains the significant decreases of the creep rate during transient stage of creep. The fine γ" transforms into coarse δ phase at longer period of creep, as observed in the microstructures of the ruptured specimens at 140 and 120 MPa. The transformation causes the precipitation density of the grain interior to decrease and thus accelerates the creep rate. Interesting point to note that although the precipitation density within grain of 120 MPa ruptured specimen is less than that tested at 140 MPa, the precipitation density of Laves phase at grain boundary is much higher. These results strongly suggest that the retardation of creep rate at the acceleration stage, which results in extending the rupture life, is mainly due to the precipitation of Laves phase at grain boundary.

Figure 1-16 shows the stress-rupture time curves of solution treated Fe-20Cr-30Ni-2Nb steel, in comparison with the reported results of Ni-base Inconel 740 alloy and the conventional 347 type austenitic heat resistant steel [19, 20]. The predicted rupture strength at 10^5 of our model steel at 973 K is about 80 MPa. Although it is still not strong enough for the A-USC, it is much superior to that of the 347 steel that strengthened by metallic carbides. These results give a strong indication of the effectiveness of the GB Laves phase to increase the creep strength of austenitic heat resistant steels. Takeyama, et.

al. attributed the effect to "*grain boundary precipitation strengthening*" by the Laves phase [13]. However, how can the GB Laves phase increase the creep rupture strength? which is yet unknown. Thus, further researches should be needed to reveal the role of GB Laves phase in creep strengthening mechanism.

1.5 Objective

For the further development of austenitic heat resistant steel by using Laves phase, it is important to fundamentally understand a role of grain boundary Laves phase in creep strengthening mechanism. Therefore, the main objective of this study is to reveal the grain boundary precipitation strengthening mechanism by the Laves phase.

In order to achieve this objective, it is necessary to examine the creep behavior under different precipitation of GB Laves and different stress and temperature conditions of the creep tests. It is therefore important to find out how to control the precipitation of Laves phase at grain boundaries. To clarify the detailed strengthening mechanism, the characterization of dislocation substructures and creep deformation behavior is also required.

It is our hope that the results obtained in this study can give a new perspective to the design for the long-term creep strength of austenitic heat resistant steels.

1.6 Outline

The flow chart of the present thesis is shown in **Fig. 1-17.**

Chapter 1 is "General Introduction" where backgrounds, previous results as well as the objectives of the research are described. The alloy design concept by using intemetallic phase and the reason why C14 Fe_2Nb Laves phase was selected as strengthener are briefly explained. The previous works on the on the model steel employing the Laves phase are also provided. The emphasis of this chapter is to introduce the significant effect of grain boundary Laves phase on long-term creep rupture strength. Then, the objective and outline of the thesis are explained.

Chapter 2 is "Precipitation Behavior and Morphology Control of Fe_2Nb Laves Phase on Grain Boundary". In this chapter the effectiveness of boron as a tool to increase the precipitation of GB Laves phase is examined. The method to control precipitation of GB Laves through aging treatments is also described. Morphology of Laves phase in three dimensions at grain boundaries is examined by means of tilting experiments in FE-SEM.

Chapter 3 is "Effect of Grain Boundary Laves Phase on Creep Behavior". In this chapter the confirmation of the effect of GB Laves phase in increasing creep rupture strength is described by means of creep observation of steels with high precipitation of GB Laves phase at 973 K and 1073 K. The evaluation of creep exponent of solution treated steels at 973K is also discussed.

Chapter 4 is "Creep Strengthening Mechanism by Grain Boundary Laves Phase". In this chapter the creep behavior of pre-aged steels at 973K and 1073K is analyzed.

Particular attention has been paid on the effect of area fraction of GB Laves phase on creep resistance. Creep strengthening mechanisms by GB Laves phase is proposed based on the creep test results as well as dislocation analysis of creep interrupted specimens. Classical theory of creep mechanism is also reviewed based on the creep test results obtained in this chapter.

Chapter 5 is "Role of Grain Boundary Laves Phase on Deformation Mechanism at Accelerating Stage". In this chapter the application of grain boundary precipitation strengthening (GBPS) concept at accelerating stage is reviewed. New approach to observe microstructures at accelerating stage by means of local observation of the ruptured samples is described. Local microstructure change with strain is the focus attention of analysis in this chapter. The governing deformation mechanism in creep of model steel is proposed based on the analysis results.

Chapter 6 is "Concept of Grain Boundary Precipitation Strengthening Mechanism". In this chapter the engineering application of the strengthening mechanism concept by Laves phase is discussed. Future development of austenitic heat resistant steels based on the concept is also proposed.

Chapter 7 is "General Conclusions". All results gained from this research are summarized in this chapter. Future plans for this research is briefly discussed.

References

[1] World Energy Outlook 2008, www.worldenergyoutlook.org.

[2] http://www.toshiba.co.jp/env/en/energy/index.htm.

[3] J. A. Fay, D. S. Golomb, *Energy And The Environment*, Oxford University Press, New York, pp. 4-5, 2002.

[4] F. Masuyama: Report of JSPS 123rd Committee on Heat-Resisting Materials and Alloys, 48, pp. 3 (2007)

[5] R. Viswanathan et al., Proc. of the 2nd Regional Conference on Energy Technology Towards a Clean Environment, Phuket, Thailand, (2003).

[6] NRIM Creep Data Sheet, 1987, No. 5B.

[7] NRIM Creep Data Sheet, 2000, No. 6B.

[8] M. Takeyama, *Mater. Sci. Forum*, 539-543, 3012, 2007.

[9] M. Takeyama: Report of JSPS 123rd Committee on Heat-Resisting Materials and Alloys, **45** (2004), p. 51.

[10] M. Takeyama, N. Gomi, S. Morita, T. Matsuo: MRS Symp. Proc. Vol. 842 (2005), p.461.

[11] S. Ishikawa, N. Gomi, T. Matsuo and M. Takeyama: Report of JSPS 123rd Committee on Heat-Resisting Materials and Alloys, 46 (2005), p.25.

[12] J. L. Murray, Phase diagrams of binary titanium alloys, ASM, Metals Park (1987).

[13] M. Takeyama: Nishiyama Memorial Lecture, No. 194-195, ISIJ (2008), pp. 1-23.

[14] Y. Hasebe, K. Hashimoto, M. Takeyama, J. Jpn. Inst. Met., 75(4), 265 (2011).

[15] Y. Hasebe, K. Hashimoto, M. Takeyama, Mater. Res. Soc. Symp., **1295**, 171 (2011).

[16] T. Sugiura, S. Ishikawa, T. Matsuo and M. Takeyama: Materials Science Forum, 561-565, 435 (2007).
[17] Y. Hasebe: Master Thesis, Tokyo Institute of Technology (2011).
[18] N. Hashizume: Master Thesis, Tokyo Insitute of Technology (2008).
[19] H. Tanaka, M. Murata, K. Kamihara, M. Yamazaki, K. Kimura, H. Abe: Report of JSPS 123rd Committee on Heat-Resisting Materials and Alloys, 47 (2006), p.31.
[20] Special Metals: Technical bulletin, www.specialmetals.com.

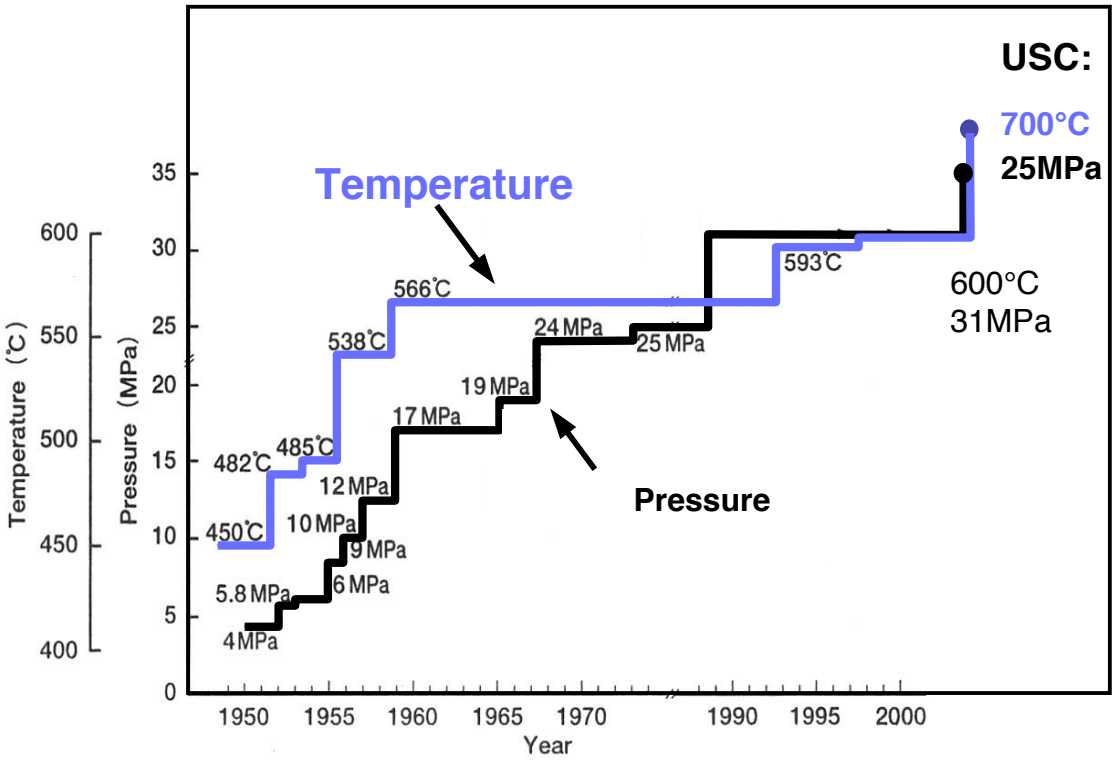

Fig. 1-1 Trend of inlet steam condition of thermal power plants in Japan.

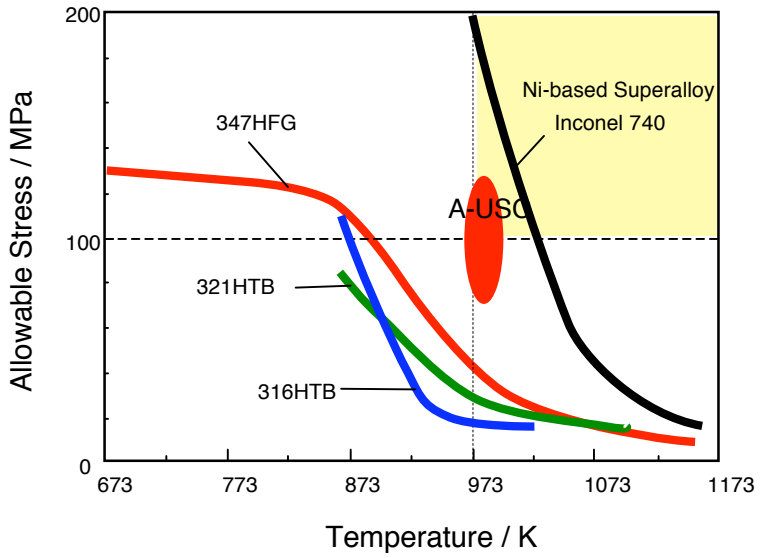

Fig. 1-2 Allowable Stress of commercial austenitic heat resistant steels and Inconel 740. [1,2]

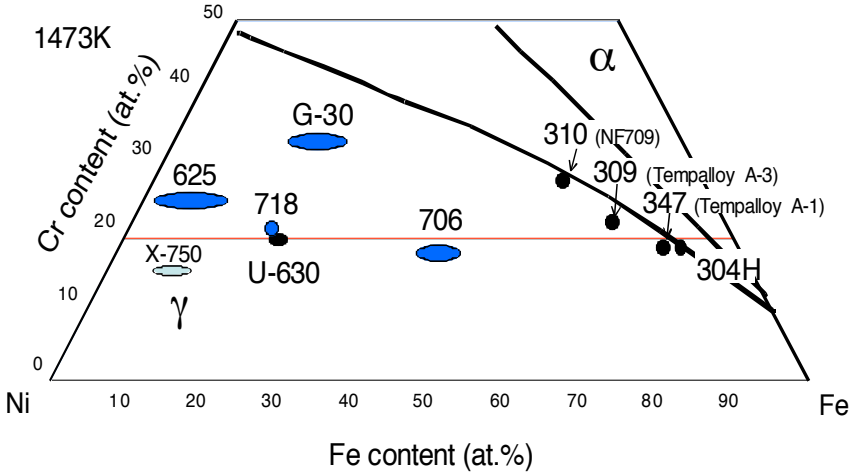

Fig. 1-3 Composition of commercial austenitic steels and Ni-based alloys plotted at isothermal section of Fe-Ni-Nb ternary system at 1473 K.

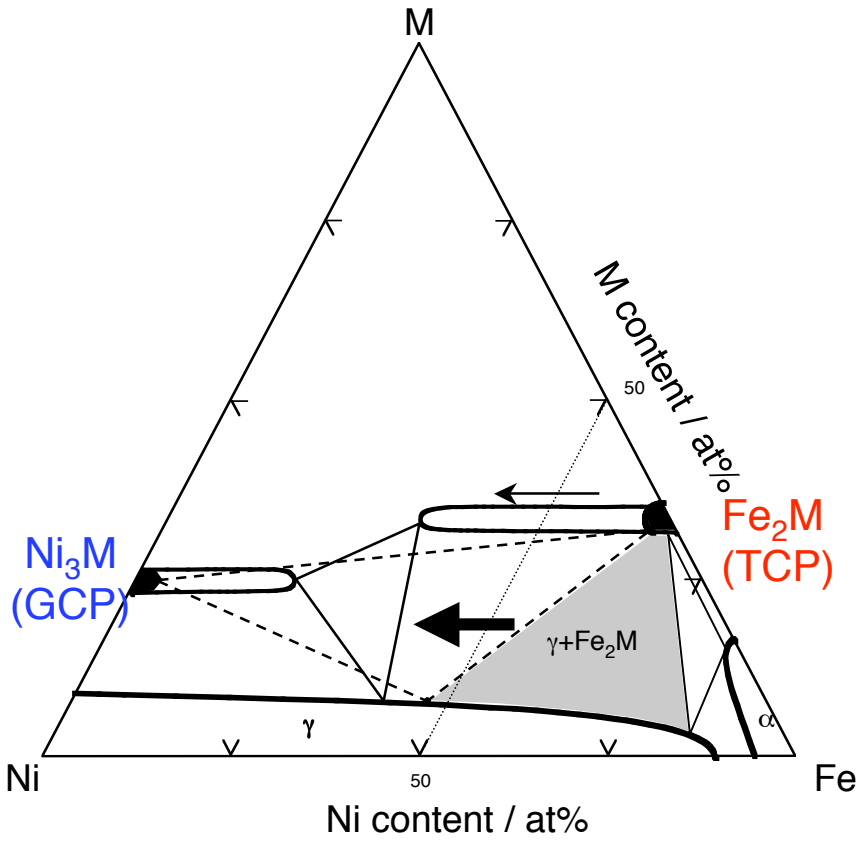

Fig. 1-4 Fe-Ni-M ternary phase diagram for the design of heat resistance austenitic steel strengthened by intermetallic compounds (GCP and TCP).

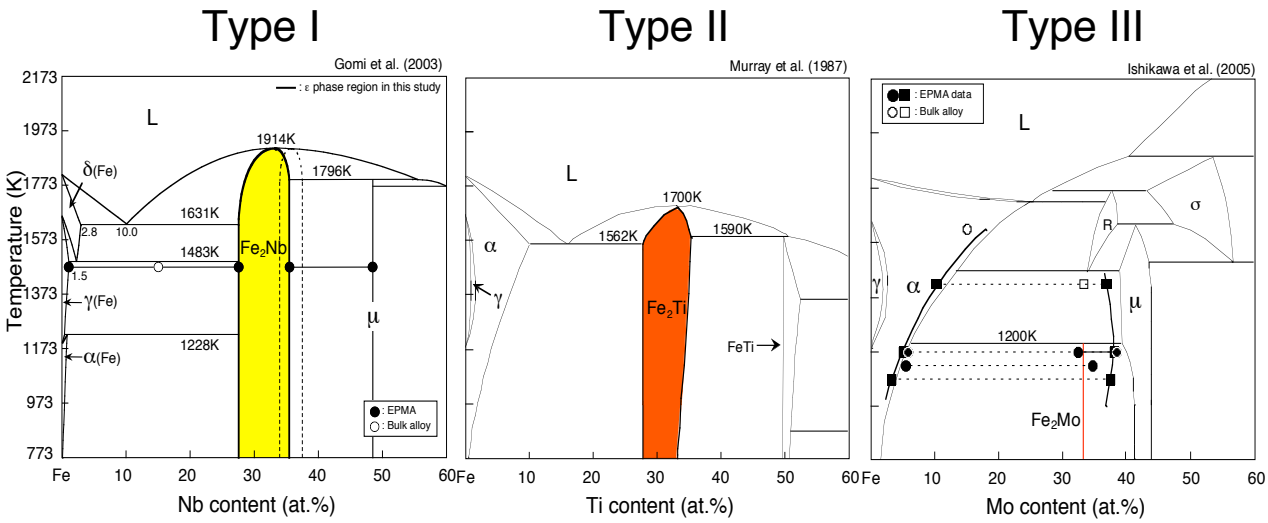

Fig. 1-5 Classification of Fe-M Laves phases based on binary phase diagrams.

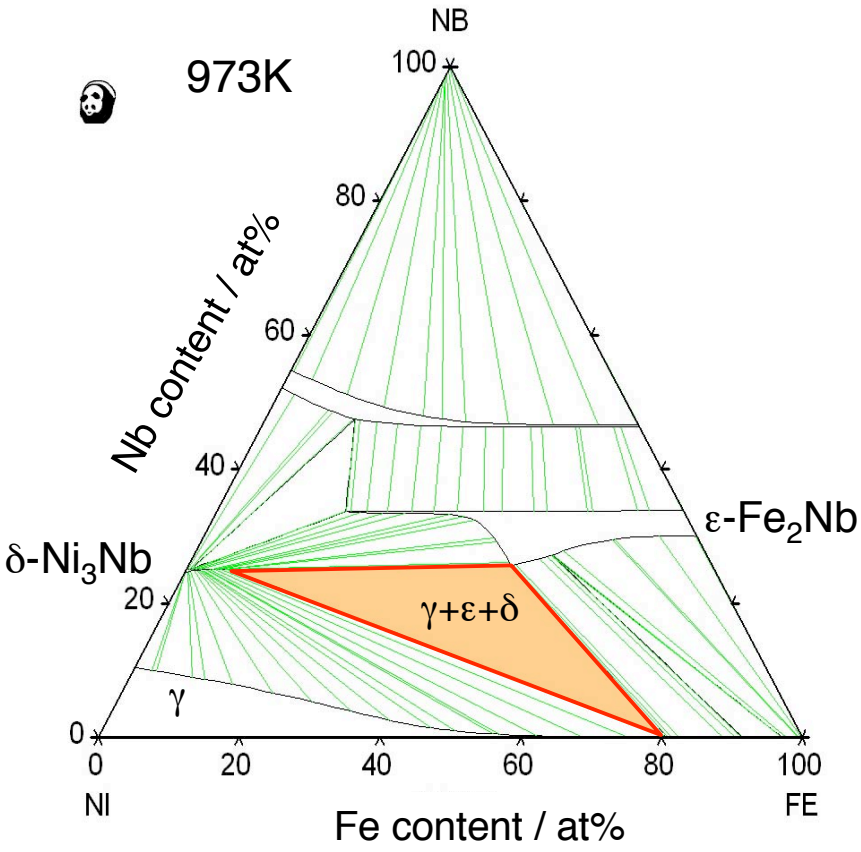

Fig. 1-6 Calculated isothermal section of Fe-Ni-Nb ternary system at 973K.

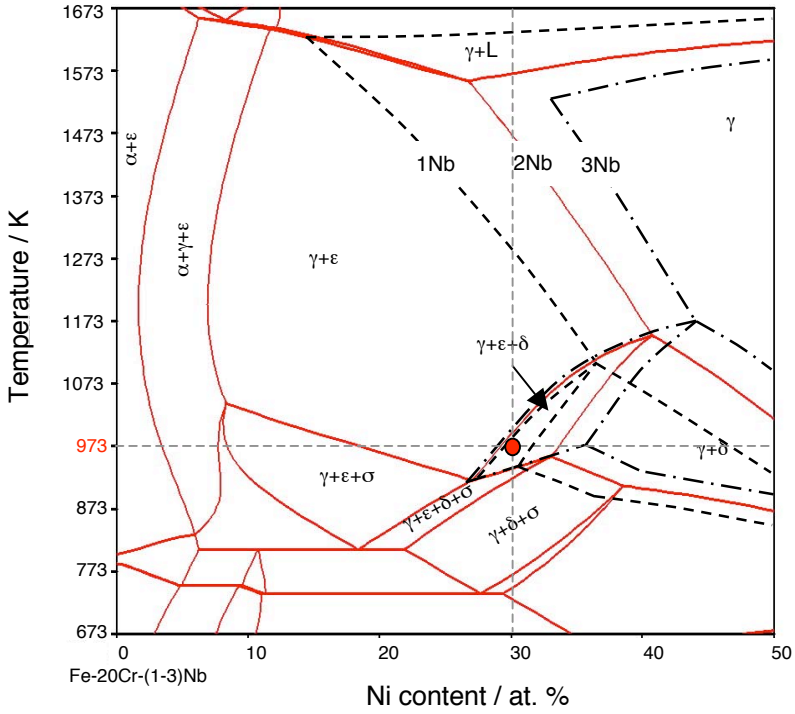

Fig. 1-7 Calculated vertical section of quarternary Fe-Ni-Cr-Nb system cut along Fe-Ni-20Cr-(1-3)Nb.

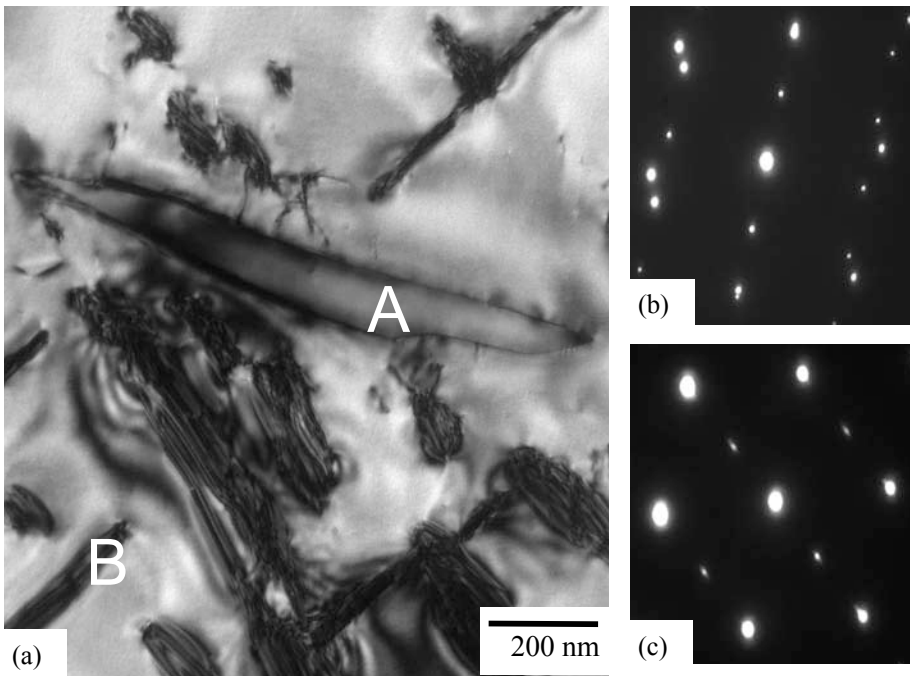

Fig. 1-8 Transmission electron micrographs of Fe-20Cr-30Ni-2Nb steel after aging at 973K for 1200h (a) Bright Field Image with **B**=110_{γ}, (b) SADP taken from A domain (**B**=110_{γ} // 1010_{ε}), (c) SADP taken from B domain (**B**=110_{γ} // $110_{\gamma''}$).

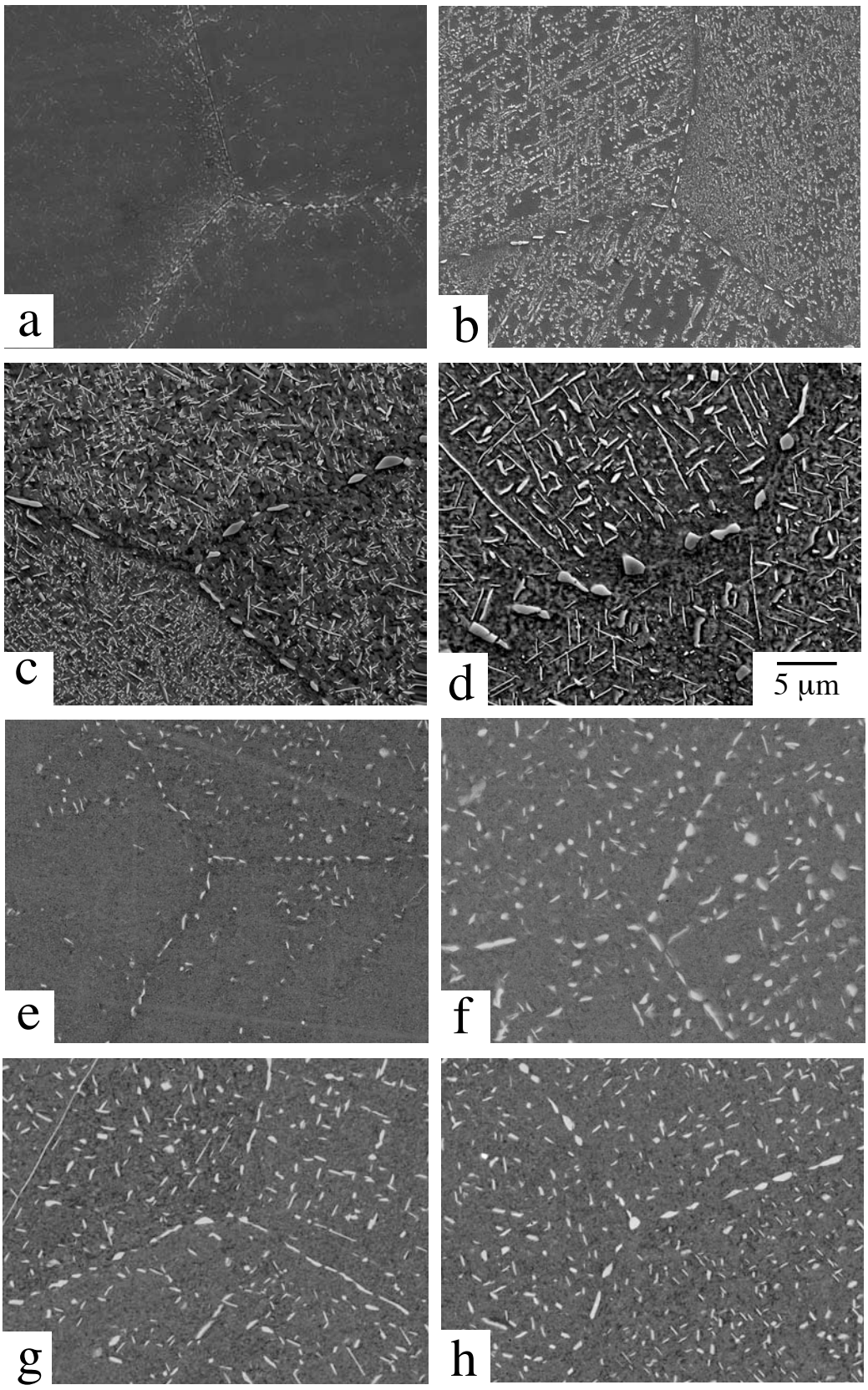

Fig. 1-9 Microstructures of Fe-20Cr-30Ni-2Nb steel aged at (a) 973 K / 24 h, (b) 973 K / 240 h, (c) 973 K / 1200 h, (d) 973 K / 3600 h, (e) 1073 K / 24 h, (f) 1073 K / 240 h, (g) 1073 K / 1200 h, (h) 1073 K / 3600 h.

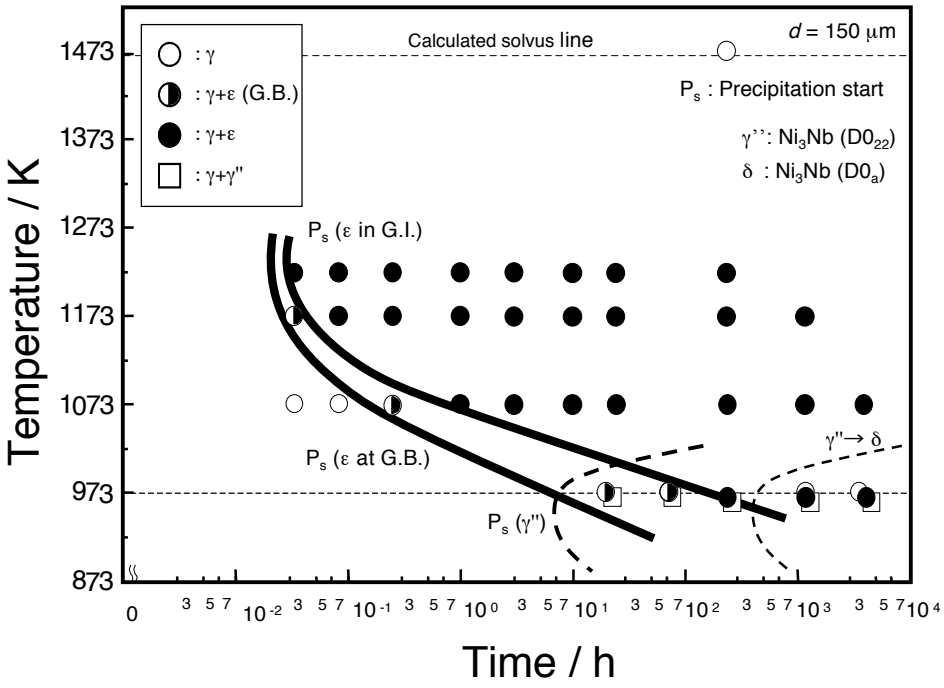

Fig. 1-10 TTP diagram of Fe-20Cr-30Ni-2Nb steel.

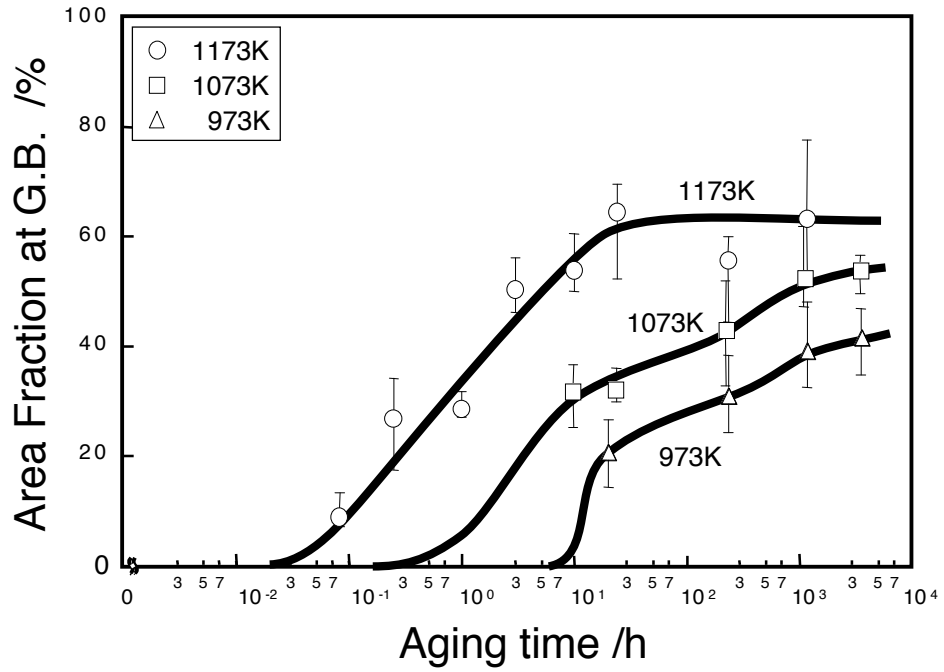

Fig. 1-11 Change in area fraction of Fe_2Nb Laves phase at grain boundary with aging time.

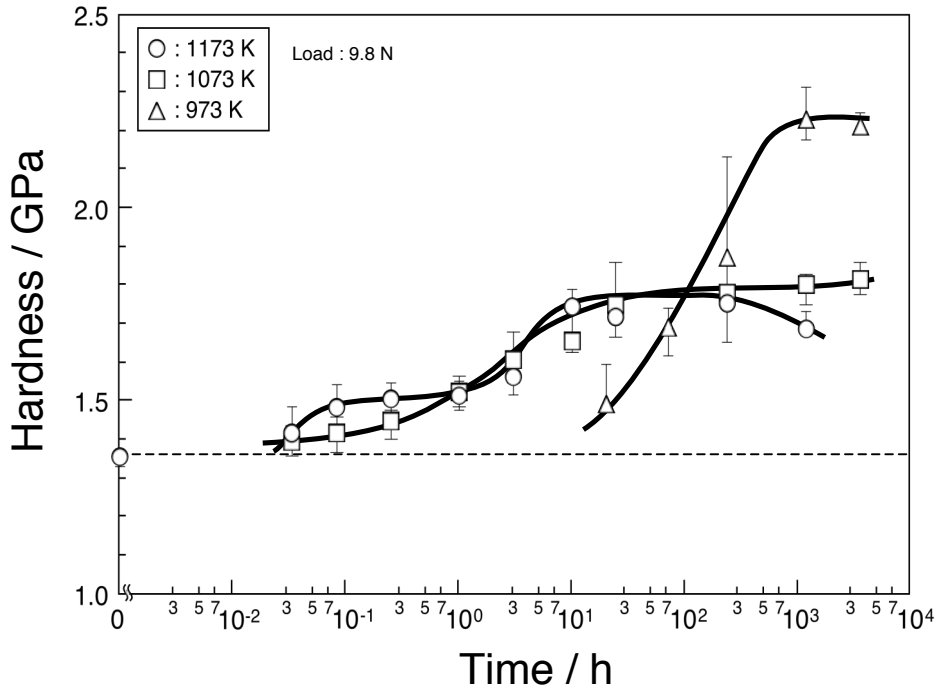

Fig. 1-12 Change in grain interior hardness of Fe-20Cr-30Ni-2Nb steel during aging.

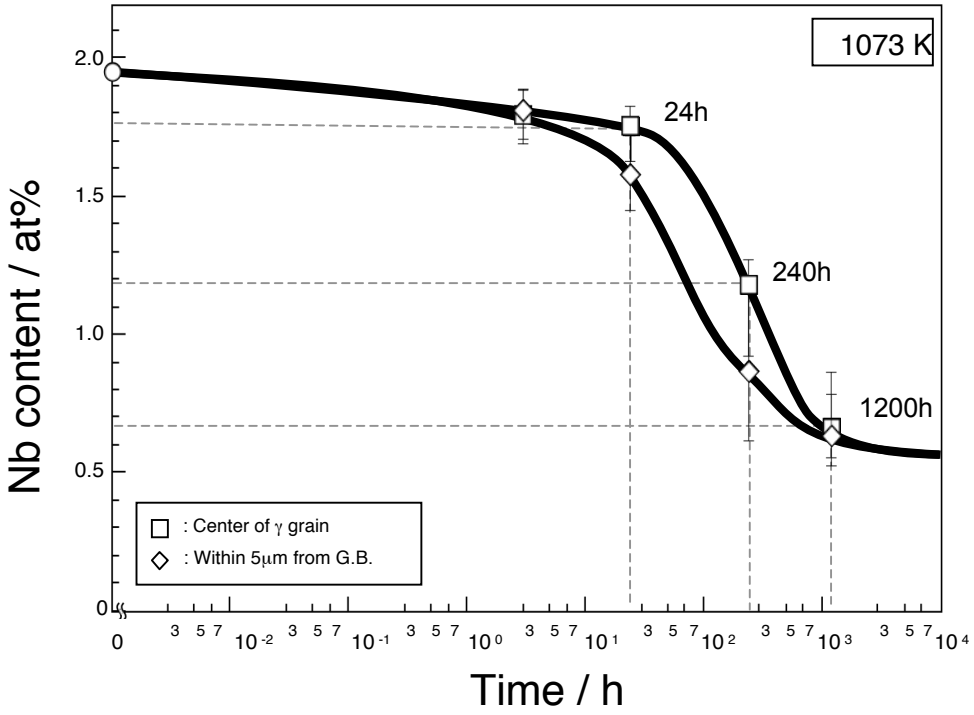

Fig. 1-13 Change in solute Nb content in γ matrix of Fe-20Cr-30Ni-2Nb steel with aging at 1073K.

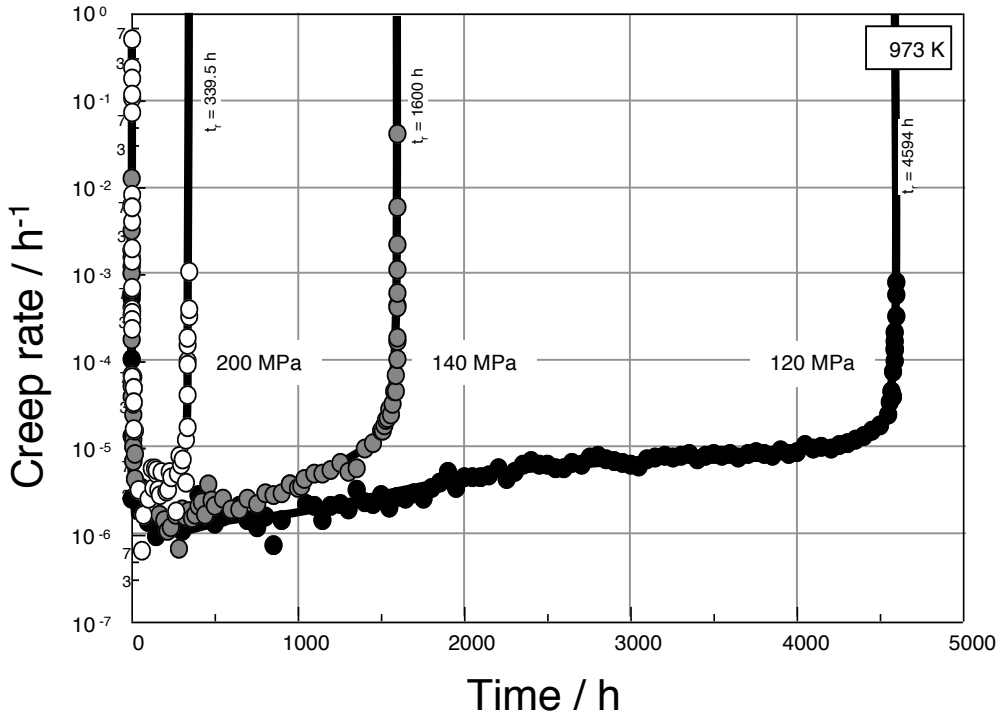

Fig. 1-14 Creep rate / time curves at 973 K / 200 MPa, 140 MPa and 120 MPa of solution-treated base steels(linear).

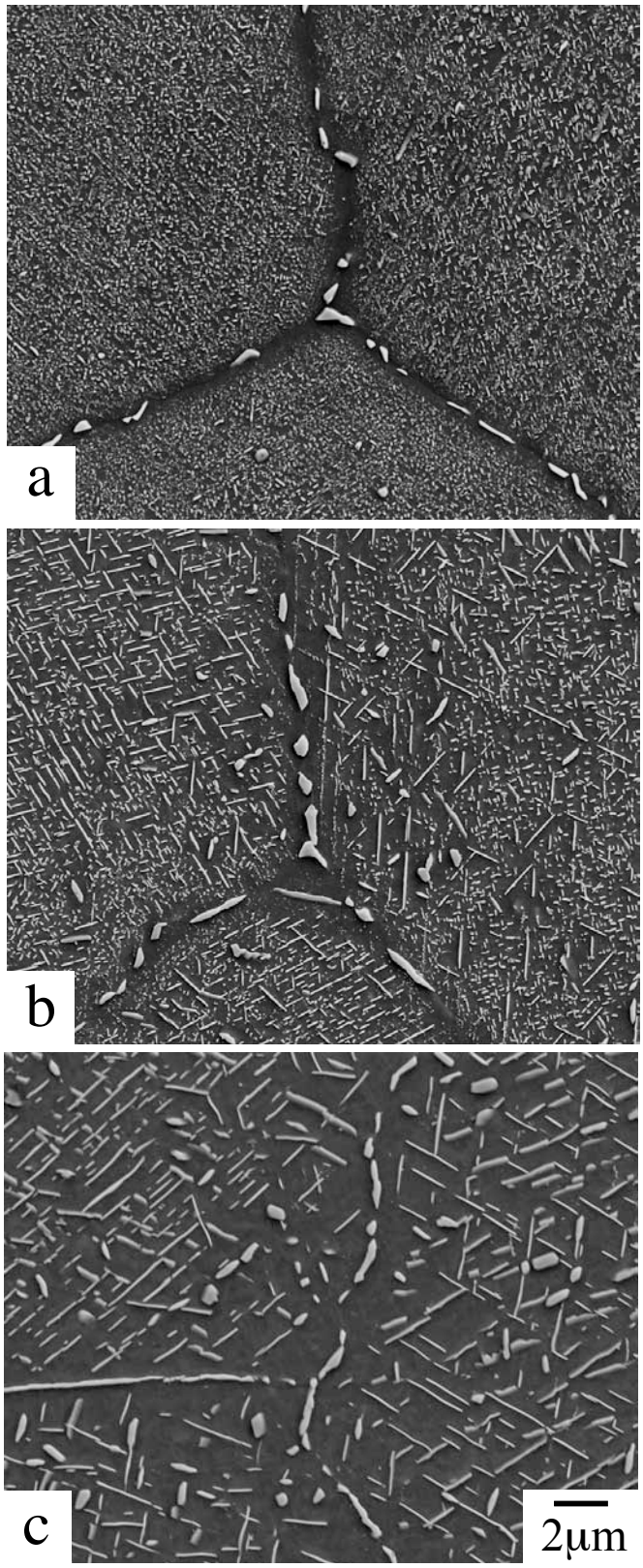

Fig. 1-15 Microstructure of the solution-treated Fe-20Cr-30Ni-2Nb steel creep ruptured at 973 K : (a) 200MPa, (b) 140MPa, and (c) 120MPa.

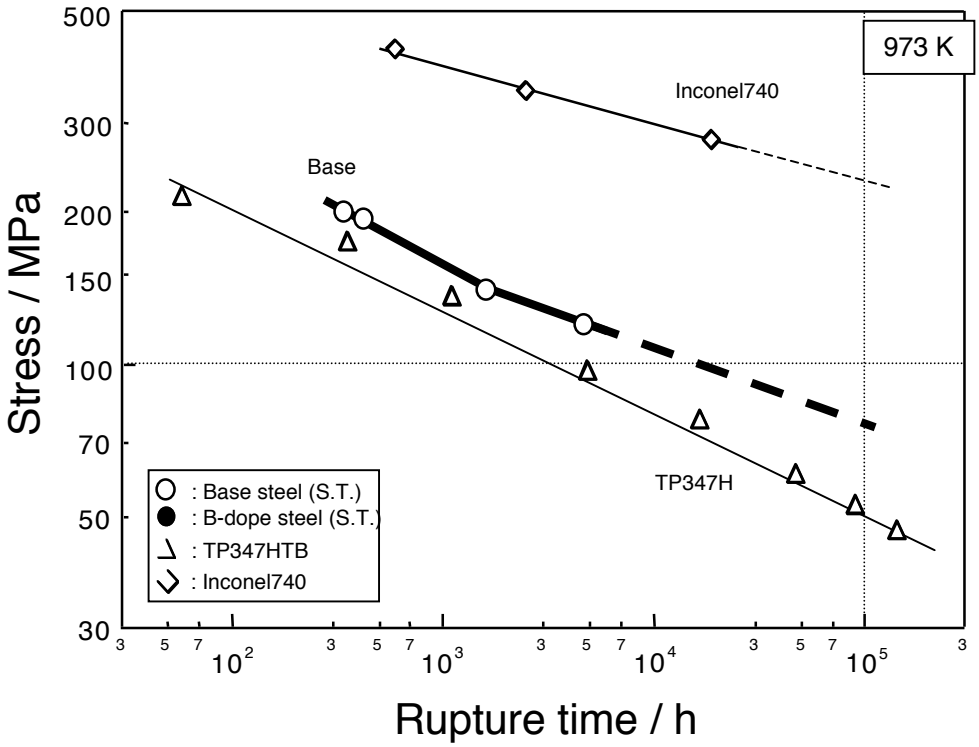

Fig. 1-16 Stress / rupture time curve at 973 K of Fe-20Cr-30Ni-2Nb steel.

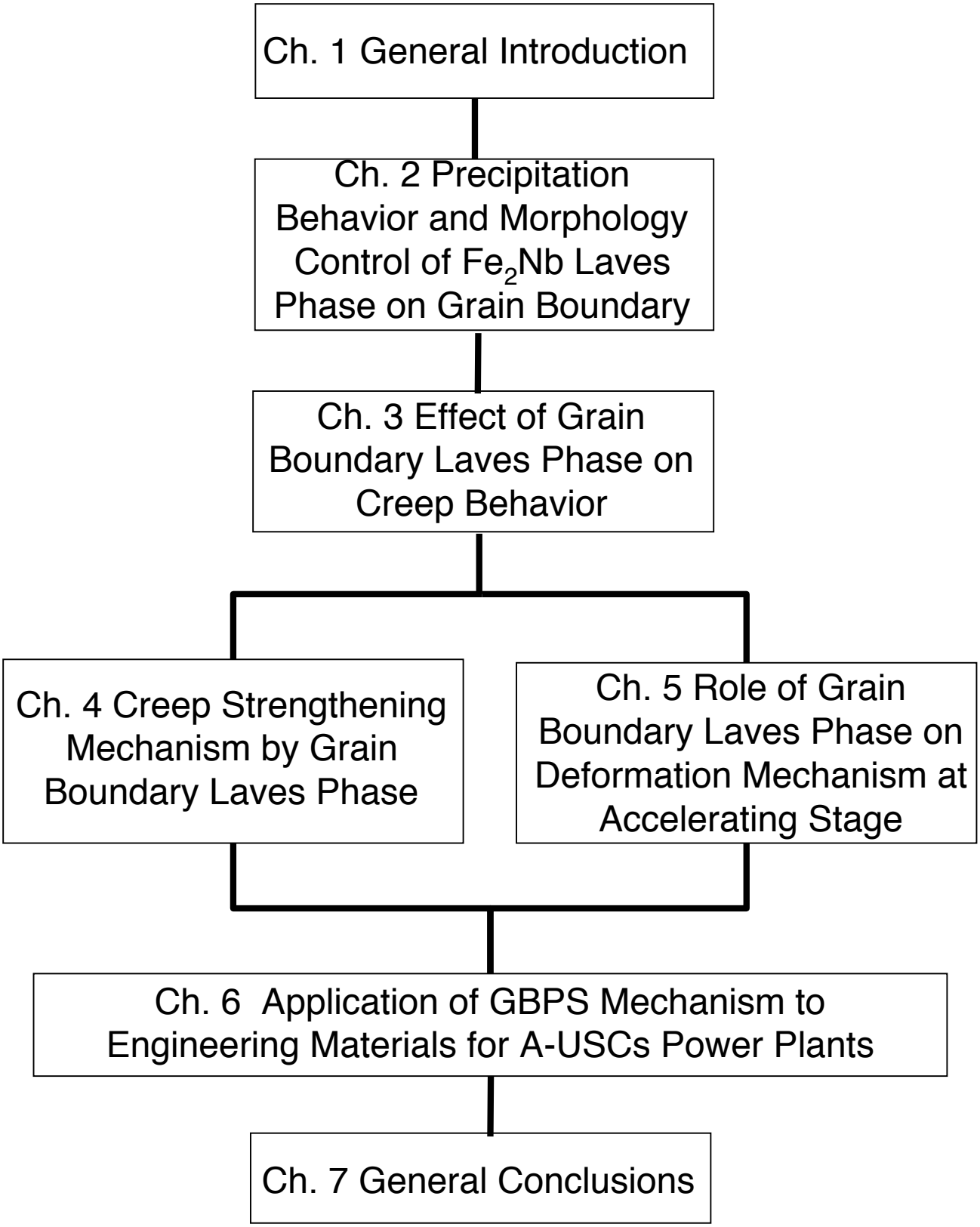

Fig. 1-17 Flow chart of the present thesis.

Chapter 2

Precipitation Behavior and Morphology Control of Fe_2Nb Laves Phase at Grain Boundary

2.1 Introduction

In Chapter 1, it was observed that at the long-term creep test, the creep acceleration stage of the model steel is extended significantly and the microstructure consists of high precipitation of GB Laves. Based on this result it has been proposed that the GB Fe_2Nb Laves phase is responsible for the superior long-term creep rupture strength of the model steel. However, more observations are needed to confirm this result and clearly identify the role of GB Laves on creep strengthening. This can be done by comparing the results with another steels exhibiting the enhanced precipitation of GB Laves phase. Therefore, we need to find a method to control the precipitation of GB Laves phase in the model steel.

The possible way to control the precipitation in steels is through aging treatment or alloying. The effect of aging treatment on precipitation of GB Laves phase in our model steel has been briefly described in Chapter 1. By conducting aging treatment before the creep test, we could examine the behavior of the steels with different amount of precipitates. As for alloying, it has been previously reported that small addition of boron can significantly enhance the precipitation of α_2-W (bcc) phase in γ matrix of Ni-Cr-W superalloys [1]. Based on this result, we intentionally added small amount of boron into our model steel as an attempt to enhance the precipitation of Laves phase at grain boundary. However, in order to utilize this method, it is necessary to understand how the boron can affect kinetics and precipitation behavior of GB Laves in our steel.

The purpose of this chapter is to establish microstructual control, in particular the precipitates of Laves phase at grain boundaries, as a preparatory to elucidate the effect of GB Laves phase on creep strengthening mechanism. For this objective, in this chapter the precipitation behavior and morphology of B-doped steel is carefully examined and compared with the base model steel.

2.2 Experimental Procedures

The experimental procedure of this study is shown in **Fig. 2-1**. The steels used in this study are the model steel with the addition of 0.03 at.% B, which is referred as B-doped steel for short. As comparison, we also used the model steel Fe-20Cr-30Ni-2Nb at.% (base). Detail compositions of each steel are listed in **Table 2-1**. All steels were prepared by using Vacuum Induction Melting (VIM), followed by hot forging at 1473 K into ϕ12 mm rod shape. The steels were then solution treated at 1473 K/2h for B-doped steel and 1523 K/1h for the base to adjust the grain size of 150 μm.

To observe the microstructures, the solution treated steels were aged at 973K and 1073K for up to 3600 h. The aged specimens were polished in sequence by using emery papers with size of #400, #800 and #1200, continued by diamond paste polishing with size of 3 and 1 mm. Final polishing was done by using 0.02 mm alumina powder and 0.05 mm colloidal silica. To reveal the precipitation of Ni_3Nb at grain interior, the specimens were electro-polished in a solution of phosphoric acid with supersaturated chromic anhydride at condition of 20V, 1A, 373 K for up to 1 minute. Three-dimensional morphology of Laves

phase was observed by electro-polished the specimens for longer time to dissolve the γ matrix. Then the heavily electro-polished specimens were tilted 45^o in FE-SEM to observe the precipitates from different angle. Microstructures were examined by using JEOL FE-SEM: JSM-7000F operating at 15 kV with working distance (WD) of 10 mm. Grain boundary misorientation was observed by Electron Back-Scattered Diffraction (EBSD) with step size 5 mm and analyzed by Orientation Imaging Microscopy (OIM) software.

For analyze quantitatively precipitation of Laves phase at grain boundary, the term area fraction (ρ) is used, which is calculated by using the equation 1 with *l* and *L* are the length of GB Laves and total length of GB, respectively. The observation were done on random position along the specimen surface with about 1000 μm of total grain boundary length was examined for each measurements. Assessment of precipitation density within grain interior was done by hardness test measurement within grain interior. Micro Vickers hardness test with 9.8 N load was used to obtain hardness value.

$$\rho(\%) = \frac{\left(l_1 + l_2 + l_3 + l_4 + ...\right)}{L} \quad (1)$$

2.3 Results and Discussion

2.3.1 Precipitation behavior of B-doped steel

Figure 2-2 shows the electro-polished microstructures of B-doped steel after aged at 973K for 20, 240, 1200 and 3600 h, together with those of the base steel [2,3] as comparison. At early stage of aging, the Fe_2Nb Laves phase starts to precipitate at grain boundaries and grain interior and simultaneously fine precipitation of Ni_3Nb-γ" occurs at grain interior (Fig. 2-2 (a,b)). Precipitation of Laves as well as γ" phases increases significantly with further aging. After 240 h of aging, the γ" starts to transform into coarse Ni_3Nb-δ phase within grain interior. At 3600 h, the microstructure of both steels show fine morphology of Laves phase at grain boundaries and coarse acicular morphology of δ within grain interior. From all these microstructures, it is apparent that there is no difference on phase present within B-doped and base steels during all aging time at 973K. However the precipitation of GB Laves in B-doped steel is much higher and finer than that in the base steel. As for GI precipitates, the B-doped steel shows less precipitation density compared to that of the base, except at 3600 h where it appears to be the same in both steels.

Figure 2-3 shows the microstructures of B-doped and base steels after aged at 1073 K. Only Fe_2Nb Laves phase precipitates at grain boundary and grain interior of both steels, without any precipitation of Ni_3Nb. At an early stage of aging, the Laves phase preferentially precipitates at grain boundary of both steels, followed by precipitation at grain interior. With further aging, the precipitation of Laves phase in grain boundary of both steels continues to increase even after 1200 h, whereas at grain interior, it becomes saturated at 240 h. After 240 h of aging, the precipitation density within grain interior of

B-doped steel seems to decrease and becomes much lower than that of the base steel. Similar to the microstructure observations for 973K aged specimens, at 1073K, the phase presents in B-doped steel is the same as that in the base steel. The only difference between these two steels is only the amount of precipitation at grain boundary and grain interior. The B-doped steel has much higher precipitation of Laves phase at grain boundary but less precipitation density within grain interior compared to that of the base steel.

2.3.2 Precipitation kinetics of Laves phase at grain boundary

Figure 2-4 shows change in ρ with aging time in B-doped and base steels at 973 K as well as at 1073 K. At 973K, both steels show sigmoid-shape like curves where the ρ increases rapidly up to 1200 h of aging and becomes slower afterwards. However, the precipitation kinetics in B-doped steel is much higher, which results in much higher ρ compared to that of the base at all aging time. The ρ of B-doped steel after 3600 h of aging can reach up to 54%, while in base is only 42%. Nevertheless, the precipitation of GB Laves phase in both steels keep increasing even after 3600 h of aging. At 1073 K, the curves of both steels also show sigmoid-shape with the highest growth occurs between 1 to 24 h. At this temperature, the ρ becomes much higher compared to that at 973 K and the difference in ρ between B-doped and base steels becomes much larger, with B-doped steel always have higher ρ at all aging time compared to the base. At 1200 h, the ρ in B-doped steel can reach up to 89%, while the base only 52%. At 3600 h, the ρ in B-doped one slightly decreases into 79%, which might be due to the coalescence of Laves phase at grain boundaries. The detail measurement results of ρ for each aging time at 973 K and 1073 K are listed on **Table 2-2**.

Figure 2-5 shows change in grain interior hardness of B-doped and base steels at 973 K as well as at 1073 K, the detail results are listed in **Table 2-3**. The B-doped steel shows similar tendency of hardness change to that of base steel at all temperature, where the hardness is much higher at 973 K than that at 1073 K due to the precipitation of Ni_3Nb. This is in good agreement with the observed microstructure, which show that B-doped steel has the same precipitates to that in the base one. However, at 1073K, the hardness of B-doped steel is lower and the hardness starts to increase at longer time than that of base steel. At 973K, the hardness of B-doped steel is also lower than the base, although the difference is not as big as that at 1073K. These results also support the precipitation density in B-doped steel is lower than that in the base one, which was observed by SEM (**Fig.2-2, 2-3**).

The aforementioned results clearly indicate that the boron is effective to enhance the precipitation kinetics of GB Laves phase. However, there is still remaining question why the boron can increases the grain boundary precipitation. Moreover, it is also interesting point to find out why the addition of boron makes the GB Laves become much finer and more evenly distributed along the grain boundary (**Fig. 2-2**). In attempt to answer these issues, we have tried to re-evaluate the precipitation of GB Laves in terms of the activation energy for nucleation in both steels.

Based on classical nucleation theory [4], the precipitation at grain boundary will result in the elimination of the defect (grain boundary) that release some free energy (ΔG_d) and thereby reducing the activation energy barrier for heterogeneous nucleation according to equation 2:

$$\Delta G = -V(\Delta G_v - \Delta G_s) + A\gamma - \Delta G_d \quad (2)$$

where ΔG_v, ΔG_s, γ are volume free energy, misfit strain energy and interfacial free energy respectively. As for the free energy of grain boundary, ΔG_d is given by:

$$\Delta G_d = A_{gb}\,\gamma_{gb} \quad (3)$$

where A_{gb} is the area of grain boundary eliminated during the precipitation and γ_{gb} is the grain boundary energy. In general, the energy of low angle boundary with lower misorientaion (θ) than 15^o can be expressed as the total energy of the aligned dislocations consisting the boundary [5], following the equation 4.

$$\gamma = \gamma_0(\theta A - \ln\theta) \quad (4)$$

where $\gamma_0 = Gb/\pi(1-v)$ (G: shear modulus, v: poisson ratio, b: Burgers vector), $A = 1+\ln(b/2\pi r_0)$ and r_0 is the radius of the dislocation core. As the θ increases, the density of dislocations in the boundary becomes higher, which result in higher boundary energy.

Based on this theory, we have assumed that the grain boundary misorientation might have an influence on precipitation kinetics of GB Laves phase and such observation possibly can give a suggestion to resolve a question how the boron change the precipitation kinetics at grain boundary. Therefore, we have tried to observe the precipitation kinetics of GB Laves at 3 types of grain boundaries in both B-doped and base steels, i.e. low angle boundary ($\theta < 15^o$), high angle boundary ($\theta \geq 15^o$) and twin boundary ($\theta = 60^o$).

Figure 2-6 shows the microstructures at low angle boundary (LAB), high angle boundary (HAB) and twin boundary (TB) of B-doped and base steels after aged at 1073K / 240 h. In base steel, the precipitation of GB Laves phase at LAB is lower than the HAB and TB, with the average ρ of 34%, 56% and 100% respectively. On the other hand, the precipitation of GB Laves phase in LAB and HAB of B-doped steel is the same with average ρ of about 71%. The precipitation at TB in B-doped steel shows similar result where GB Laves covers the entire grain boundary.

Figure 2-7 shows the change in the area fraction (ρ) of GB Laves as a function of GB misorientation angle (θ) in B-doped and base steels aged at 1073 K / 240 h. In the base steel, ρ increases from 15 to 51% with increasing θ up to about 18^o, which is close to a maximum misorientaion of low angle boundary. Then ρ becomes constant independent of θ of about 51%. On the other hand, the ρ in B-doped is constant independent of θ, with the

average of about 72%.

From these results, it can be observed that the precipitation kinetics of GB Laves phase in LAB is more sluggish than that in HAB. It is in good agreement with the nucleation theory, where the low θ in LAB results in low grain boundary energy and thus higher activation energy for nucleation compared to that of HAB. Surprisingly, the small addition of boron can enhance the precipitation kinetics of GB Laves phase on even LAB. This might be associated with the increase in free energy of grain boundary, ΔG_d, which decreases the activation energy for nucleation by B segregation at GB. It can explain why the B-doped steel has higher kinetics and also finer precipitation of GB Laves compared to the base. While the detail mechanism is beyond the scope of this thesis, these results give us an indication that the boron might segregate at grain boundary and cause the ΔG_d as has been suggested by other reports [6,7].

2.3.3 Morphology of Laves phase at grain boundary

Figure 2-8 shows the morphology of GB Laves phase in the base steel aged at 1073K for 240 h. On the left side of the pictures, from top to bottom, are the two-dimensional observations of GB Laves on LAB, HAB and TB respectively. The right side of the pictures shows the three-dimensional view of the left side pictures. From the two-dimensional view, there is no difference in morphology between LAB and HAB. However, three-dimensional observations revealed that at the LAB, the GB Laves has rod-like shape, while at HAB it has granular shape. As to the twin boundary, both observations show thin planar shape of GB Laves.

Figure 2-9 shows the morphology of GB Laves phase in the B-doped steel aged at 1073K for 240h. The left side of the pictures is the two-dimensional view of the precipitates, while the right one shows the three-dimensional observation of the left side pictures. From the two-dimensional observations, the Laves phase on LAB exhibits rod-like shape while that on HAB has granular shape morphology. It was observed from the three-dimensional views that the GB Laves at the LAB might has preferential growth direction, where the precipitates appear to be aligned along its axis toward certain direction. The precipitates at the right side of the LAB are very dense and almost cover the entire grain boundary area. On the other hand, the precipitates at HAB do not show any preferential growth direction. The precipitates are connected to each other to form a wall with few gaps left. On TB, planar-shape Laves phase precipitates and fully cover the entire grain boundary area.

From these results it can be clearly seen that the GB Laves at LAB has different morphology compared to that at HAB and TB. The addition of boron does not change these morphologies, however since it enhances the precipitation kinetics, the precipitates connects each other and form a solid wall. Although the difference in ρ between B-doped and base steel is only 21% (51% and 72%, respectively), it shows big difference in terms of the grain boundary area that covered by GB Laves.

2.4 Summary

Precipitation behavior and morphology of Fe_2Nb Laves at grain boundary have been observed. The followings are the conclusions obtained in this chapter:

1) Boron can enhance the precipitation of Fe_2Nb Laves phase at grain boundary.
2) B-doped steel has higher precipitation of Laves phase at grain boundaries but lower precipitation density within grain interior compared to that of the base steel.
3) In base steel, the precipitation kinetics of Laves phase at low angle boundary is lower than that at high angle grain boundary, whereas in B-doped steel the precipitation kinetics is the same on all grain boundaries.
4) Boron does not change the morphology of grain boundary Laves phase.

References

[1] T. Matsuo, M. Kikuchi and M. Takeyama: Strengthening Mechanisms of Ni-Cr-W Based Superalloys for Very High Temperature Gas Cooled Reactors, Proc. 1st Inter. Conf. Heat-Resistant Materials, (1991), 601.

[2] N. Hashizume: Master Thesis, Tokyo Institute of Technology, (2008).

[3] K. Kurata: Master Thesis, Tokyo Institute of Technology, (2009).

[4] D. A. Porter, K. E. Easterling, and M. Sherif, *Phase Transformations in Metals and Alloys*, 3rd ed. (CRC/Taylor & Francis [distributor], Boca Raton, FL/London, 2009).

[5] F. J. Humphreys and M. Hatherly, RECRYSTALLIZATION and Related Annealing Phenomena, 2nd ed, (Pergamon), (2002) p. 60.

[6] D. A. Mortimer: J. Phys. Colloques, 36 (Nov. 1975), pp. c4-137 – c4-140.

[7] S. H. Song, A. M. Guo, D. D. Shen, Z. X. Yuan, J. Liu, T. D. Xu: Materials Science and Engineering A, 360(2003), pp. 96-100.

Table 2-1 Analyzed composition of studied steels.

Steel	Compositions / at.%				
	Fe	Cr	Ni	Nb	B
Base	Bal.	19.7	29.9	2.03	-
B-doped	Bal.	19.8	29.9	2.01	0.032

Table 2-2 Area fraction of B-doped and base steels after aged at 973K and 1073K.

Steel	Aging condition		Area fraction at G.B. /%		
	Temp. /K	Time /h	ave.	min.	max.
0B	1073	10	31.8	25.3	36.6
		24	32.0	30.0	36.0
		240	42.9	32.8	51.9
		1200	52.3	47.1	62.0
		3600	53.7	49.7	56.5
	973	20	20.7	14.3	26.6
		240	31.0	24.2	38.3
		1200	39.3	32.5	48.0
		3600	41.7	34.0	46.9
3B	1073	10	51.9	39.7	57.3
		24	69.9	64.2	82.4
		240	80.1	73.8	90.8
		1200	88.8	82.6	94.4
		3600	79.4	65.7	90.5
	973	20	29.5	28.1	30.9
		240	33.5	29.0	37.9
		1200	60.5	56.2	70.1
		3600	63.5	60.1	70.9

Table 2-3 Hardness of B-doped and base steels in as solution treated condition and aged at 1073K and 973K.

Steel	Aging condition		Hardness /GPa		
	Temp. /K	time /h	ave.	min.	max.
Base	as solution treated		1.35	1.33	1.38
	1073	0.03	1.39	1.35	1.43
		0.08	1.41	1.36	1.45
		0.25	1.44	1.39	1.47
		1	1.52	1.48	1.56
		3	1.60	1.54	1.68
		10	1.65	1.62	1.73
		24	1.74	1.66	1.85
		240	1.78	1.76	1.79
		1200	1.80	1.74	1.82
		3600	1.81	1.76	1.85
	973	72	1.69	1.61	1.74
		240	1.87	1.65	2.13
		1200	2.23	2.17	2.31
		3600	2.21	2.19	2.24
B-doped	as solution treated		1.30	1.26	1.31
	1073	3	1.48	1.45	1.53
		10	1.53	1.52	1.57
		24	1.51	1.42	1.57
		240	1.72	1.70	1.74
		1200	1.61	1.58	1.66
		3600	1.71	1.67	1.76
	973	20	1.49	1.46	1.54
		240	1.84	1.80	1.91
		1200	2.09	2.05	2.11
		3600	2.19	2.13	2.25
					(Load: 9.8N)

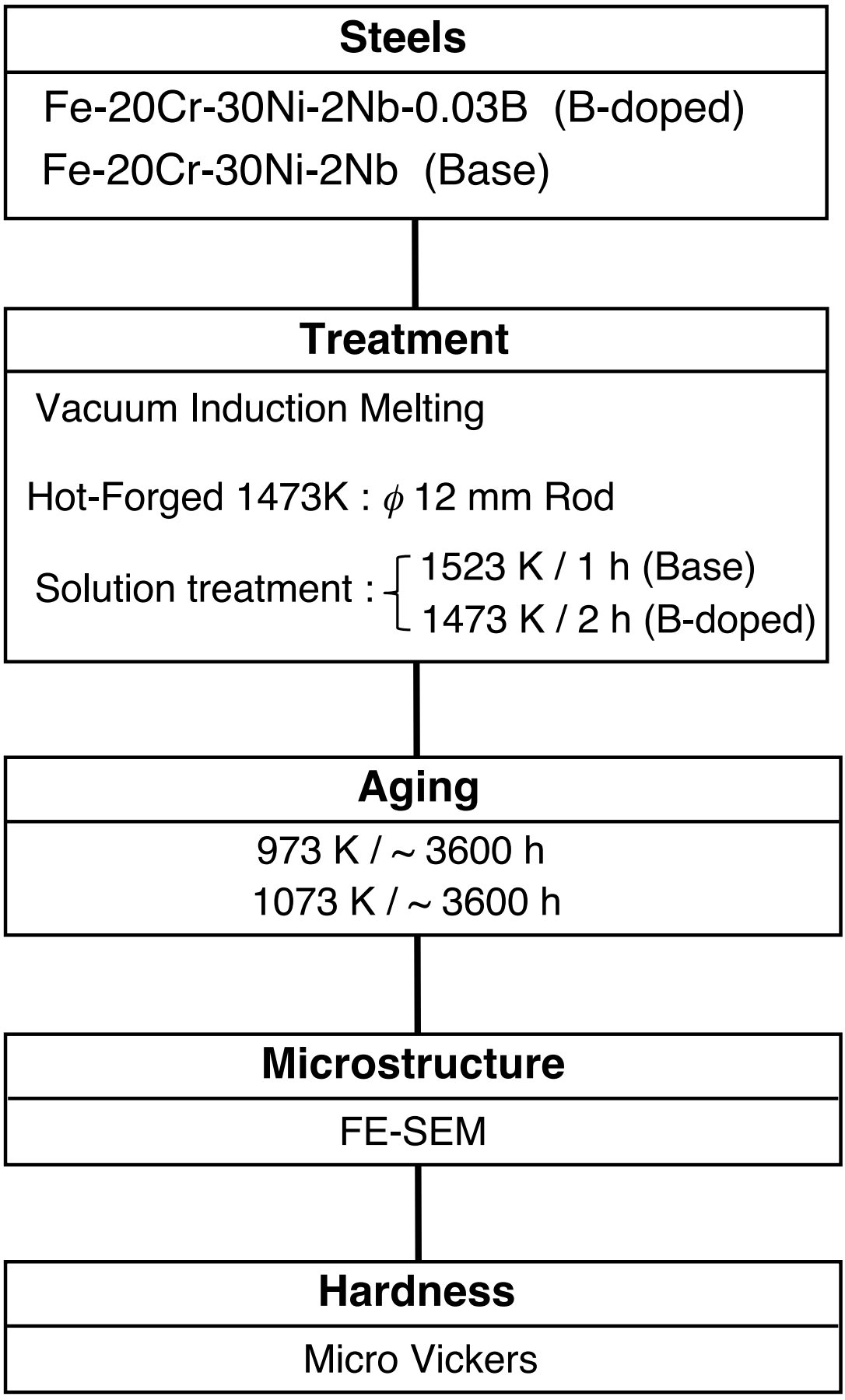

Fig. 2-1 Flow chart of the experimental procedure in the chapter 2.

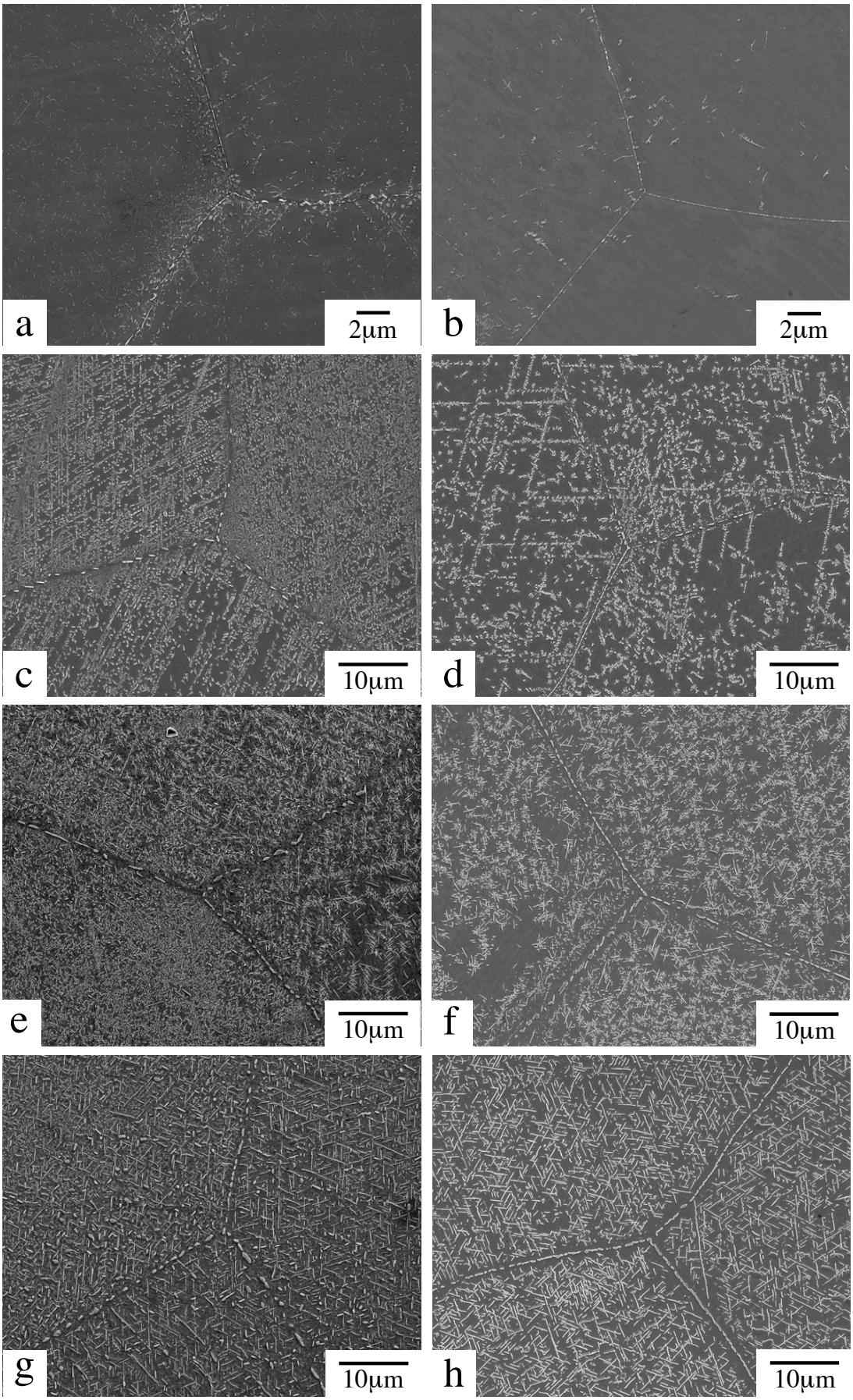

Fig. 2-2 BEIs of base (a, c, e, g) and B-dope (b, d, f, h) steels aged at 973 K : (a, b) 20 h, (c, d) 240 h, (e, f) 1200 h, (g, h) 3600 h as electropolished

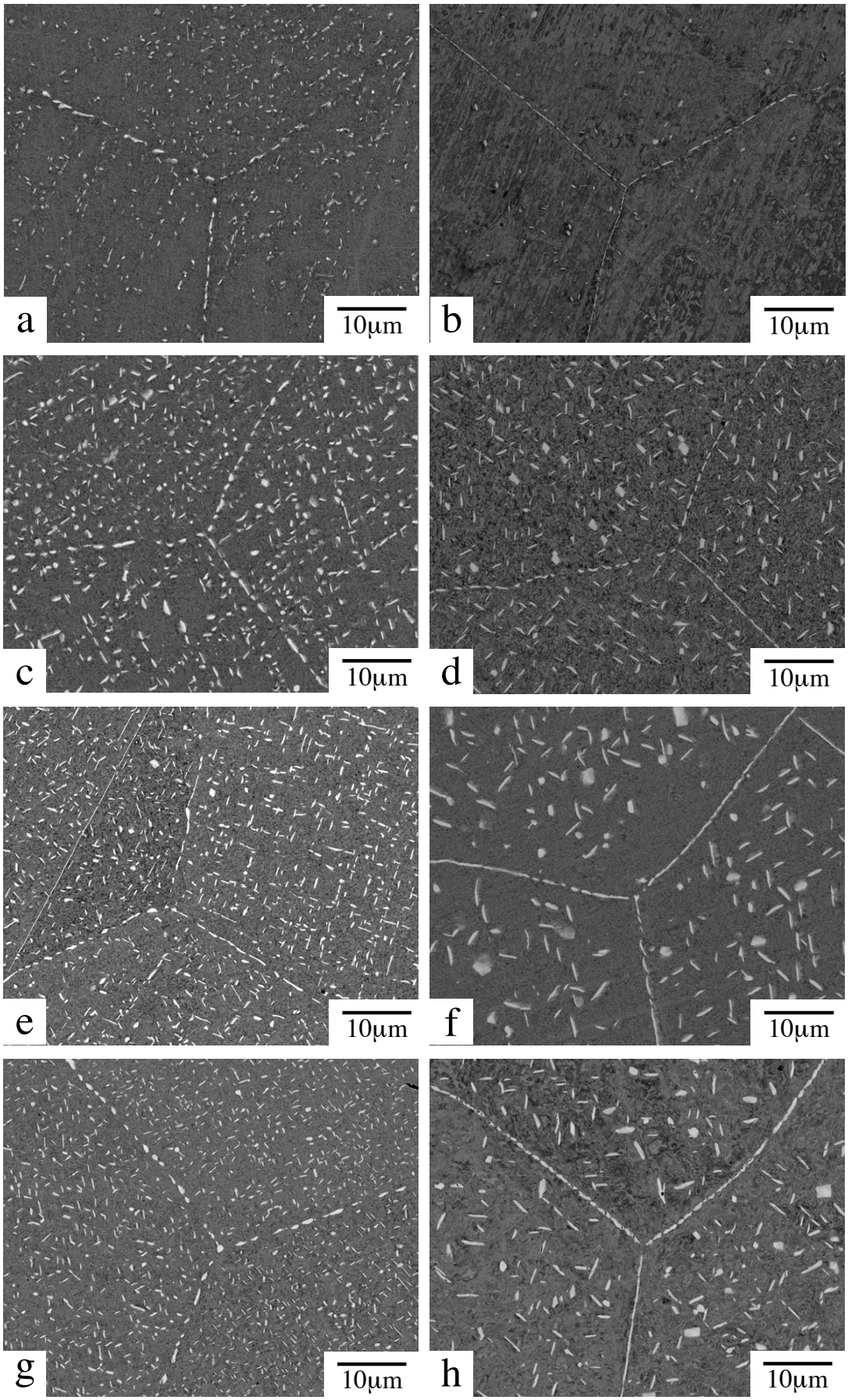

Fig. 2-3 BEIs of base (a, c, e, g) and B-dope (b, d, f, h) aged at 1073 K as mechanical polished : (a, b) 24 h, (c, d) 240 h, (e, f) 1200 h, (g, h) 3600 h.

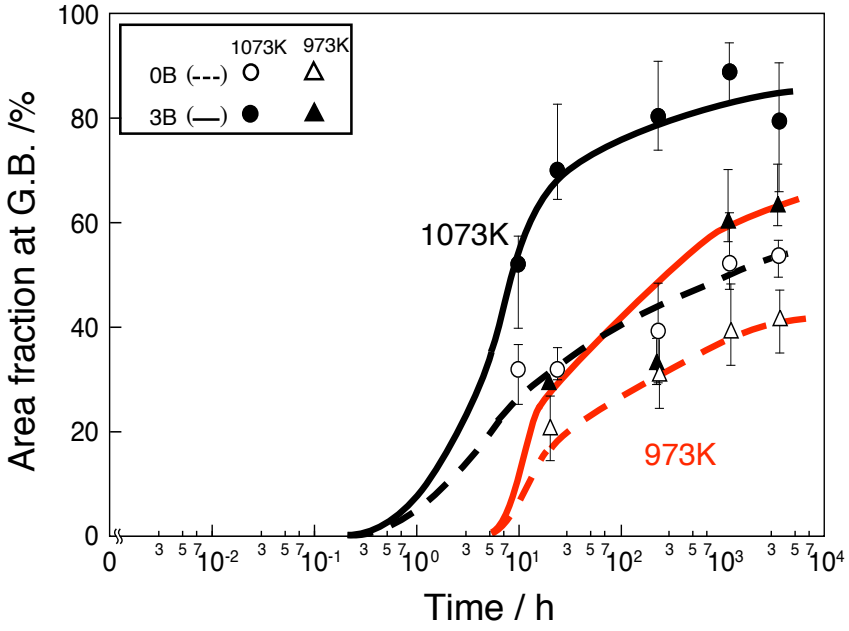

Fig. 2-4 Change in ρ of base and B-doped steels with aging at 973K and 1073 K.

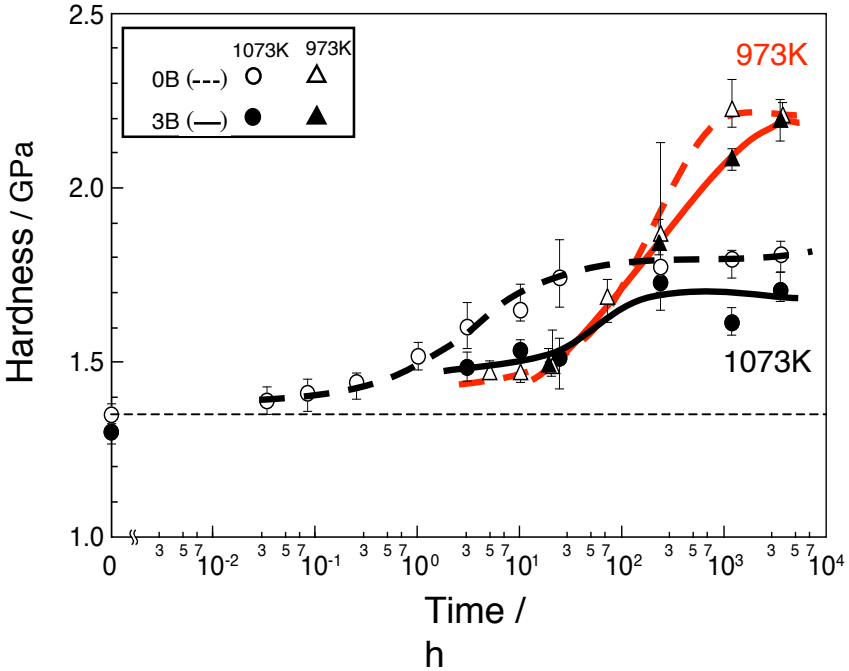

Fig. 2-5 Change in hardness of base and B-doped steels with aging at 973K and 1073 K.

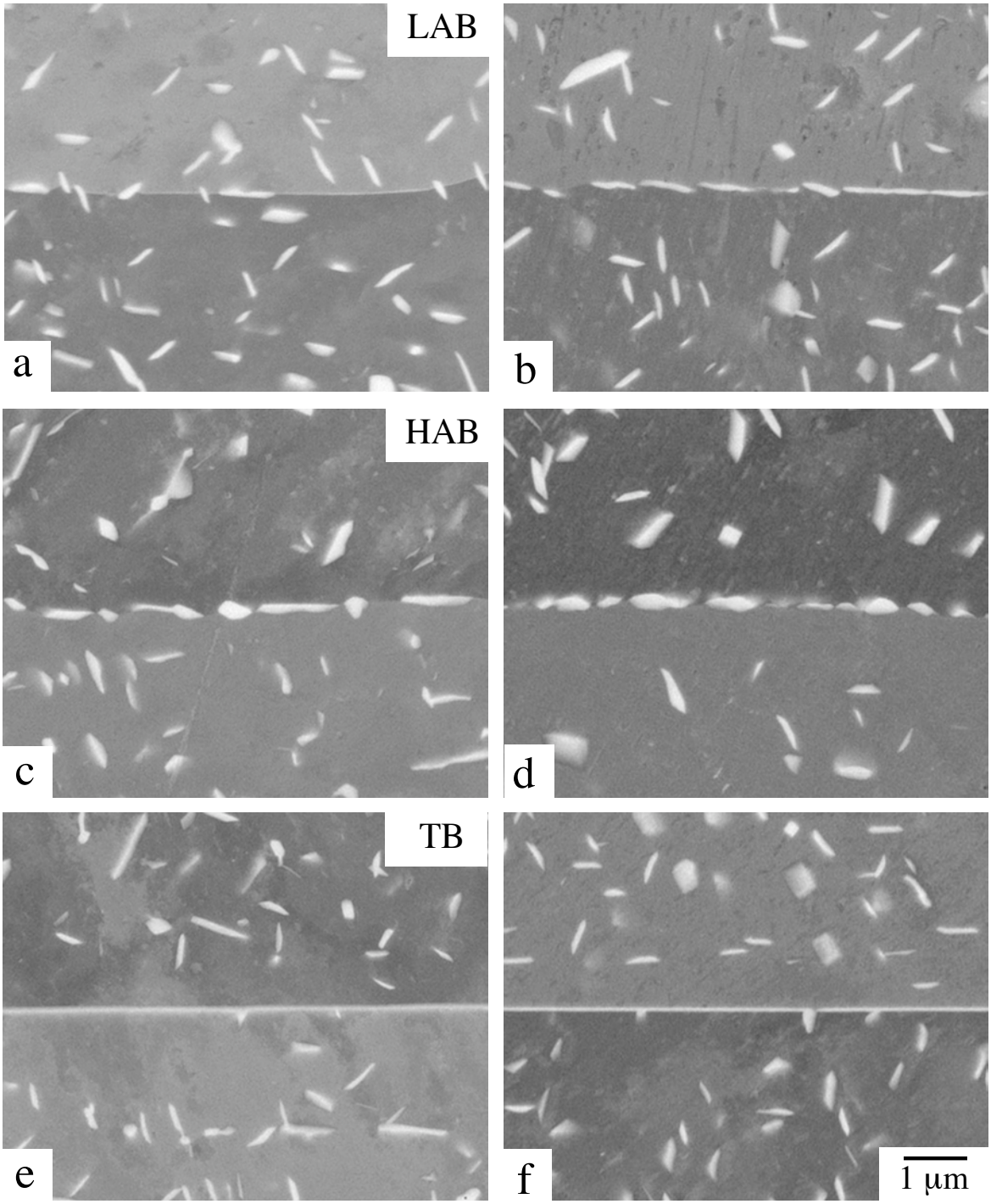

Fig. 2-6 BEIs of GB Laves phase on Low angle boundary (a, b), High angle boundary (c,d), and Twin boundary (e, f) in: base (a, c, f) and B-doped (b, d, f) steels aged at 1073 K for 240 h

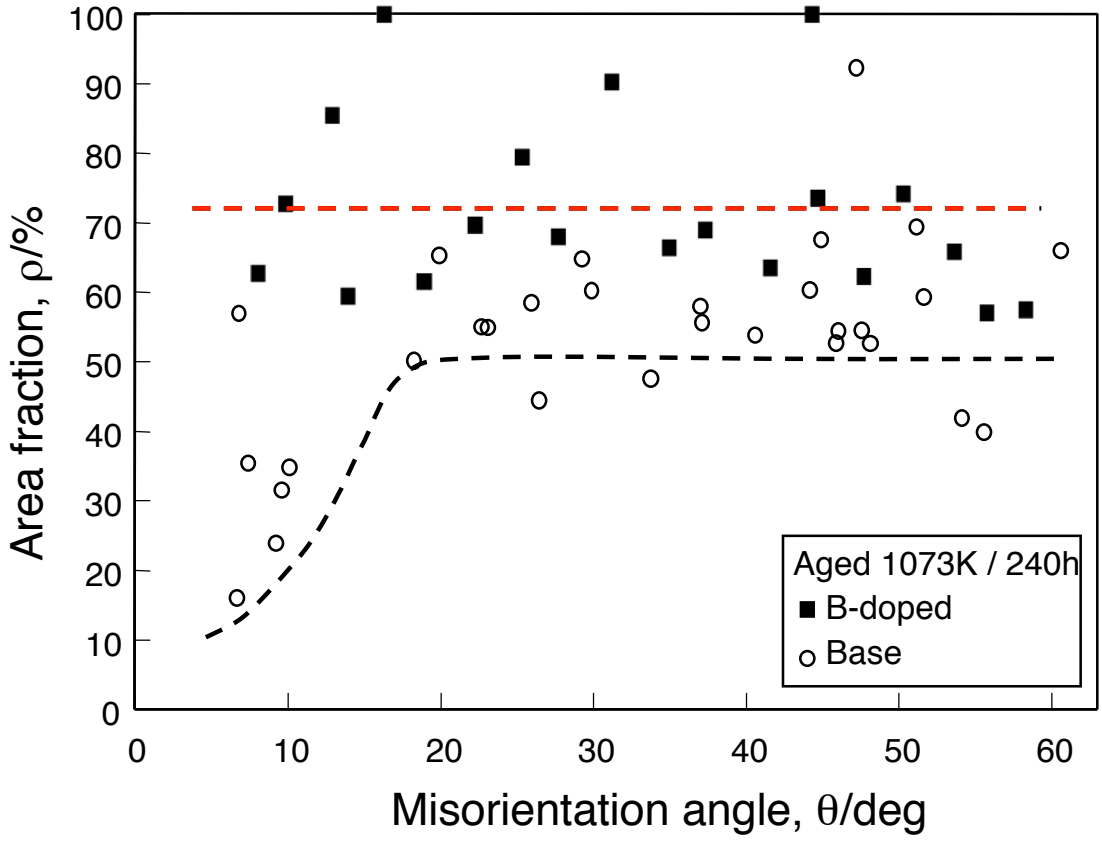

Fig. 2-7 Change in the area fraction (ρ) of GB Laves phase as a function of GB misorientation angle (θ) in the B-doped and base steels aged at 1073K / 240 h.

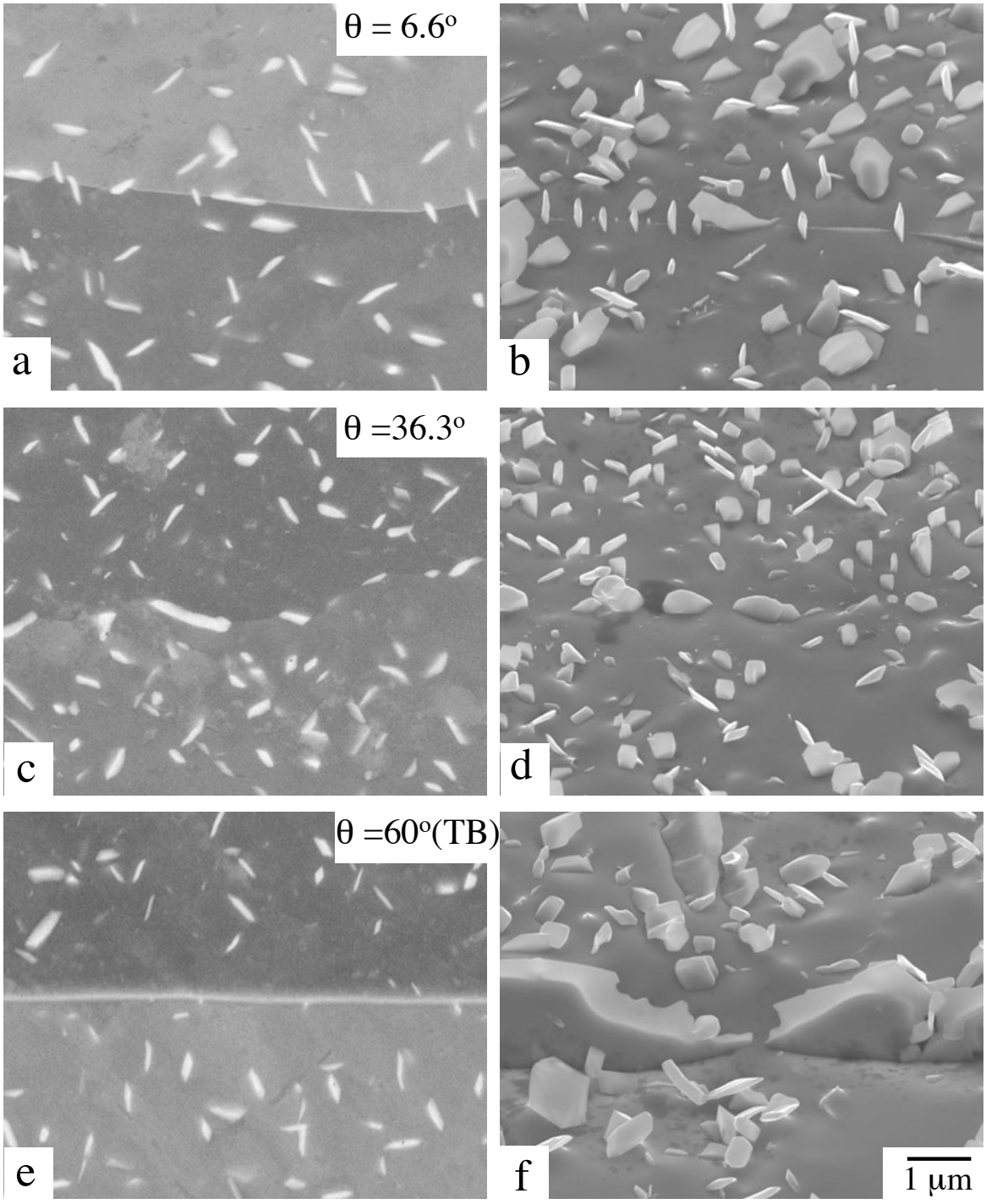

Fig. 2-8 BEIs of GB Laves phase on low LAB (a, b), HAB (c, d) and TB (e, f) in base steels aged at 1073 K for 240 h: (a, c, e) two dimensional observation as mechanical polished, (b, d, f) three dimensional observation as electro-polished. .

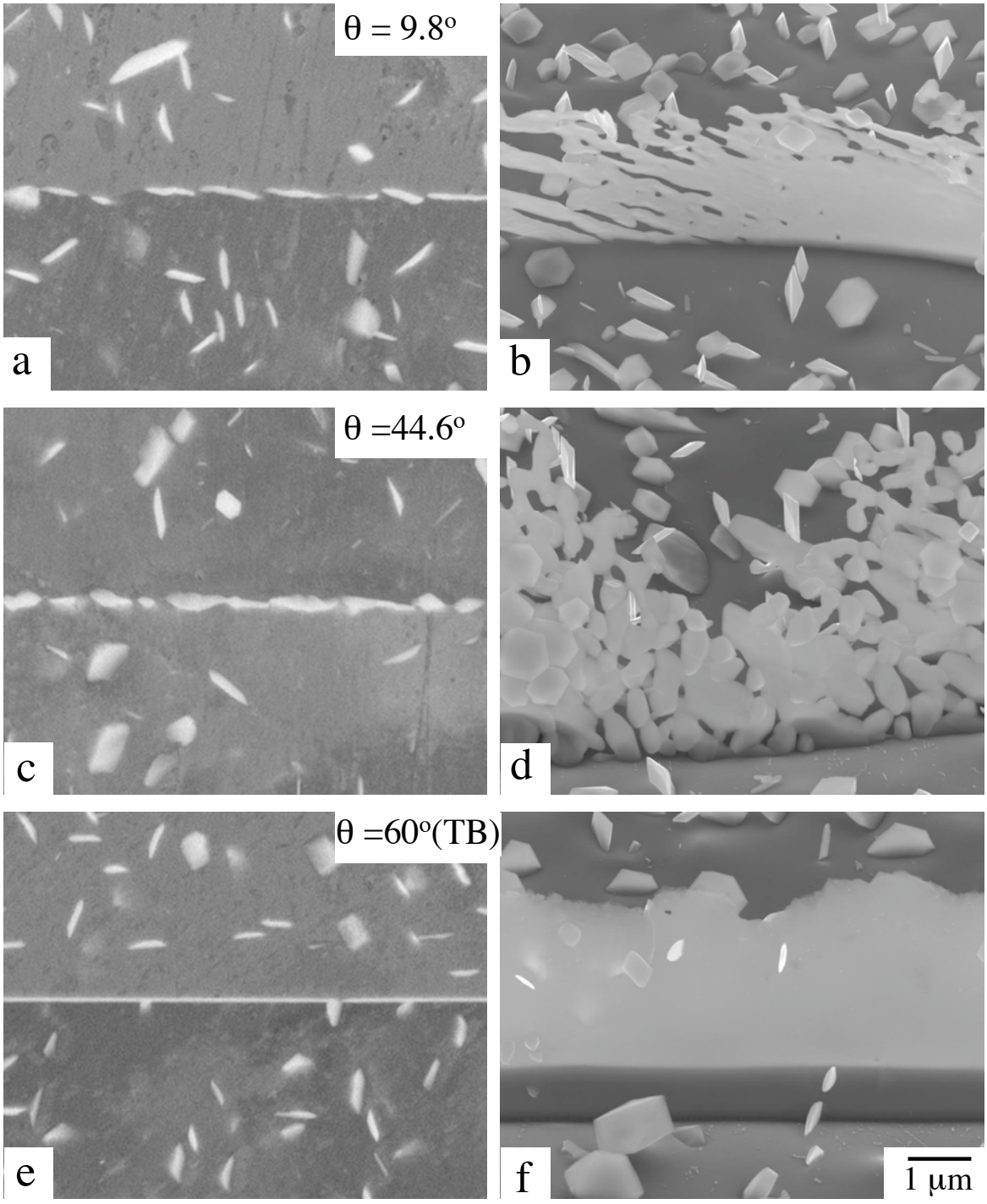

Fig. 2-9 BEIs of GB Laves phase on low LAB (a, b), HAB (c, d) and TB (e, f) in B-doped steels aged at 1073 K for 240 h: (a, c, e) two dimensional observation as mechanical polished, (b, d, f) three dimensional observation as electro-polished. .

Chapter 3

Effect of Grain Boundary Laves Phase on Creep Behavior

3.1 Introduction

In chapter 2, we have successfully found methods to control precipitation of GB Laves in our model steel by addition of trace boron and aging treatments. The addition of boron clearly enhances the precipitation of GB Laves phase without affecting the GCP phase of Ni_3Nb within grains. In addition, the shape of Laves phase at grain boundary is also unaffected by the boron. However, the B-doped steel has lower precipitation density within grain interior compared to the base. After these findings, it became our interest to examine the difference in the creep behavior of two steels with different microstructures.

It is generally believed that the steel with higher precipitation density within grain interior will exhibit higher creep rupture strength. This is the reason why in most of the steel design, people is trying to control fine precipitation morphology in grain interior, without paying much attention to the grain boundary. On the contrary, we have proposed [1-3] that grain boundary strengthening plays a significant role in increasing long-term creep rupture strength of the steels, as indicated by the creep test results of our model steel of Fe-20Cr-30Ni-2Nb, as shown in Chapter 1. However, the data obtained so far is not enough to support this concept for strengthening by Laves phase on GB. Therefore, the investigation of creep behavior of B-doped steel is needed to elucidate the effect of GB Laves phase and give us well understanding how effective is the grain boundary strengthening for the long-term creep rupture strength.

In this chapter, the creep behavior of B-doped steel and base steel (solution treated condition) has been examined at 973K and 1073K under constant stresses.

3.2 Experimental Procedures

The flowchart of the experimental procedures used in this study is shown in **Fig. 3-1**. The steels used in this study are B-doped and base steels, which have the same compositions as described in Chapter 2. All steels were prepared by the same processes described in chapter 2, followed by solution treatment to obtain the grain size of 150 μm.

For the creep test, the solution-treated rod was machined into full-size dimension according to JIS G0567 standard with 28 mm in gauge length and 6 mm in diameter, as shown in **Fig. 3-2**. Tensile creep tests were conducted at 973 K at constant stresses of 120, 140 and 200 MPa. To prevent the precipitation of Ni_3Nb, some of the creep tests were done at 1073K at constant stresses of 50, 60 and 70 MPa. Creep strain was measured by using extensometer equipped with linear variable differential transducers (LVDT). All of the creep tests were started within 4 hours after heating in order to avoid the precipitation of both intermetallic phases before the initial loading.

Microstructures after the creep tests were examined by using FE-SEM: JEOL JSM-7000F operating at 15 kV. The area fraction of Laves phase on GB (ρ) is used to interpret the precipitation of GB Laves phase, which was calculated by the same method described in Chapter 2.

3.3 Results and Discussion

3.3.1 Creep Behavior of Solution Treated Steels at 973K

In general, the response of materials to creep loading can be divided into 2 types depending on the applied stress. Creep under above and below yield stress are high stress and low stress creep, respectively. The low stress creep might be related to lower mobile dislocation density than that under high stress creep, and thus shows lower creep rate and different creep behavior. Therefore, in order to clearly observe and compare the creep behavior between B-doped and base steels, it is necessary to ensure that these two steels tested under the same creep stress level. **Figure 3-3** shows the instantaneous strain as a function of the applied stress in both B-doped and base steels at 973 K. Both B-doped and base steels exhibit a linear stress-strain relationship up to about 150 MPa. Beyond this point, the instantaneous strain significantly increases with increasing the applied stress. Based on this result, the 150 MPa is defined as the critical stress to distinguish the low stress and high stress creep for both B-doped and base steels. It also implies that the comparison of the creep behavior of both B-doped and base steel can be done at the designated stress levels (120, 140 and 200 MPa) since both of the steels are in the same creep stress level.

Figure 3-4 show stress-rupture time curves at 973K of the solution treated B-doped and base steels together with the reported Inconel 740 and conventional 347 austenitic heat resistant steels [4,5]. The B-doped steel shows excellent creep rupture strength, much stronger than the 347 austenitic heat resistant steels and the base model steel. The extrapolated 10^5 h creep rupture strength at 973 K is about 90 MPa, which almost meets the requirements for A-USC power plant. Note that these lines are extrapolated from the lower stress creep region (140, 120 MPa) defined in **Fig. 3-3**. The followings are the details of creep behavior of the steels at each stress condition:

(A) 200 MPa

Figure 3-5 ~ 3-8 show the creep test results of solution treated B-doped steel at 973K / 200 MPa, in addition to those of the base steel under the same test condition. Note that this stress level is in high stress creep region as have been mentioned previously. **Figure 3-5** shows the creep curve of both B-doped and base steels. At the initial loading, both B-doped and base steels exhibit almost the same instantaneous strain at around 4%. Following this stage, the creep strain of B-doped steel slowly increases to 5% at 1000 h and then it rises exponentially until rupture at 9.7% in strain and time of 1373 h. This rupture strain is more than 2 times larger than that of base steel, which ruptured at 4.5%. The higher creep strain of B-doped steel is also accompanied by significant increase of the rupture time, which is more than 4 times longer than the base steel (t_r = 340 h). **Figure 3-6** shows the creep rate – time curves of B-doped and base steels at 973 K / 200 MPa plotted in semi logarithmic scale. The B-doped steel reaches minimum creep rate of 1.5 x 10^{-6} h^{-1}, which is slightly lower than that of the base ($\dot{\varepsilon}_m$ = 3 x 10^{-6} h^{-1}). At the acceleration stage, while the creep rate of base steel rapidly increases and rupture at 340 h, the creep rate of

B-doped steel keeps increasing at a constant rate until fracture at 1373 h, resulting in the longer acceleration stage compared to that of the base. The creep behavior during the transient stage can be clearly observed on the logarithmic scale of creep rate – time curves, as shown in **Fig. 3-7**. At early transient stage, the creep rate of B-doped steel decreases at lower rate than that of the base but it is followed by sudden decrease to the minimum creep rate after 7 h. The B-doped steel reaches minimum creep rate after 20 h, which is much faster than the base steel (t_m = 70 h). After reaching the minimum, the creep rate of B-doped steel slightly increases and become constant at 3 x 10^{-6} h^{-1} for nearly 400 h before accelerating. It is interesting that the base steel does not show any steady stage creep after the minimum. **Fig. 3-8** shows the creep rate – strain curves of B-doped and bases steels at 973 K / 200 MPa. The B-doped steel reaches minimum creep rate at strain of 0.3%, which is smaller than that of the base steel (ε_m = 0.7%). After the minimum, the creep rate of B-doped steel increases at a constant rate for wide range of strain, resulting in much longer acceleration stage compared to that of the base steel.

(B) 140 MPa

Figures 3-9 ~ 3-10 shows the creep test results of solution-treated B-doped steel at 973K / 140 MPa, in addition to the creep data results of base steel at the same test condition. The test stress condition is in the lower stress creep behavior region. **Figure 3-9** shows the creep curves of B-doped and base steels. At the initial loading, the B-doped steel exhibits instantaneous strain of 0.1%, which is slightly lower than that of the base (0.4%). After the initial stage, the creep strain of B-doped steel gradually increases at almost the same rate as that of the base one. However, while the creep strain of base steel rapidly increases to rupture at 2.6%, the creep strain of B-doped steel continues to extend at lower rate up to 2%. Then, it increases exponentially up to ruptured at 11.5%, which is 5 times longer than the rupture strain of the base steel. **Figure 3-10** shows the semi logarithmic plot of creep rate – time curves of B-doped and base steels. The creep rate of B-doped steel reaches minimum at 1 x 10^{-6} h^{-1}, which is almost similar to that of the base steel. After the minimum, while the creep rate of base steel continues to increase until rupture at 1600 h, the creep rate of B-doped steel decreases again shorts after the acceleration and then reaches the second minimum at 4000 h. Then, it keeps a constant rate of 3 x 10^{-5} h^{-1} for about 5000 h, before ruptured at 9107 h. **Figure 3-11** shows the creep rate – time curves of B-doped and base steels plotted in logarithmic scale. At the transient stage, the creep rate of B-doped steel decreases at constant rate until reaches the minimum at 300 h, which is similar to that of the base steel. From this curve it can also be observed that the time to rupture of B-doped steel is almost 1 order magnitude longer than that of the base steel. **Figure 3-12** shows the creep-rate – strain curves of B-doped and base steels. The B-doped steel reaches the first minimum at 0.005% strain, which is more than one order of magnitude smaller than that of the base (ε_m = 0.1%). After the minimum, the creep rate gradually increases with strain up to 7 x 10^{-6} h^{-1} at 0.7% creep strain. Then, it decreases again with increasing creep strain reaching the second minimum at 3 x 10^{-6} h^{-1} at strain of 2%, followed by gradual increases to fracture.

(C) 120 MPa

Figures 3-13 ~ 3-16 show the creep test results of solution treated B-doped, together with those of the base steel, at 973K / 120 MPa. The creep curves are shown in **Fig. 3-13**. At the initial loading the B-doped steel exhibits instantaneous strain of 0.1%, which is slightly lower than that of the base steel (0.2%). The creep strain of B-doped steel increases with time with similar rate to that of the base steel up to 2000h. With increasing time, while the strain of base steel significantly increases up to rupture, the strain of B-doped steel continues to extend at slower rate up to 1% strain. Beyond this point, the strain of B-doped steel is further extended at increasing rate until rupture at 9.5% of strain, which is almost 3 times longer than the rupture strain of the base steel (3.5%). **Figure 3-14** shows the semi logarithmic plot of the creep rate – time curves of the steels. The B-doped steel reaches the minimum creep rate at 9 x 10^{-7} h^{-1}, which is slightly lower than that of the base steel (1.3 x 10^{-6} h^{-1}. After the minimum, the creep rate of B-dope steel gradually increases up to 2000 h by the same rate with that of the base steel. However, after 2000 h, while the creep rate of the base steel becomes constant, the creep rate of B-doped steel decreases again to reach the second minimum at around 6000 h. Beyond this point, the creep rate then slowly increases until rupture at 16721 h, which is almost 3 times longer than that of the bases steel. **Figure 3-15** shows the logarithmic plot of the creep rate – time curves of the steels. In the transient stage, the creep rate of B-doped steel is slightly higher than the base but it gradually decreases and reaches the minimum at the same time, i.e. at 300 h. The creep-rate – strain curves of the steels are shown in **Fig. 3-16**. Both B-doped and base steels reach the first minimum at 0.1% strain. The second minimum of B-doped steel occurs at 1% strain, which is almost the same to that obtained at 140 MPa creep test.

3.3.2 Crept Microstructures at 973 K

Figure 3-17 shows the comparison of microstructures between B-doped and base steels after creep tested at temperature of 973 K and stresses of 200, 140 and 120 MPa. At 200 MPa creep test, the Ni_3Nb-δ and γ" precipitates was observed at grain interior of B-doped steel, while only γ" is present in base steel. At grain boundaries, both Laves phase was observed on both steel, however the area fraction in B-doped steel is much higher than that in the base steel (**Fig. 3-17 (a, b**)). At 140 MPa, the microstructure at the grain interior of B-doped steel fully consists of coarse Ni_3Nb-δ precipitates, while there is still γ" in grain interior of the base steel. Nevertheless, the area fraction of GB Laves phase in B-doped steel is much higher than that in the base steel. At 120 MPa, both steels show precipitation of Laves phase at grain boundaries and coarsened δ phase within grain interior. In this stress condition also, the B-doped steel has much higher precipitation of GB Laves compared to that of the base steel. In addition, the GB Laves in B-doped steel is much finer than that in the base steel. These results confirm our proposed concept that the grain boundary Laves phase is responsible for the superior creep rupture strength of the Fe-20Cr-30Ni-2Nb austenitic heat resistant steel.

3.3.3 Creep Behavior of Solution Treated Steels at 1073K

The creep test at 973 K show further evidences for the creep strengthening effect by GB Laves phase. However, the crept microstructures also contain the precipitation of GCP Ni_3Nb-γ" phase, which presumably obscures the effect of GB Laves phase. Thus, we have tried to examine the creep behavior at 1073 K, where only Laves phase can precipitate during creep, based on the TTP diagram of the steel (**Fig. 1-10**).

Figure 3-18 shows the instantaneous strain as a function of the applied stress in both B-doped and base steels at 1073 K. Both steels exhibit a linear stress-strain curve below 70 MPa in stress, which indicates the elastic strain of the specimens by loading. It obviously shows that the lower stress than 70 MPa can be classified into low stress level for creep at 1073 K.

Figure 3-19 ~ 3-22 show the creep test results of solution treated B-doped and base steels, tested at 1073 K / 70 MPa. **Figure 3-19** shows the creep curves of the steels. At initial loading, the instantaneous strain of B-doped steel is 0.05%, almost the same to that of the base steel (0.06%). After this stage, the strain of both steel increases linearly with time, but the B-doped steel shows much slower rate than the base. After reaching 20% of strain, the strain of B-doped steel increases significantly and ruptured at 31%, while the base steel starts to accelerate at 40% and ruptured at 56%. **Figure 3-20** shows the semi-logarithmic plot of creep-rate – time curves. Both steels show long steady state creep soon after the transient stage. At the beginning of the steady state stage, the creep rate of B-doped steel is 8×10^{-4} h^{-1}, which is lower than that of the base (1×10^{-3} h^{-1}). However, while the creep rate of B-doped remains unchanged with time, the creep rate of base steel gradually increases to 2×10^{-3} h^{-1} at 40 h and keep a constant until reaches the acceleration stage at 200 h. The B-doped steel exhibits the acceleration stage at longer time than the base (280 h), but it lasts only for very short time. Nevertheless, the time to rupture of B-doped steel is longer than that of the base, i.e. 293 h and 248 h, respectively. **Figure 3-21** shows the logarithmic scale of creep-rate – time curves. At the initial stage, the creep rate data B-doped steel slowly decreases until reaches the minimum at 3×10^{-4} h^{-1} and then it increases again before entering the steady state creep stage. The base steel also shows the same tendency but with higher creep rate than B-doped steel, having the minimum at 7×10^{-4} h^{-1}. The reason why both steels show the minimum before the steady state stage has still remained unclear, however it might be related to the solid solution strengthening of Nb within the matrix, which effect diminishes with time as it is used for the precipitation. It can also be observed from the figure that the base steel has two steady state creep stage at this test condition. **Figure 3-22** shows the creep-rate – strain curve of the steels. Both B-doped and base steels reach minimum creep rate, in the transient stage, and also the steady state stage at the same strain, 0.1 and 1.0% respectively. At strain of 3%, while the creep rate of B-doped steel keeps constant, the creep rate of the base steel gradually increases until reaches the second steady state stage at 7% of strain.

These test results at 1073 K show that even if the microstructures consist of only

Laves phase, the same tendencies will be observed, that is the steel with higher precipitation of GB Laves phase has higher creep resistance and creep rupture strength. It confirms our previous finding that the GB Lave has significant effect in increasing creep strength of our model steel.

3.3.4 Stress dependence of creep behavior of solution treated steels

Figure 3-23 ~ 3-26 show the creep tests results of B-doped steel at 1073 K and stresses of 70, 60 and 50 MPa. **Figure 3-23** shows the creep curve of the steel. By decreasing the stress the steady state creep stage is extended significantly. However, the rupture strain remains almost unchanged. The rupture strain of the steel at 50 MPa is 34%, only slightly higher than that tested at 70 MPa (21%). **Figure 3-24** shows the semi-logarithmic plot of creep-rate – time curves. At 50 MPa, after the initial stage the creep rate decreases again until reaches 3 x 10^{-5} h^{-1} at 700 h, then it gradually increases to 7 x 10^{-5} h^{-1} and becomes constant until ruptured at 5160 h, which is more than 1 magnitude longer than that tested at 293 h. At the time this paper was written, the creep test at 60 MPa has not yet ruptured, however it shows the similar behavior to that tested at 50 MPa where the creep rate decreases again after the initial stage. The minimum creep rate obtained at 60 MPa is higher than that tested at 50 MPa, i.e. 1 x 10^{-5} h^{-1}, and the time to reach this minimum is also shorter (t_m = 250 h). Although the creep test is still ongoing, it seems that short after reaching the minimum, the creep rate entering the steady state at slightly higher creep rate ($\dot{\varepsilon}_s$ = 1.3 x 10^{-5} h^{-1}). **Figure 3-25** shows logarithmic scale of the creep-rate – time curves. The creep data on the transient stage of 50 and 60 MPa tests is less scattered than that of 70 MPa. At 60 MPa, the creep rate slowly decreases after the initial load until reaches 3 x 10^{-4} h^{-1} at 1h. The creep rate keeps constant up to 70 h before it decreases again until reaches the minimum. By decreasing stress to 50 MPa, the creep rate decreases at all creep stage, however the creep behavior is similar. The time to reaches the first steady state is the same to that of 60 MPa (1 h), but with lower creep rate 3 x 10^{-4} h^{-1}. However, this steady state stage becomes much longer (up to 300 h), before decreases again and reaches the minimum at 700 h. **Figure 3-26** shows the creep-rate – strain curves of the steels. At 60 MPa, the first steady state stage is reached after 0.03% strain, which lasts until 1% strain. The minimum is reached at 5% strain and the onset of the second stead stage at 7%. Decreasing the stress to 50 MPa does not change the onset and span of the first steady state stage. However, the strain to reaches the minimum and the second steady state stage occur at shorter strain, i.e. at 4% and 6% respectively.

From these results, it can be observed that by decreasing the stress, or in other words decreasing the degree of deformation processes, the balance between strengthening and deformation becomes distorted at longer time and strain, which causes the creep rate to decreases again. It is reasonable to assume that this might be due to the increasing precipitation of GB Laves phase, since lowering the stress allows more time for GB Laves to precipitate before fracture. However, it might also be related to the change of dislocation substructure or density since the onset of the decrease occurs almost at the same strain. It

needs further investigation to clearly understand the mechanisms of these phenomena.

3.4 Summary

The creep behavior of the model steels, in solution treated condition, at 1073 and 973 K have been observed, these are the results obtained in this chapter:

1) The B-doped steel (enhanced precipitation of grain boundary Laves phase by Boron addition) shows higher creep resistance as well as creep rupture strength compared to that of the base steels.
2) B-doped steel exhibits two minimum creep rates under lower stress than 140 MPa at 973 K. The second minimum creep rate contributes to the sluggish creep acceleration, resulting in the pronounced extension of creep rupture life in B-doped steel. This would be related to enhanced precipitation of Laves phase on grain boundaries.
3) B-doped steel exhibits lower minimum creep rates than base steel at 1073 K where no precipitate of GCP phase in grain interior. This indicates that precipitates of Laves phase on GB can increase the creep resistance in the present steels.

References

[1] M. Takeyama, *Mater. Sci. Forum*, 539-543, 3012, 2007.

[2] M. Takeyama: Report of JSPS 123rd Committee on Heat-Resisting Materials and Alloys, **45** (2004), p. 51.

[3] M. Takeyama: Nishiyama Memorial Lecture, No. 194-195, ISIJ (2008), pp. 1-23.

[4] H. Tanaka, M. Murata, K. Kamihara, M. Yamazaki, K. Kimura, H. Abe: Report of JSPS 123rd Committee on Heat-Resisting Materials and Alloys, 47 (2006), p.31.

[5] Special Metals: Technical bulletin, www.specialmetals.com.

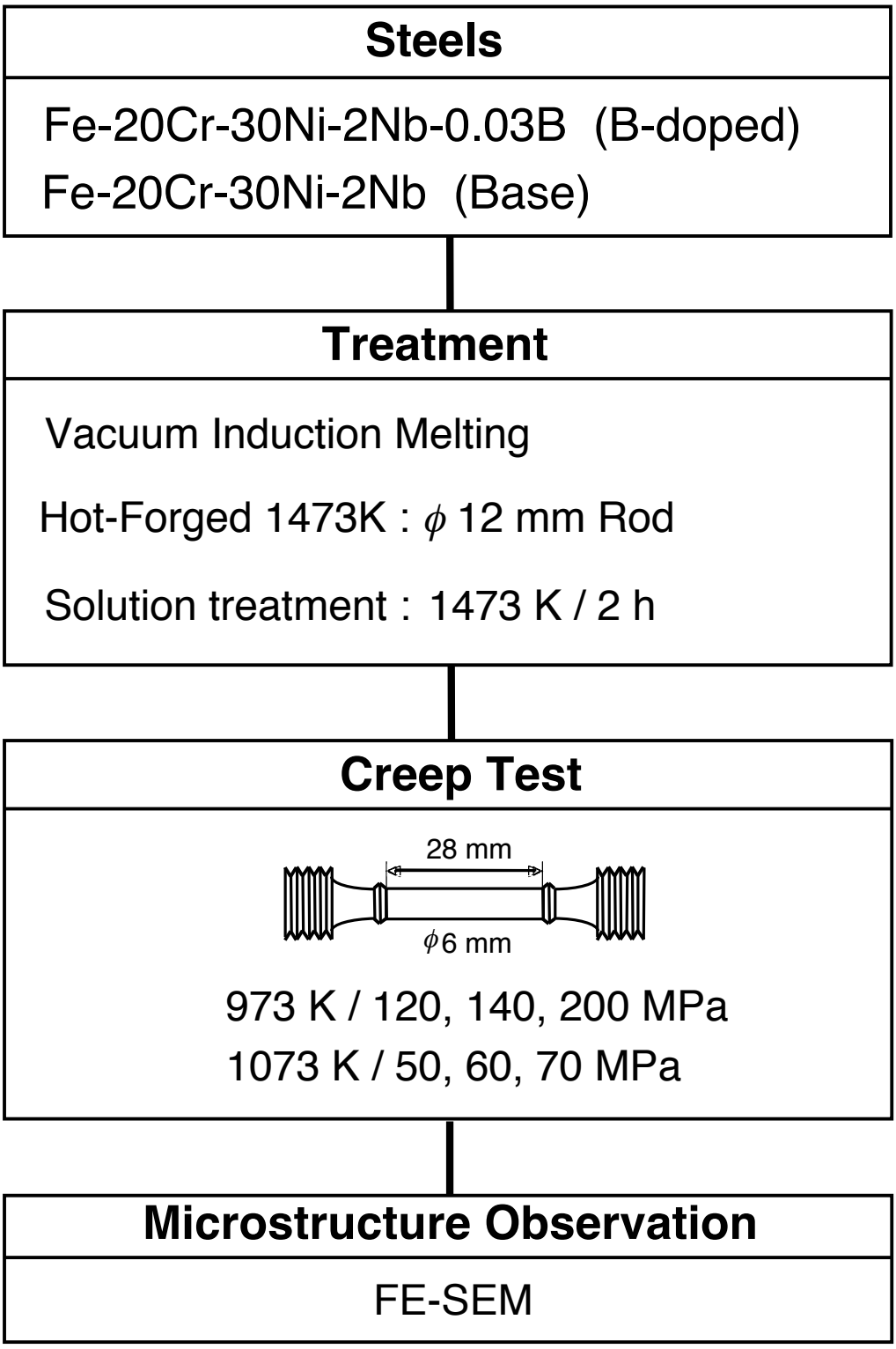

Fig. 3-1 Flow chart of the experimental procedures in the chapter 3.

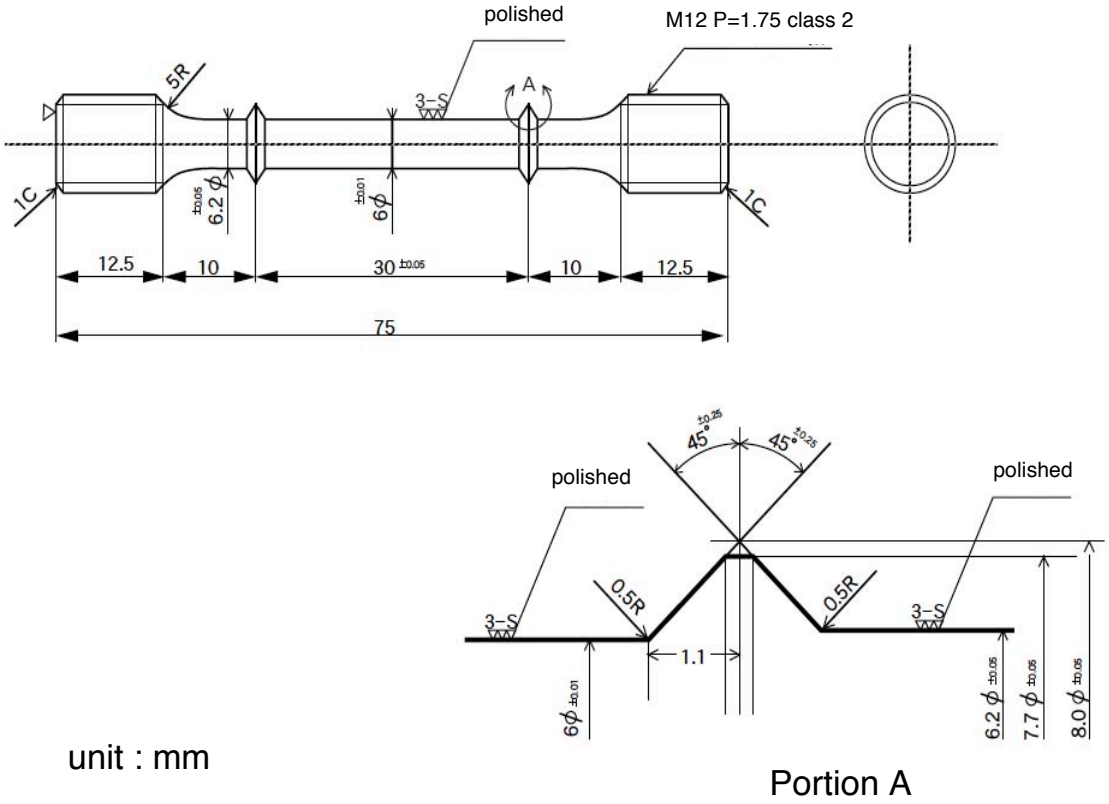

Fig. 3-2 Size specification of the full size creep specimen NO.II-6 regulated in JIS G0567.

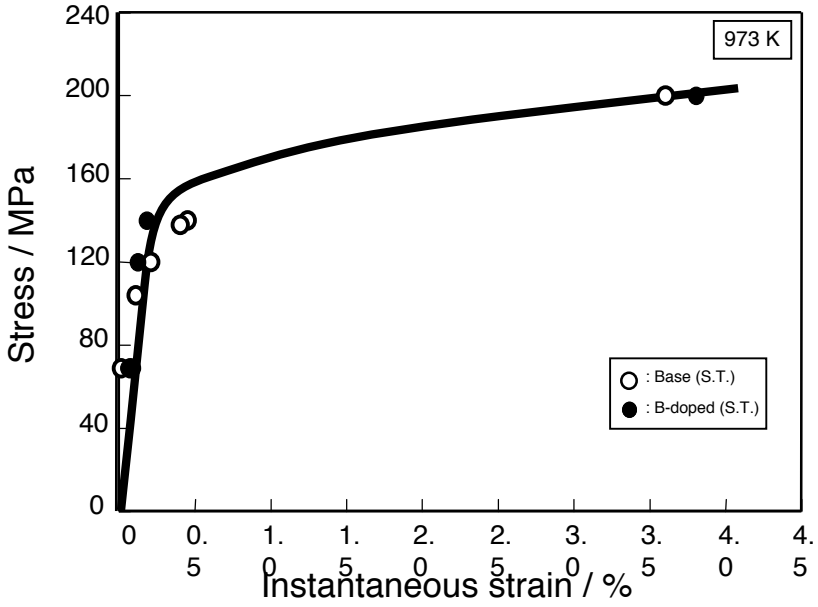

Fig. 3-3 Change in instantaneous strain of solution treated B-dope and base steels as a function of applied stress.

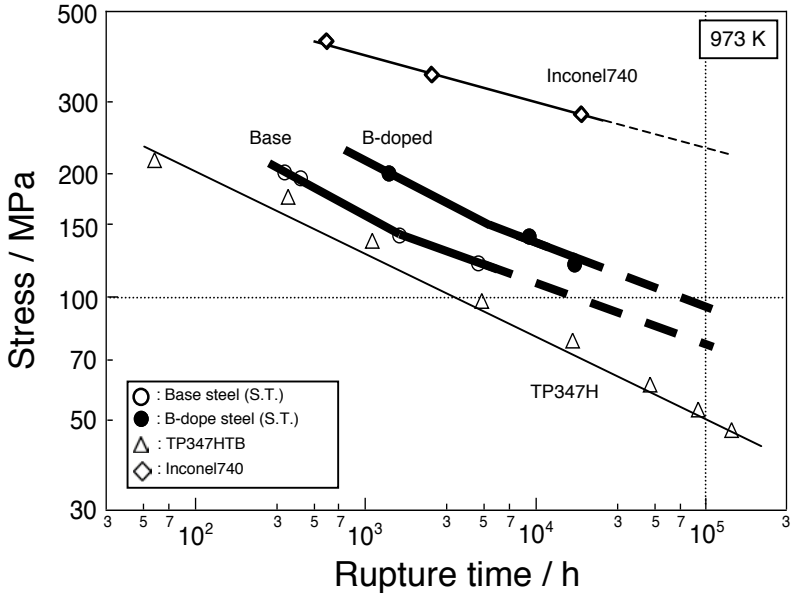

Fig. 3-4 Stress / rupture time curves of solution treated B-dope and base steels in comparison to the commercial heat resistant alloys.

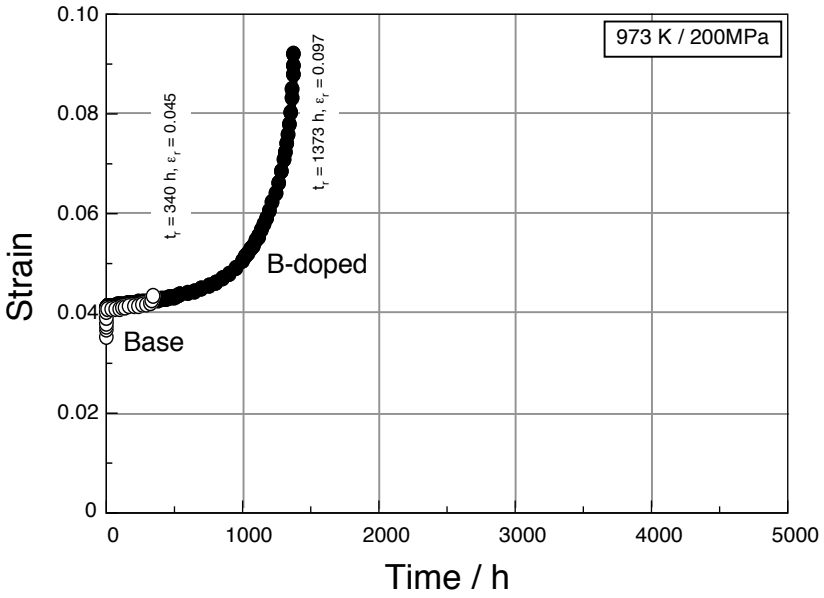

Fig. 3-5 Creep curves of solution treated B-dope and base steels tested at 973 K / 200 MPa.

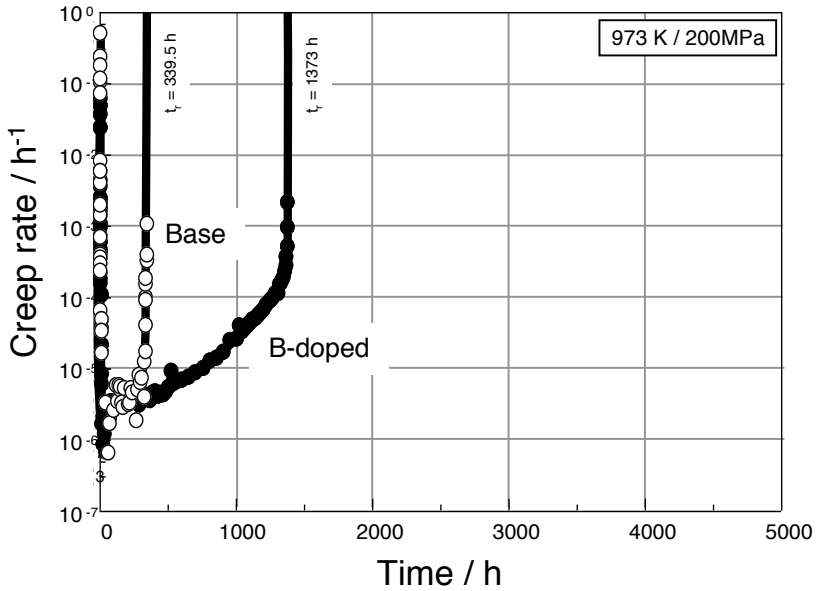

Fig. 3-6 Creep rate / time (linier scale) curves of solution treated B-dope and base steels tested at 973 K / 200 MPa.

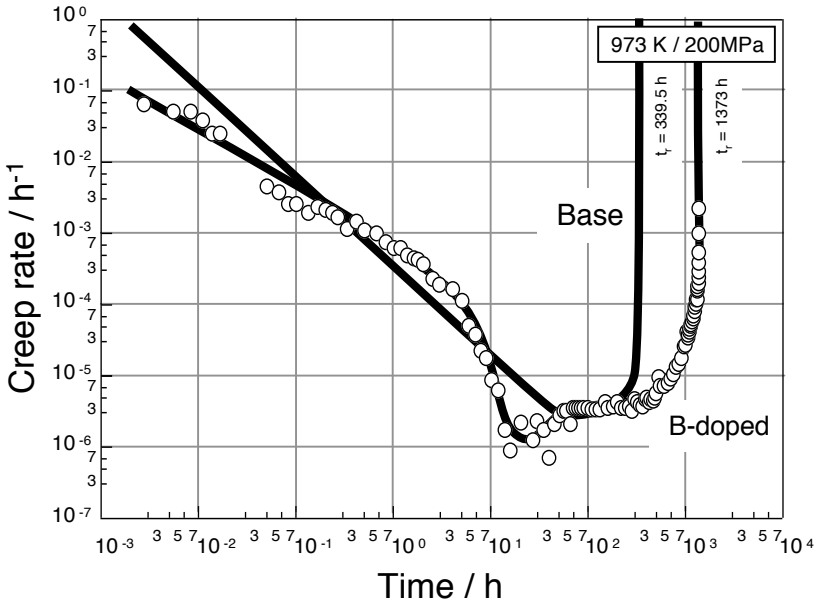

Fig. 3-7 Creep rate / time (logarithmic scale) curves of solution treated B-dope and base steels tested at 973 K / 200 MPa.

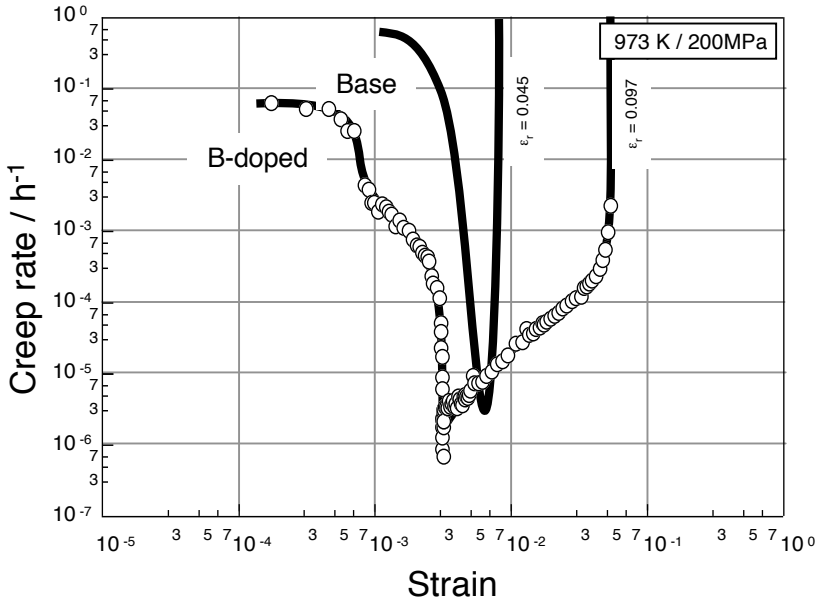

Fig. 3-8 Creep rate / strain curves of solution treated B-dope and base steels tested at 973 K / 200 MPa.

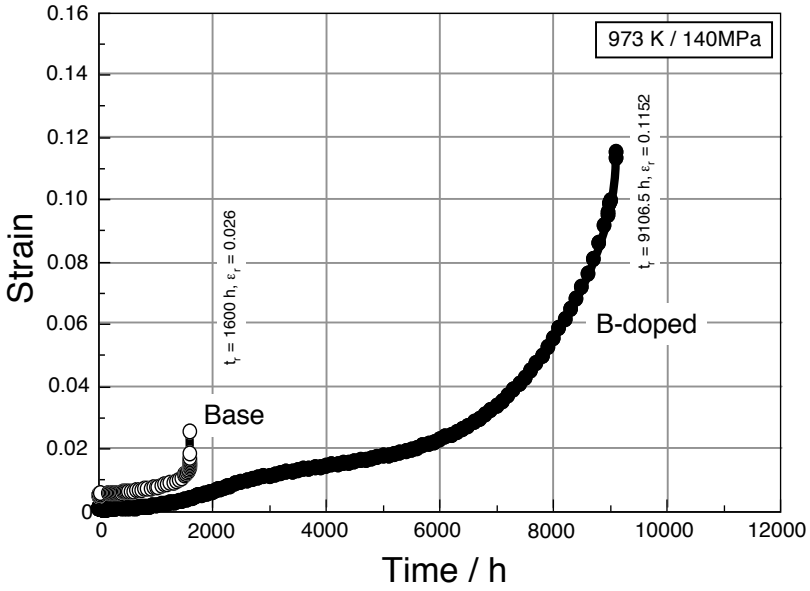

Fig. 3-9 Creep curves of solution treated B-dope and base steels tested at 973 K / 140 MPa.

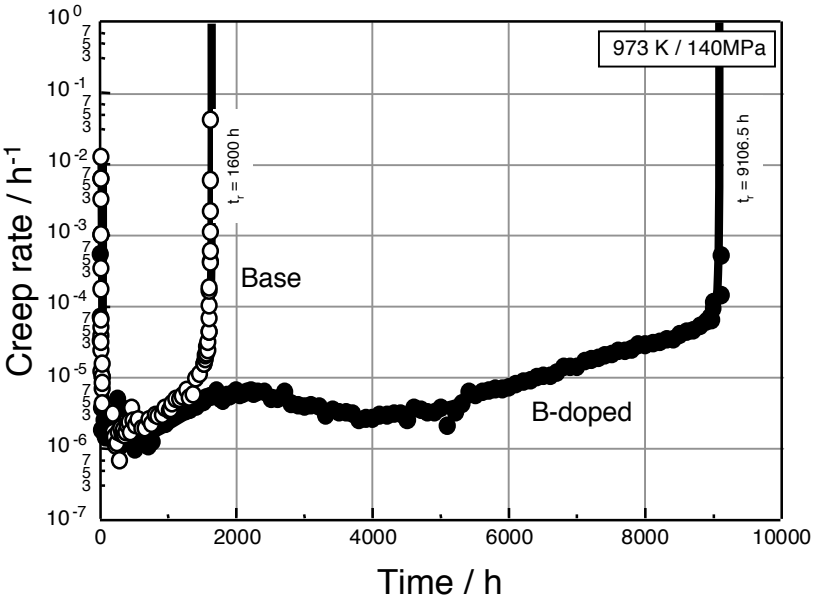

Fig. 3-10 Creep rate / time (linier scale) curves of solution treated B-dope and base steels tested at 973 K / 140 MPa.

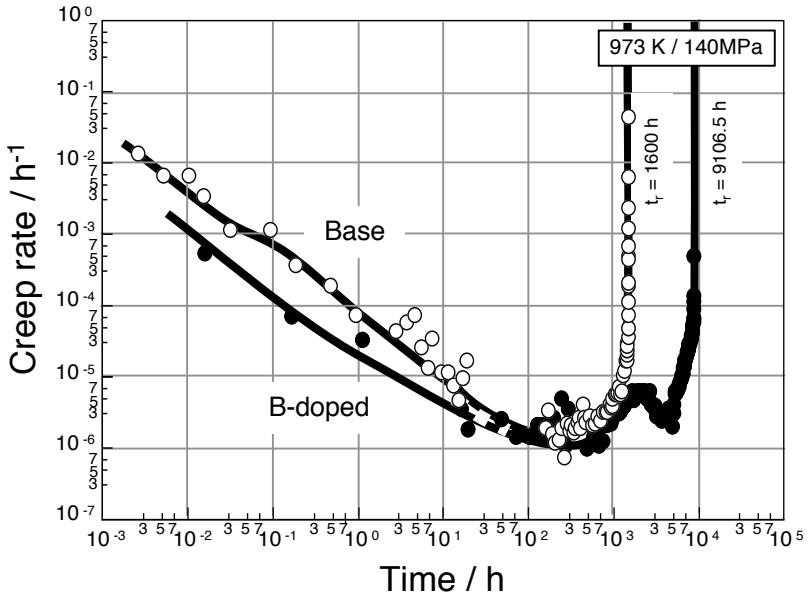

Fig. 3-11 Creep rate / time (logarithmic scale) curves of solution treated B-doped and base steels tested at 973 K / 140 MPa.

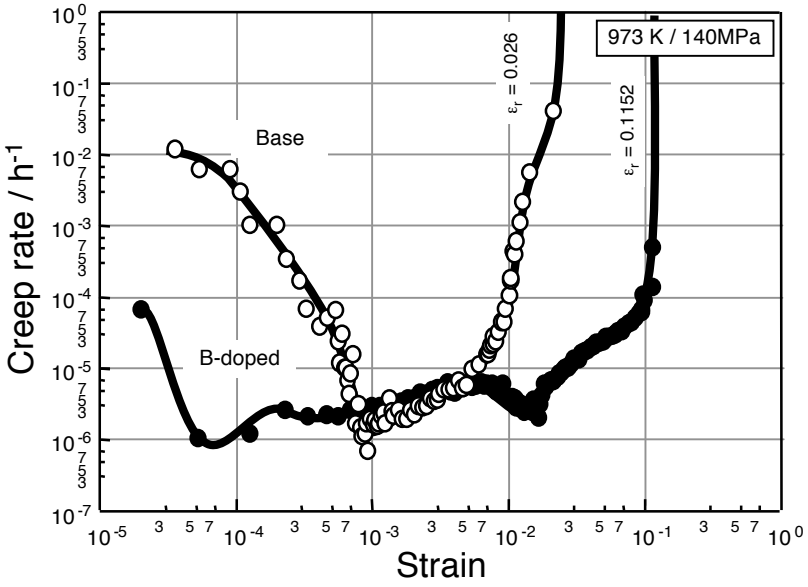

Fig. 3-12 Creep rate / strain curves of solution treated B-dope and base steels tested at 973 K / 140 MPa.

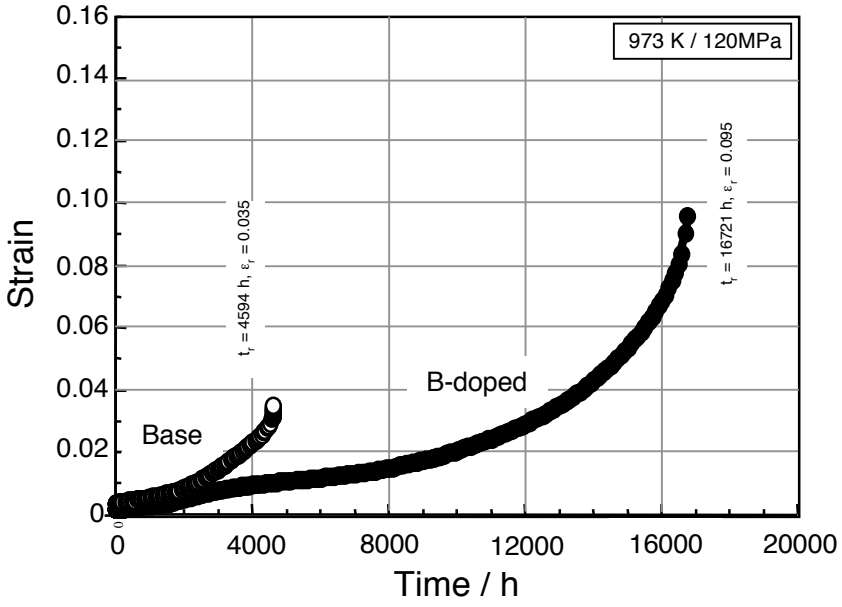

Fig. 3-13 Creep curves of solution treated B-dope and base steels tested at 973 K / 120 MPa.

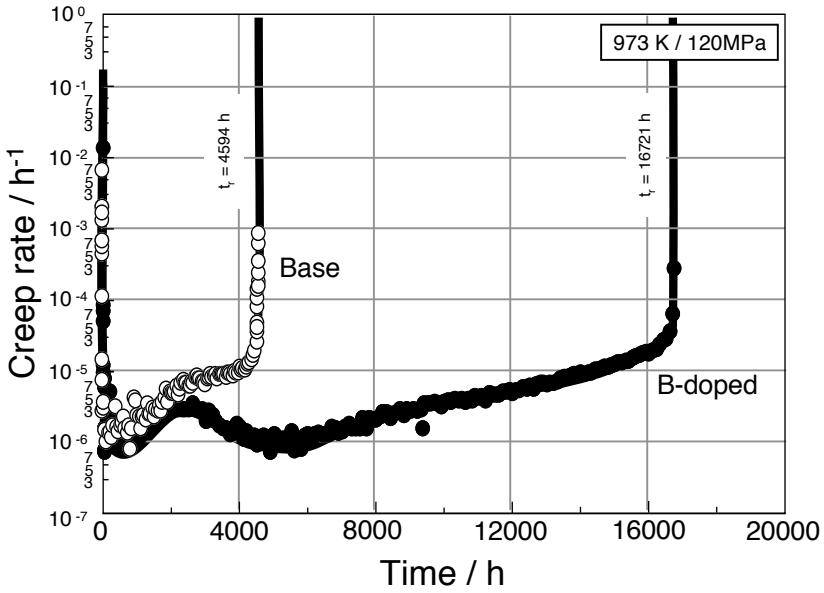

Fig. 3-14 Creep rate / time (linier scale) curves of solution treated B-dope and base steels tested at 973 K / 120 MPa.

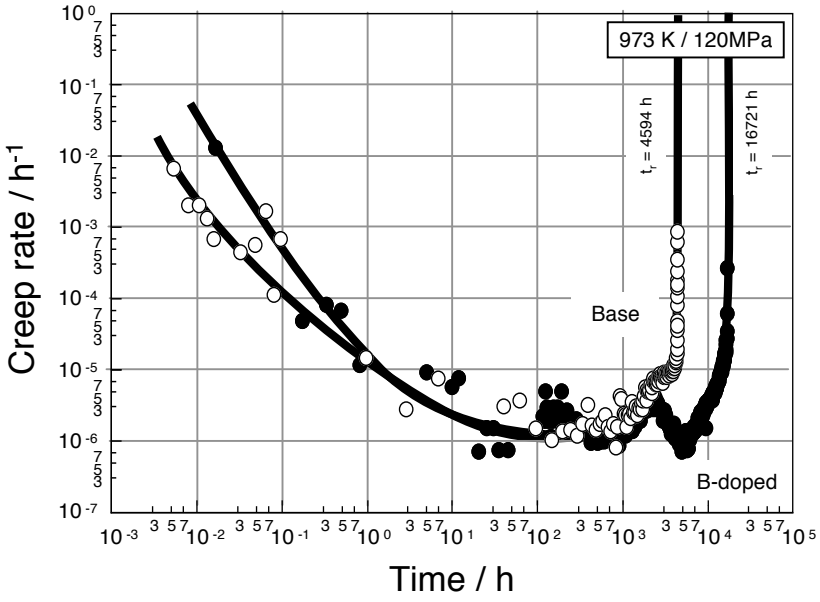

Fig. 3-15 Creep rate / time (logarithmic scale) curves of solution treated B-dope and base steels tested at 973 K / 120 MPa.

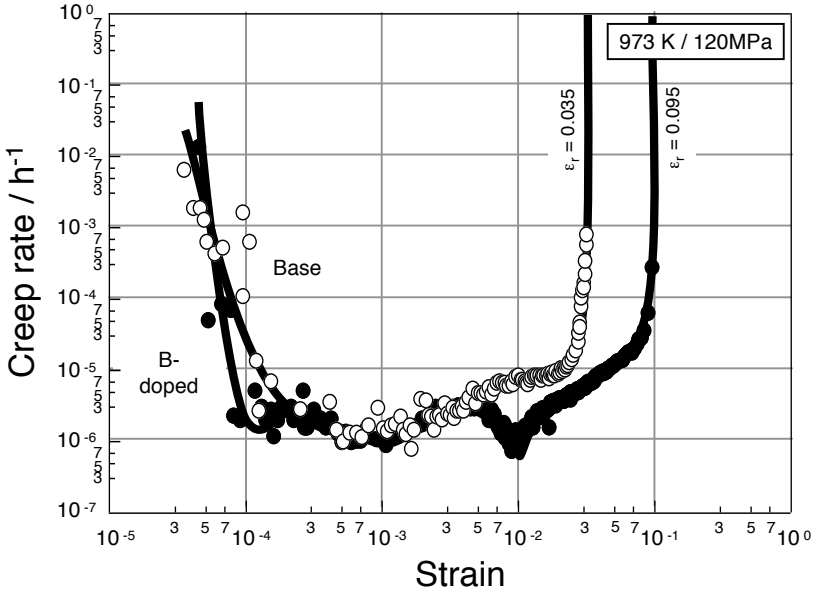

Fig. 3-16 Creep rate / strain curves of solution treated B-dope and base steels tested at 973 K / 120 MPa.

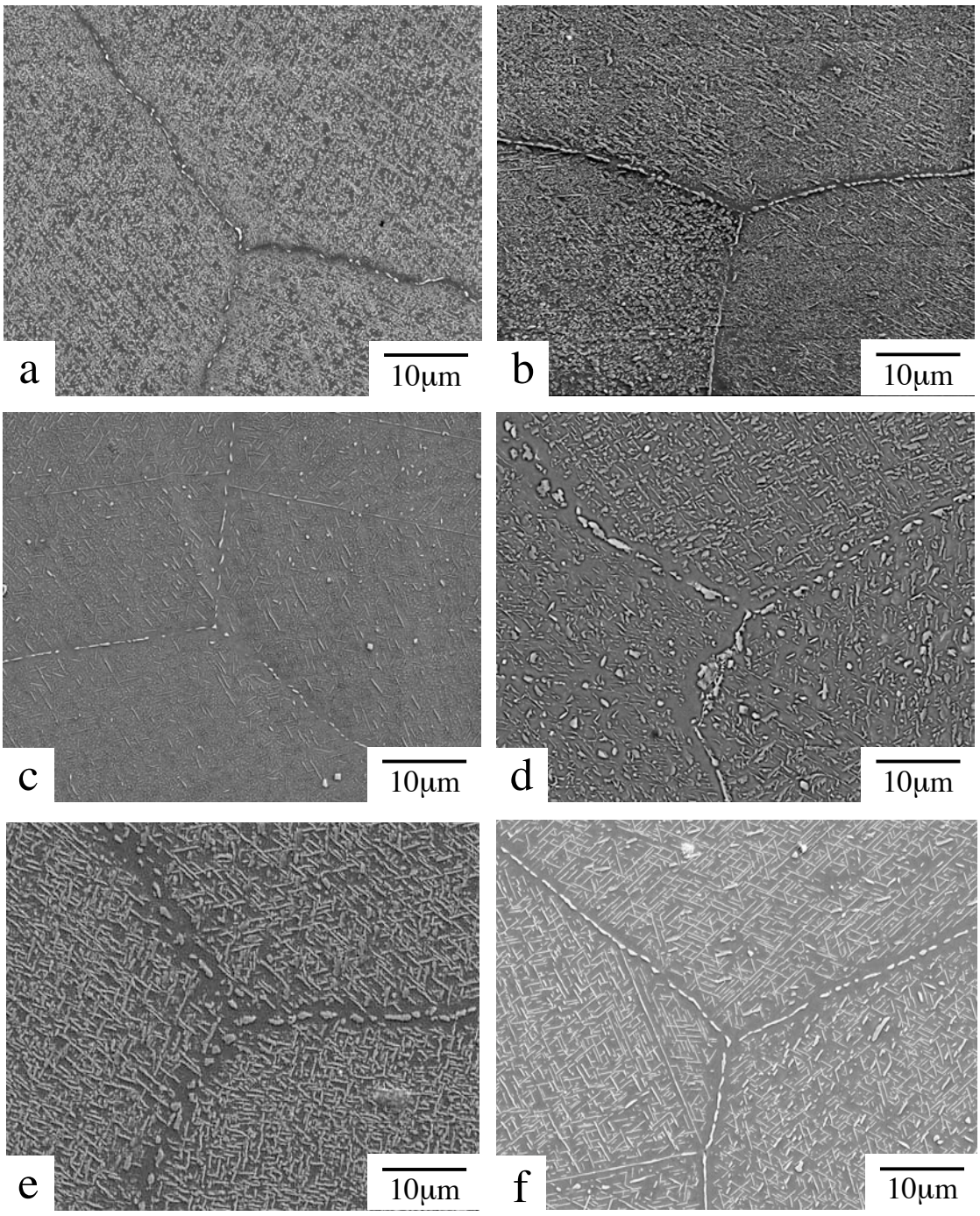

Fig. 3-17 Microstructures of the solution treated (a, c, e) base and (b, d, f) B-dope steels creep ruptured at 973K / (a, b)200, (c, d) 140 and (e, f) 120 MPa; the observed regions were located less than 10 mm from the ruptured surface.

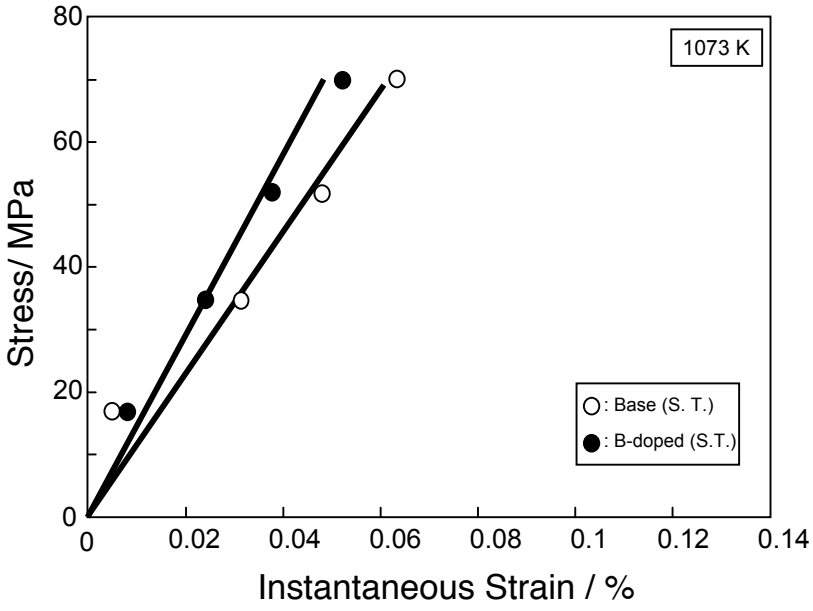

Fig. 3-18 Change in instantaneous strain of solution treated B-dope and base steels as a function of applied stress.

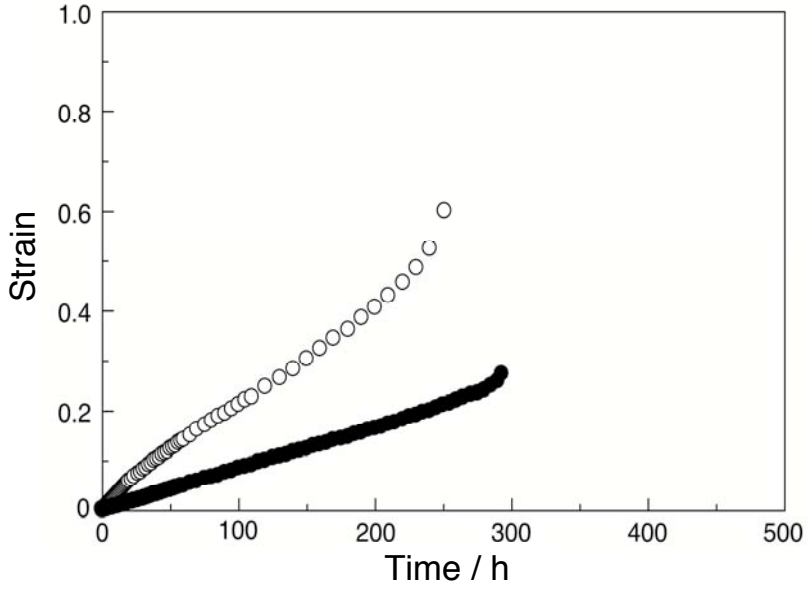

Fig. 3-19 Creep curves of solution treated B-dope and base steels tested at 1073 K / 70 MPa.

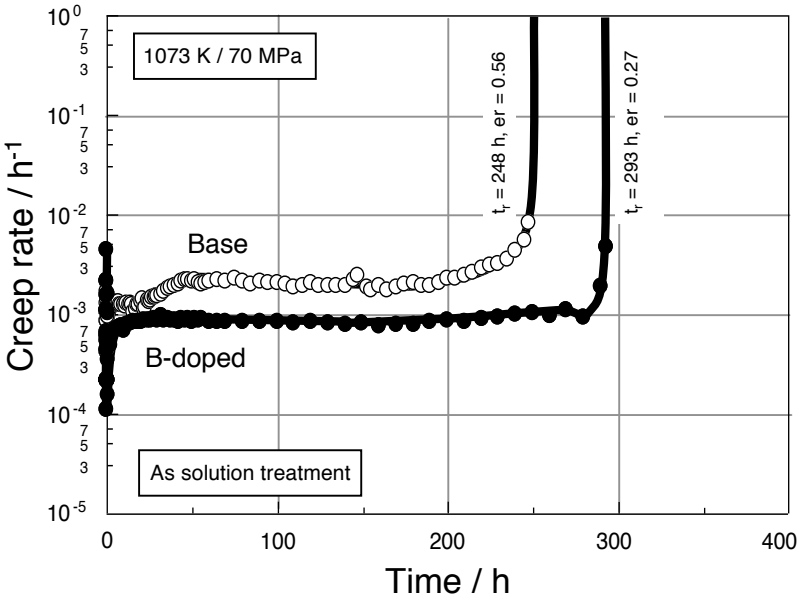

Fig. 3-20 Creep rate / time (linier scale) curves of solution treated B-dope and base steels tested at 1073 K / 70 MPa.

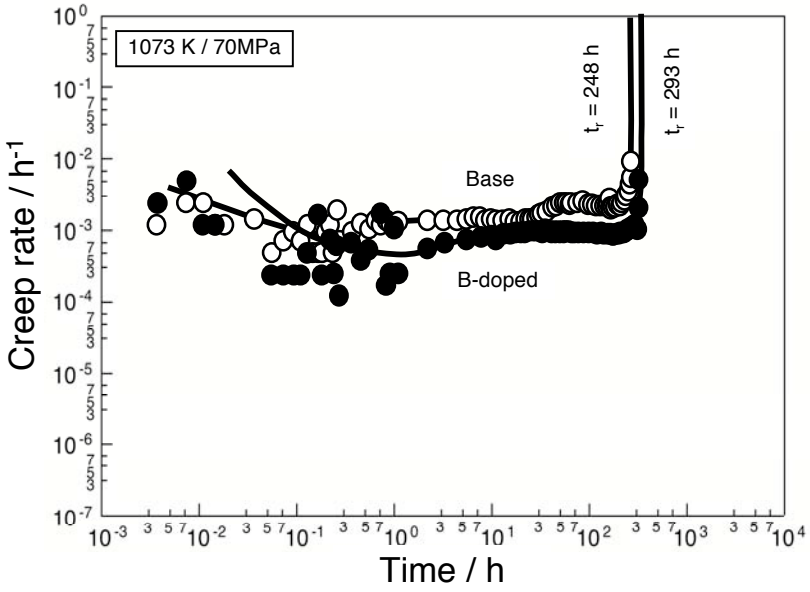

Fig. 3-21 Creep rate / time (logarithmic scale) curves of solution treated B-doped and base steels tested at 973 K / 140 MPa.

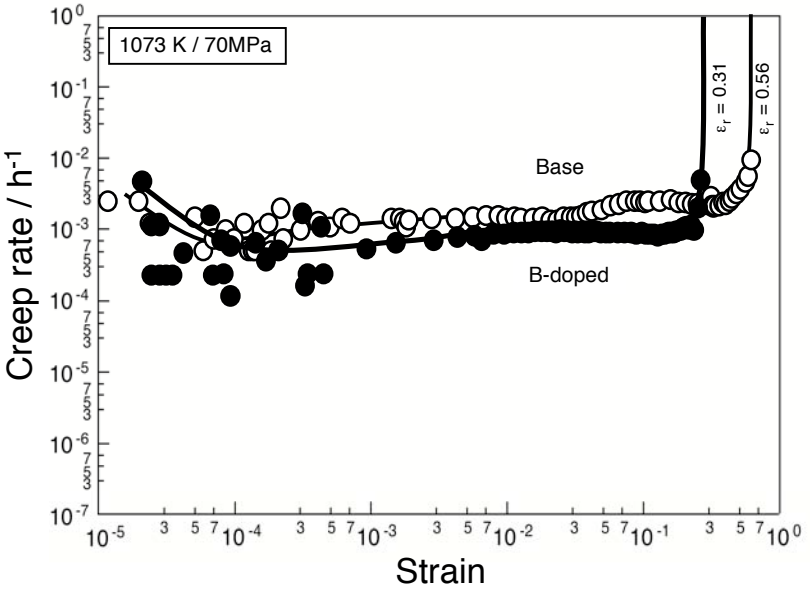

Fig. 3-22 Creep rate / strain curves of solution treated B-dope and base steels tested at 1073 K / 70 MPa.

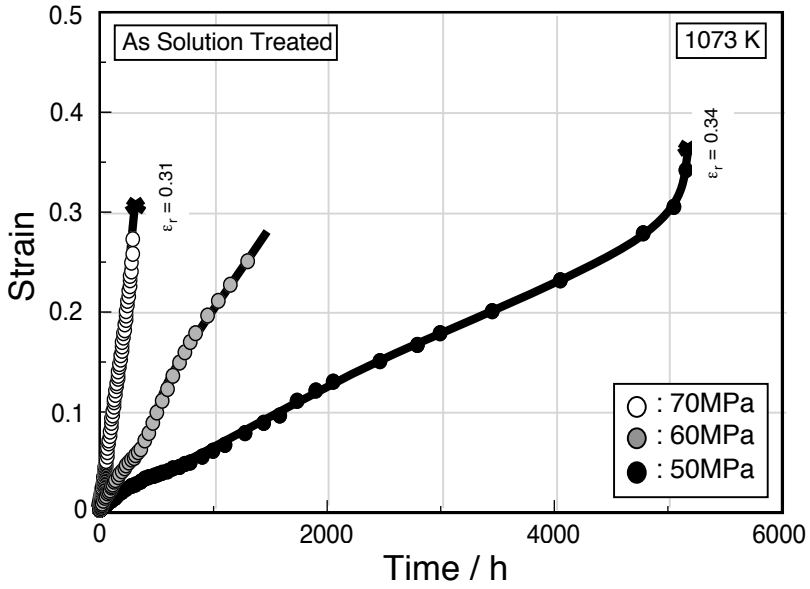

Fig. 3-23 Creep curves of solution treated B-dope tested at 1073 K / 70, 60 and 50 MPa.

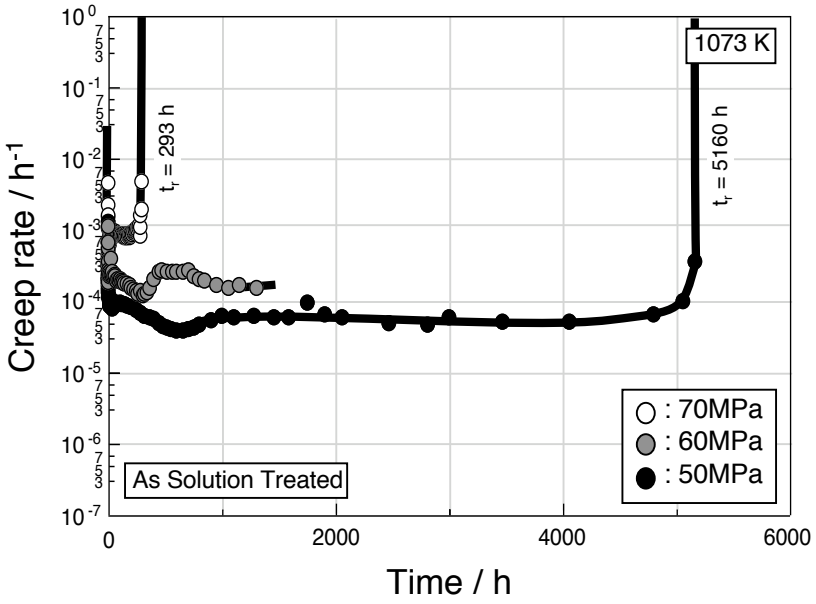

Fig. 3-24 Creep rate / time (linier scale) curves of solution treated B-dope tested at 1073 K / 70, 60 and 50 MPa.

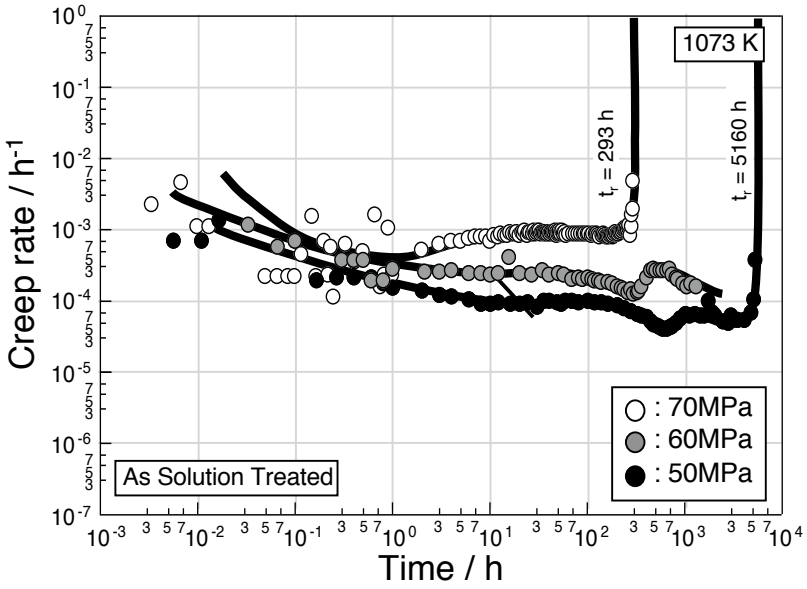

Fig. 3-25 Creep rate / time (logarithmic scale) curves of solution treated B-doped steels tested at 1073 K / 70, 60 and 50 MPa.

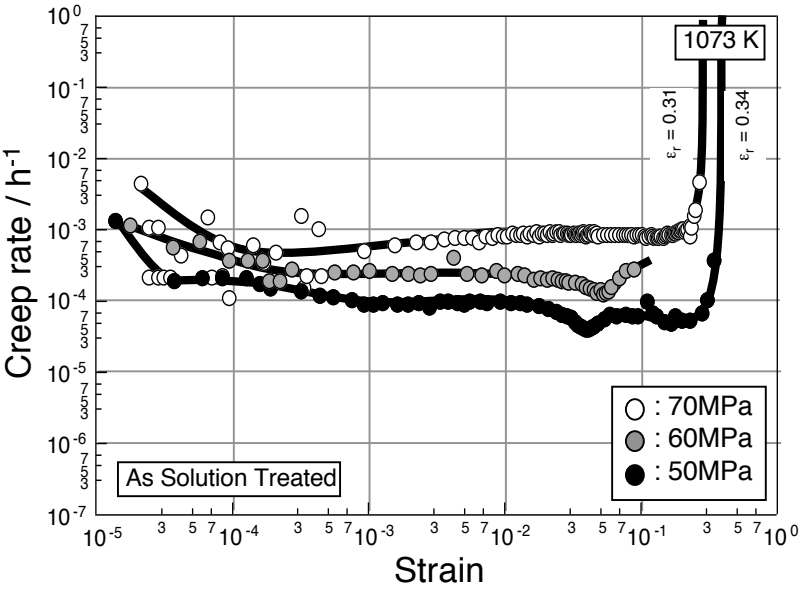

Fig. 3-26 Creep rate / strain curves of solution treated B-dope steel tested at 1073 K / 70, 60 and 50 MPa.

Chapter 4

Creep Strengthening Mechanism by Grain Boundary Laves Phase

4.1 Introduction

In Chapter 3, it has been clarified that the GB Laves phase has significant effect in increasing both creep resistance and creep rupture strength of the steels. However, the strengthening mechanism has still remained unclear. In particular, we have also found an interesting phenomenon in creep behavior of the present steel at 1073 K. At 70 MPa, the base steel shows 2 steady state creep stages, while the B-doped steel only shows single steady state stage (**Fig. 3-21**). However, at lower stress, the B-doped steel also shows 2 steady state creep stages. In addition, the minimum creep rate is present between these 2 steady state stages (**Fig. 3-25**). These phenomena might be also related to the strengthening mechanism by the GB Laves phase. However it needs further investigation to reveal the mechanism.

Unfortunately, it is very difficult to examine the strengthening mechanism in detail from the creep tests of solution treated steels, since the precipitation of GB Laves phase proceeds during creep. Therefore, in this research, we have intentionally pre-aged our steels at 1073 K for up to 1200 h before conducting the creep test. In this approach, we can assume that the area fraction of GB Laves phase does not change during creep test and thus the level of strengthening would be constant independent of time. Therefore, we could analyze more quantitatively the effect of area fraction of GB Laves phase on the creep rate.

In this chapter, we have focused on the creep strengthening mechanism at lower strain, i.e. at the transient and steady state creep. First, the change in creep behavior of the pre-aged steels with stress and time, as well as the area fraction of GB Laves phase will be examined quantitatively. Then, the strengthening mechanism will be proposed based on the microstructure observation and the dislocation analysis on the creep interrupted specimens.

4.2 Experimental Procedure

The flowchart of the experimental procedures used in this study is shown in **Fig. 4-1**. The steels used in this study are B-doped and base steels, which have the same compositions as described in Chapter 2. All steels were prepared by the same processes described in chapter 2, followed by solution treatment to obtain the grain size of 150 μm. Subsequently, the steels were aged at 1073K for up to 1200 h, with area fraction (ρ) of 89%, as shown in **Fig. 2-4**.

For the creep test, the pre-aged rods was machined in the full size creep specimens, the same dimensions specified in **Fig. 3-2**. Tensile creep tests were conduced at 973K at constant stresses of 70 and 140 MPa. The creep tests were also done at 1073 K at constant stress of 70 MPa. Creep interrupted tests were done on the steel tested at 1073 K / 70 MPa at strain of 1 and 25%, in order to observe the change of dislocations structures during creep.

Microstructures after the creep tests were examined by using FE-SEM: JEOL JSM-7000F operating at 15 kV. Dislocation substructures were observed by using JEOL JEM-2010H Transmission Electron Microscope (TEM). TEM discs with 0.15 mm

thickness and 3 mm in diameter were cut out, and then mechanically polished, followed by twin-jet polishing in a solution of ethanol with 20 vol. % perchloric acid at condition fo 25 mA and 248 K. The term area fraction (ρ) is used to interpret the precipitation of GB Laves phase, which was calculated by the same method described in Chapter 2.

4.3 Results

4.3.1 Stress dependence on creep behavior

Figures 4-2 ~ 4-5 show the creep test results of B-doped steel, pre-aged at 1073K / 1200h, and tested at 973 K with different stresses of 140 and 70 MPa. According to **Fig. 2-4**, the area fraction of the steel after pre-aged is 89%, which does not show a significant increase by further aging, thus we can assume constant ρ during creep. Both stresses of 140 and 70 MPa are in the low stress creep region, based on **Fig. 3-3**. **Fig. 4-2** shows the creep curves of the steel. At 140 MPa, the instantaneous strain after loading is 0.2 % and it decreases to 0.04 % by decreasing the applied stress into 70 MPa. The slope of the curves decreases significantly by decreasing the stress from 140 and 70 MPa, resulting in much lower strain in 70 MPa test. The rupture strain of 140 MPa test can reach up to 78%, while at the same time, the creep strain is only shows 2 % under 70 MPa. **Figure 4-3** shows the semi-logarithmic plot of creep rate-time curves. After the transient stage, the creep curve at 140 MPa exhibits long steady-state creep stage at $\dot{\varepsilon}_s = 7 \times 10^{-4}\ h^{-1}$, before finally ruptured at 880 h. The curve at 70 MPa also shows steady state creep stage after the transient stage at $\dot{\varepsilon} = 4 \times 10^{-5}\ h^{-1}$. However, after 400 h, the creep rate suddenly decreases to $1 \times 10^{-5}\ h^{-1}$ and keep a constant till 1000 h. Now, the specimen at 70 MPa is under creep. **Figure 4-4** shows the logarithmic plot of creep-rate - time curves of the steel. At 140 MPa test, after 0.1 h in the transient stage, the creep rate slows down and become constant for short period of time and then decrease again until the steady state stage at 200 h. On the other hand, the creep rate in the transient stage at 70 MPa decreases at to $5 \times 10^{-4}\ h^{-1}$ and then keeps a constant rate, which corresponds to the first steady state stage. The creep rate decreases again at 200h and then reaches a minimum of $10^{-5}\ h^{-1}$, which lasts for several hundreds hour before decreases again into the second steady state stage at 400 h. **Figure 4-5** shows the creep-rate – strain curves of the steel. At 140 MPa, the creep rate at the transient stage slows down after reaching 0.1% of strain and become constant up to 0.3%. Then the creep rate decreases again at constant rate until reaches the steady state creep stage at 20% of strain. At 70 MPa, the first steady state stage is reached at 0.1% strain, which is the same with the strain of constant creep rate of that tested at 140 MPa. However, the first steady state stage of 70 MPa test lasts for longer strain than that tested at 140 MPa. The creep rate then reaches the second stady state creep stage at 1.5% of strain.

4.3.2 Temperature dependence on creep behavior

Figure 4-6 ~ 4-9 show the creep test results of B-doped steel, pre-aged at 1073K /

1200 h, tested at constant stress of 70 MPa and 2 different temperatures of 1073 K and 973 K. Stress of 70 MPa is in the low stress creep region at both temperatures. Although 973 K is in the temperature range for Ni_3Nb formation, it is less likely to occur in the 1073K / 1200 h pre-aged steel since the supersaturated Nb in the matrix after the aging treatment is too low for Ni_3Nb formation, based on **Fig. 1-13**. Therefore, we could assume their microstructures hardly change during creep test. **Figure 4-6** shows the creep curves of the steels. The instantaneous strain of the test at 1073 K is 0.1%, which is higher than that tested at 973 K (0.04%). The curve of the 1073 K test has higher slope than that tested at 973 K, comprising of long steady state creep stage after the transient stage, and followed by the accelerating stage until rupture at 52% strain. The strain of 973 K test, at the rupture time of that tested at 1073 K, is only 1.9%. **Figure 4-7** shows the semi-logarithmic plot of the creep-rate – time curve. While the creep test at 973 K shows 2 steady state creep stage, the creep test at 1073 K shows long steady state creep stage after the transient with $\dot{\varepsilon}_s$ of 6 x 10^{-4} h^{-1}. It followed by slow accelerating stage until rupture at 681 h. **Figure 4-8** shows the logarithmic plot of the creep-rate – time curve. It was revealed that the creep test at 1073 K also shows short steady state creep stage with $\dot{\varepsilon}_s$ of 1.3 x 10^{-3} h^{-1} during the transient stage. The time to reach this first steady state stage is 1 h, which is faster than that tested at 973 K, and it lasts up to 50 h before the creep rate decreases again to reach the second or the longest steady state creep stage. The second steady state creep stage at 1073 K is also reached at 200 h time earlier than that tested at 973 K (400 h). **Figure 4-9** shows the creep-rate – strain curves of the creep tests. At 1073K, the first steady state creep stage occurs at longer strain than that tested at 973 K, that is 0.4% and 0.1% respectively. However, this stage can extend up to 7.5% of strain in 1073 K, which is much longer than that tested at 973 K (up to 1% strain). The strain to reaches the second steady state creep stage is also longer in 1073 K, which occurs at 19.5% of strain.

4.3.3 Creep behavior of steels with different area fractions of GB Laves phase

In order to examine the creep behavior of steels with different area fractions of GB Laves phase (ρ), we have conducted creep tests on several steels with ρ ranging from 40 – 89%. It was obtained by pre-aging the base and B-doped steels at 1073 K for 240 and 1200 h. To clearly observe the effect of area fraction of GB Laves phase, the comparison was conducted using the same aging treated steels, since the supersaturated solution of Nb at 240 h and 1200 h is different and thus contributing to different solid solution strengthening effect during creep.

Figure 4-10 ~ 4-13 show the comparison of the creep behavior of B-doped and base steels, pre-aged at 1073K for 240h, creep tested at 973K /140 MPa. The ρ of the base and B-doped steels after pre-aging are 80% and 39%, respectively. **Figure 4-10** shows the creep curves of the steels. The instantaneous strain of both steels is almost the same, i.e. 0.1%, however following this stage, the strain of the steel with ρ of 80% increases at much

slower rate compared to that of the steel with ρ of 40%. The steel with ρ of 40% is ruptured at strain of 52%, while at this time of rupture, the steel with ρ of 80% only shows limited strain of 5%. Unfortunately, the creep test of the steel with ρ of 80% was stopped after reaching 17% of strain and thus the rupture strain of the steel is unknown. **Figure 4-11** shows the semi-logarithmic plot of creep-rate – time curves of the steels. The steel with ρ of 40% shows steady state creep stage with $\dot{\varepsilon}_s$ of 1.8 x 10^{-3} h^{-1} after the transient stage. The higher ρ steel does not show steady state creep stage as the creep rate keep decreasing until reaches the minimum at 1400 h with $\dot{\varepsilon}_m$ of 4.2 x 10^{-5} h^{-1}. **Figure 4-12** shows the logarithmic scale of creep rate-time curves of the steels. The creep rate of the steel with ρ of 40% decreases sharply to 5 x 10^{-5} h^{-1} within few minutes after the initial stage. Then the creep rate begin to slow down and reach the steady state after 1 h, which lasts up to 135 h before finally accelerated and ruptured at 183 h. On the other hand, the creep rate of the steel with ρ of 80% does not show a significant decrease on the creep rate after the initial load, but after 30 h the creep rate decreases significantly until reaches the minimum. Nevertheless, the creep rate of the steel with higher ρ always shows lower creep rate throughout all testing period. **Figure 4-13** shows the creep-rate – strain curves of the steels. The creep rate of the steel with ρ of 40% decreases sharply after the initial load until reaches 0.05% strain and becomes slow down until the steady state stage at 1% of strain. The creep rate of the steel with ρ of 80% decreases slowly after the initial load, but after 1% of strain it decreases significantly until reaching a minimum at 13% of strain.

Since the creep behavior of the steel with ρ of 80% does not show any steady state creep stage, which is similar to the creep behavior of the solution treated steel; we have conducted TEM observation on the steel interrupted at 17% in strain, as shown in **Fig. 4-14**. The bright field image (**Fig. 4-14 (a)**) revealed very fine stick-shaped precipitates with a length of about 400 nm within the matrix. Further analysis on the precipitate by using SADP with **B** = 110 (**Fig. 4-14 (b)**) shows superlattice diffractions and has the orientation relationship with the γ matrix as:

$$[100] \parallel \langle 100 \rangle_\gamma$$
$$(010) \parallel \{111\}_\gamma$$

This result clearly indicates that the precipitates are Ni_3Nb-δ phase with $D0_a$ structure, which might be formed during the creep test. It is most likely that the concentration of solid solution of Nb within the matrix, after aging at 1073K / 240 h, is still high enough to drive the precipitation of Ni_3Nb during creep test at 973K. This can explain why the creep behavior of the steel is similar to that of the solution treated steel, i.e. does not show any steady state creep stage. The precipitates might form after 30 h of creep test or 1% strain, where the slope of the curve starts to become steeper.

Based on the TEM observation, we extended the pre-aging time of the steels up to

1200 h to reduce the solid solution Nb within the matrix and thus preventing the formation of Ni_3Nb precipitates during creep. The resulting area fractions of GB Laves after aging are 89% for B-doped steel and 52% for the base. **Figure 4-15 ~ 4-18** show the creep test results of the B-doped and base steels, aged at 1073 K / 1200 h and tested at 973 K / 140 MPa. **Figure 4-15** shows the creep curves of the steel. The instantaneous strains of both steels are almost the same, i.e. at around 0.2%. The curves of both steels are also consists of long steady state creep stage after the transient, which are followed by the acceleration stage. However, the higher ρ steel shows lower slope at all creep stages. Surprisingly, the steel with ρ of 89% can reach up to 77% of strain before its rupture, which is almost the same to that of the lower ρ steel with 78% in rupture strain. **Figure 4-16** shows the semi-logarithmic plot of creep rate - time curves of the steels. Both steels show single steady state creep stage, but the steel with higher ρ has lower creep rate and much longer creep rupture life. The steel with ρ of 89% ruptured at 880 h, which is more than 3 times longer than that of the 40% ρ steel (t_r = 258 h). **Figure 4-17** shows the logarithmic plot of creep-rate – time curves of the steels. At the beginning of the transient stage, the creep rate of the steel with ρ of 89% decreases at steeper slope, but becomes slower and has the same slope to that of the steel with lower ρ after 1 h. The steel with ρ of 89% reaches the steady state creep rate of $\dot{\varepsilon}_m$ of 7 x 10^{-4} h^{-1} after 200 h, while the steel with ρ of 52% shows higher steady sate creep rate of 2.8 x 10^{-3} h^{-1}, which is reached just after 10 h. **Figure 4-18** shows the creep-rate – strain curves of the steels. The creep rate of the steel with ρ of 89% is lower than that of 52% at all strain. The steel with ρ of 89% reaches the steady state creep stage at a strain of 19%, which is much longer than that of the lower ρ (ε_s = 3.6%).

The creep tests have been extended into 1073 K by using the same pre-aged steels. **Figure 4-19 ~ 4-22** show the creep test results of the B-doped and base steels, aged at 1073 K / 1200 h and creep tested at 1073K / 70 MPa. **Figure 4-19** shows the creep curves of the steels. Both steels show almost the same instantaneous strain at around 0.01%, which is followed by steady state and acceleration stages. However, the curve of the steel with ρ of 89% has shallower slope than that of the steel with ρ of 52%. The rupture strain of the steel with ρ of 89% is 54%, which is slightly higher than that of the steel with ρ of 52% (ε_r = 52%). **Figure 4-20** shows the semi-logarithmic plot of creep rate - time curves. Similar to the test results at 973K, the steel with higher ρ shows lower creep rate and much longer creep rupture life. The steel with ρ of 89% shows steady state creep rate of 6 x 10^{-4} h^{-1} and rupture life of 681 h, while that with 52% of ρ has steady state creep rate of 1.8 x 10^{-3} h^{-1} and rupture life of 239 h. **Figure 4-21** shows the logarithmic plot of the creep rate – time curves. The creep rate of both steels decreases at the same rate during the transient stage and becomes constant after 1 h, for up to 15 h. The creep rate decreases with increasing time until reaches the second steady state creep. The steel with ρ of 52% reaches the second steady state creep stage at 70 h, which is much earlier than that of higher ρ (200 h). Similar with previous results, the steel with higher ρ shows lower creep rate at all creep

stages. **Figure 4-22** shows the creep-rate – strain curves of the steels. Both steels show similar creep behavior at all strain. The strain to reaches the first steady state creep in both steels is 0.5 %, which extends up to 5% of strain. At 20% strain, the steady-state creep stage is attained in both steels. Nevertheless, the steel with higher ρ shows lower creep rate at all strain compared to that of lower ρ steel.

4.4 Discussion

4.4.1 Governing creep mechanism

In classic creep theory, the creep deformation of metals is usually described to be a function of stress, temperature, time and strain [1] or can be expressed in general forms as:

$$\dot{\varepsilon} = f(\sigma, T, t) \tag{1}$$

$$\text{or} \quad \dot{\varepsilon} = f(\sigma, T, \varepsilon) \tag{2}$$

Which means that at specific stress and temperature, $\dot{\varepsilon}$ describes the creep rate at certain fixed time (equation 1) or at some certain fixed strain (equation 2). When the time and strain are constant, as in the case of steady state or minimum creep, the creep rate will only depend on stress and temperature and can be expressed as:

$$\dot{\varepsilon} = u(\sigma) \cdot v(T) \tag{3}$$

where $u(\sigma)$ describes the dependence of $\dot{\varepsilon}$ with stress, while $v(T)$ describes the temperature dependence. These functions are usually assumed to be independent each other, i.e. the change in creep rate with stress should be the same at all temperature and vice versa. Generally, the temperature dependence is often related to the diffusion rate and obeys Arrhenius's Law:

$$\dot{\varepsilon} \propto \exp -(Q_c / RT) \tag{4}$$

where Q_c is called the activation energy for creep and R is universal gas constant (8.31 $Jmol^{-1}K^{-1}$). On the other hand, the stress dependence is often related to the Norton's Law, i.e. :

$$\dot{\varepsilon} \propto \sigma^n \tag{5}$$

where n is usually called the creep exponent value. Substituting the equation (4) and (5) into (3), then gives

$$\dot{\varepsilon} = A\,\sigma^{n} \exp -(Q_c / RT) \qquad (6)$$

where A is materials constant. This relationship is called the "power law" relationship, which have been widely used to described temperature creep behavior.

It has been proposed that the value of n and Q_c is strongly indicate the mechanism that governs the creep process in metals at certain stress and temperature [1,2]. When n value is equal to 3 ~ 5 and Q_c close to the activation energy for lattice self-diffusion of the metals, the creep process is said to be controlled by dislocation motion, or usually referred as dislocation creep mechanism. On the other hand, when n is equal to 1 ~ 2 and Qc is less than, or equal, to lattice self-diffusion, the creep is controlled by diffusion process, which is generally known as the diffusion creep mechanism.

Based on this theory, we have tried to examine the creep data that have been obtained so far in order to identify the governing creep mechanism in our model steels. **Figure 4-23** shows the creep exponent of the 1073 K /1200 h pre-aged B-doped steel (ρ = 89%), tested at 973 K, in addition to that of solution treated B-doped steel tested at 973 K and 1073 K. The creep exponent was obtained from the slope of the curve between steady state or minimum creep rate and applied stress in logarithmic scale. At 973 K, the solution treated B-doped steel shows creep exponent of 1. However, by increasing the test temperature to 1073K, the creep exponent changes into 5. The low creep exponent at 973 K might be related to the complex interaction between the creep deformation and the precipitation of metastable Ni_3Nb-γ" within the matrix. When Ni_3Nb is eliminated, as in the creep test at 1073 K, the creep exponent indicates the dislocation creep mechanism. To further clarify the results, the creep exponent of 1073K / 1200 h aged B-doped steel at 973K has also been examined. Since the pre-aged steels show 2 steady state creep stages, the examination of creep exponent has been done based on the creep rate of each stages. The creep exponent measured from both lower strain (first steady state) and higher strain (second steady state) creep rate shows the same value, i.e. n = 5. This result is similar to that of solution treated steel at 1073 K, which indicates that the creep mechanism in the model steel is controlled by dislocation motion.

However, the creep exponent alone is not enough to justify the creep mechanism. As mentioned previously, for the dislocation creep mechanism to occur, the creep activation energy should be near or equal the activation energy for the lattice self-diffusion. **Figure 4-24** shows the creep activation energy of 1073K / 1200 h aged B-doped steel at 70 MPa. The creep activation energy was calculated from the slope of log $\dot{\varepsilon}_s$ vs. 1/T, based on equation (4). Similar to the examination of creep exponent, the measurement of activation energy of the pre-aged steel was done on both steady state creep stages. Based on the creep rate at lower strain region, the creep activation energy is equal to 325.3 kJ mol^{-1}, which is close to the activation energy of lattice self-diffusion of γ-Fe (ΔH_{SD} = 291 kJ mol^{-1} [3]). On the other hand, the calculated creep activation energy from the creep rate at high strain

region is equal to 347.7 kJ mol^{-1}. It is clear from these results that the governing mechanism in the model steel is dislocation creep. The higher activation energy in the second steady state creep stage might be the result of another process that occur at high strain, for instance dislocation-dislocation interactions that restrict the dislocation movement and thus increasing the energy for further deformation.

4.4.2 Effect of Area Fraction of GB Laves Phase on Creep Rate

Based on the previous analysis, the "power law" creep equation seems to be satisfactory to describe the creep behavior of our model steel. However, the equation fails to explain the change in creep rate with the area fraction of GB Laves phase, as shown in the creep test results in section 4.3.3. The creep tests clearly indicate that the creep rate also depends on the area fraction of GB Laves phase (ρ), i.e.

$$\dot{\varepsilon} \propto f(\rho) \tag{7}$$

This dependency has not been considered in general creep theory, while we found it has strong correlation. Therefore we have tried to analyze more quantitatively the relationship between the creep rate and area fraction of grain boundary Laves phase.

Kondo et. al [7] has shown the experimental result that the creep rate is inversely proportional to the grain size, as follows;

$$\dot{\varepsilon} \propto d^{-1} \tag{8}$$

where the grain size is also inversely proportional to the grain boundary area, which means that the smaller the grain size, the higher the grain boundary area and thus can be expressed as

$$d \propto S^{-1} \tag{9}$$

If the precipitate is present along the grain boundary, the grain boundary area for deformation will be reduced by the area fraction of the GB precipitates, i.e.

$$S = S_o\,(1-\rho) \tag{10}$$

where S and S_o are the effective grain boundary area and the grain boundary area without precipitates, respectively. The effective grain boundary means the grain boundary area that is not covered by the precipitates and thus become the area that effectively takes part in deformation.

From the equations (8) and (9) it can be seen that the creep rate is proportional to the grain

boundary area and substituting this into equation (10) we can get the relationship:

$$\dot{\varepsilon} = \dot{\varepsilon}_o (1-\rho) \tag{11}$$

where $\dot{\varepsilon}_o$ is the creep rate at $\rho = 0$. Takeyama [4-6] has proposed this concept as "Grain Boundary Precipitation Strengthening" (GBPS).

Figure 4-25 shows the normalized creep rate ($\dot{\varepsilon}/\dot{\varepsilon}_o$) plotted as function of ρ of the model steels creep tested at 973K / 140 MPa and 1073K / 70 MPa. For the creep at 973K / 140 MPa, only the data of 1073K / 1200 h pre-aged steels was used since the shorter time aged steels show precipitation of Ni_3Nb during creep, as shown previously. All the data, both from 973 K and 1073K-creep tests, fit reasonably well with the relationship, i.e. the creep rate decreases with increasing ρ, independent of stress and temperature. It clearly shows that there is a strong relationship between the area fractions of GB Laves phase and the creep rate. Based on these results, we proposed that the GB Laves phase increase the creep resistance through the "*grain boundary precipitation strengthening mechanism*".

4.4.3 Effect of GB Laves Phase on Dislocation Motion

Although it is already clear that the GB Laves phase increases the creep resistance through the GBPS, the mechanism has still remained unclear. In order to investigate the mechanism into more detail, we have conducted creep-interrupted test on the steel with ρ of 52%, tested at 1073K / 70 MPa, at strain of 1 and 25%, as shown in **Fig. 4-26**. The strain of 1% is located on the first steady state creep stage, while 25% is on the second steady state creep stage. **Fig. 4-27** shows the TEM bright field image of the area near the grain boundary at 1% strain. The picture was taken in the two-beam condition of (101) with B = 111. From the picture, it can be observed that some of dislocations were piled-up near the GB Laves. We have further analyzed the Burger's vector of the dislocations by using the invisibility criteria:

$$\mathbf{b} \cdot \mathbf{g} = 0 \tag{12}$$

where **b** and **g** are the Burger's vector and diffracting vector, respectively. The equation means that if the Burger's vector of the dislocation is perpendicular to the diffraction vector, the contrast of the dislocation will become weak, i.e. dislocation will be invisible. This can be used to determine the Burger's vector by imaging the same dislocations with different diffraction vectors and observing the contrast. In the FCC matrix, the Burger's vector of perfect dislocation in the primary (111) slip plane can be identified by observing the dislocation's contrast using B=111 at 3 different g vector of $20\bar{2}$, $02\bar{2}$ and $\bar{2}20$. **Figure 4-28** shows the determination of Burger's vector of the dislocations in the 52%-ρ steel, creep tested at 1073K / 70 MPa and interrupted at strain of 1%. The dislocations are clearly

visible at **g** of $20\bar{2}$ and $\bar{2}20$, but become invisible at $02\bar{2}$. From all the possible Burger's vectors in the primary (111) slip plane, the observation results match with the Burger's vector of ½ (011). **Figure 4-29** shows the TEM bright field image of the area near the grain boundary at 25% strain. At this creep stage, it can be observed very high density of dislocations piled-up at the GB Laves phase. The determination of the Burger's vector of these dislocations was unsuccessful since not all dislocations can be made invisible by changing the diffracting vectors. Then, it is suggested that these pile-ups might be consisted of dislocations on various slip planes.

Based on these results, we have proposed the strengthening mechanism as shown in schematic illustrations in **Fig. 4-30**. At low strain region, the GB Laves phase restricts the dislocation motion that causes the dislocations to be piled up at the precipitates. Then the creep deformation can only proceed through dislocation climb, which is assisted by diffusion of vacancies into the dislocations. This is in good agreement with the results of measurement of creep activation energy that shows the value near the lattice self-diffusion of the γ-Fe. However, with increasing strain, the diffusion of vacancies cannot longer accommodate the dislocation movements, since a number of dislocations increase significantly. Therefore, for further creep deformation, the secondary slip would be activated on different planes. The dislocations on these different slip planes would interact each other and become tangled, which further impede the dislocation movements. This can explain the drop of the creep rate at higher strain. In summary, the GB Laves phase increases the creep resistance by restricting the dislocation movements around the grain boundaries.

4.5 Summary

The role of grain boundary Laves phase on creep strengthening mechanism has been examined, these are the results obtained in this chapter:

1) The creep exponent of the steel is equal to 5 and the creep activation energy is close to that the lattice self-diffusion of γ-Fe, indicating the creep process is governed by dislocation creep mechanism.
2) The creep rate decreases with increasing the area fraction of GB Laves phase following the equation of:

$$\dot{\varepsilon} = \dot{\varepsilon}_o (1-\rho)$$

   which is proposed as Grain Boundary Precipitation Strengthening Mechanism.
3) The GB Laves phase increases the creep resistance by restricting dislocation motion around grain boundaries.

References

[1] R. W. Evans and B. Wilshire: Introduction to Creep, The Institute of Materials, (1993).

[2] R. W. Hertzberg: Deformation and Fracture Mechanics of Engineering Materials, John Wiley & Sons, (1976).

[3] Hiroshi Oikawa: Lattice Self-Diffusion in Solid Iron (1982).

[4] T. Matsuo, M. Takeyama, M. Kikuchi and R. Tanaka: TMS-AIME Technical paper, (1986), F86-10.

[5] T. Matsuo, M. Kikuchi and M. Takeyama: Strengthening Mechanisms of Ni-Cr-W Based Superalloys for Very High Temperature Gas Cooled Reactors, Proc. 1st Inter. Conf. Heat-Resistant Materials, (1991), 601.

[6] M. Takeyama, NMS, ISIJ, 194·195, 1(2008).

[7] Y. Kondo, T. Matsuo, T. Shinoda, R. Tanaka, Tetsu-to-Hanane, 65(1979), 174.

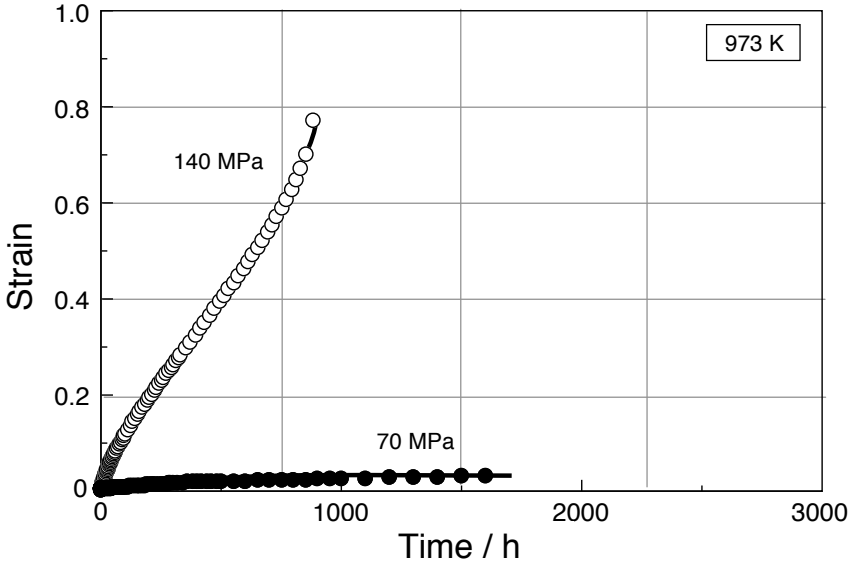

Fig. 4-2 Creep curves of 1073K / 1200h pre-aged B-doped steels tested at 973K with stresses of 70 and 140 MPa

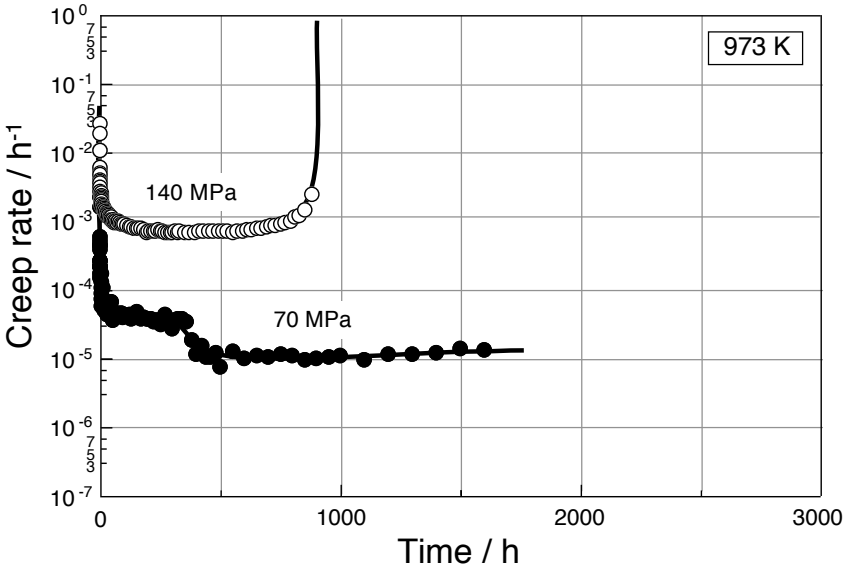

Fig. 4-3 Creep rate / time (linier scale) curves of 1073K / 1200h pre-aged B-dope steel tested at 973 K with stresses of 70 and 140 MPa

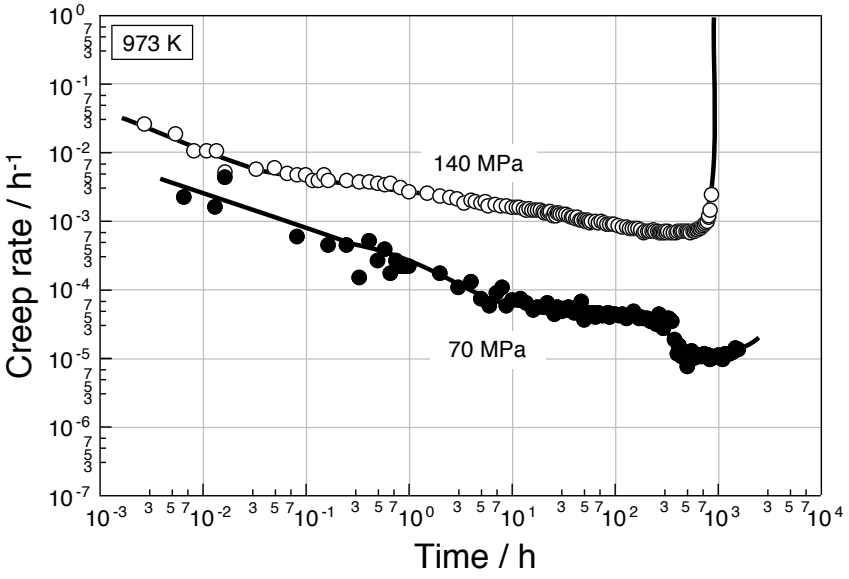

Fig. 4-4 Creep rate / time (logarithmic scale) curves of 1073K/1200h pre-aged B-doped steel tested at 973K at stresses of 70 and 140 MPa.

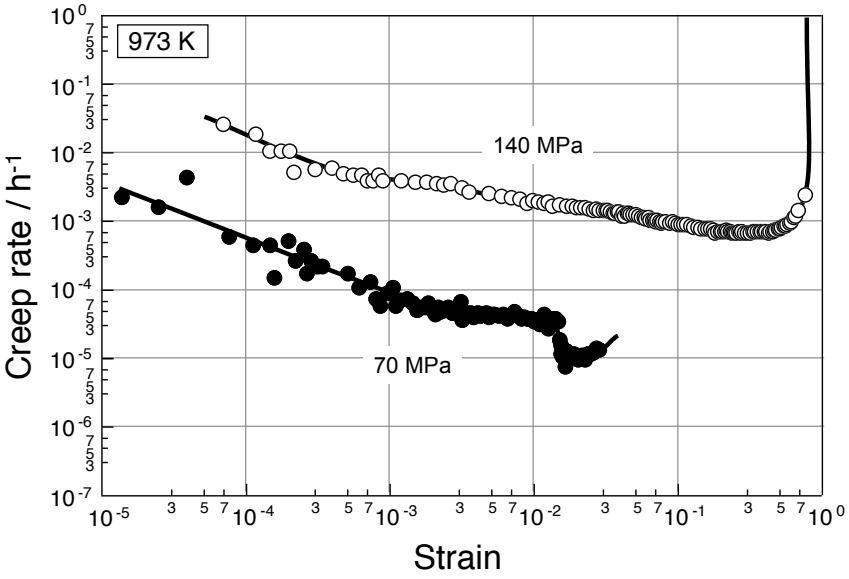

Fig. 4-5 4 Creep rate / strain curves of 1073K/1200h pre-aged B-doped steel tested at 973K at stresses of 70 and 140 MPa

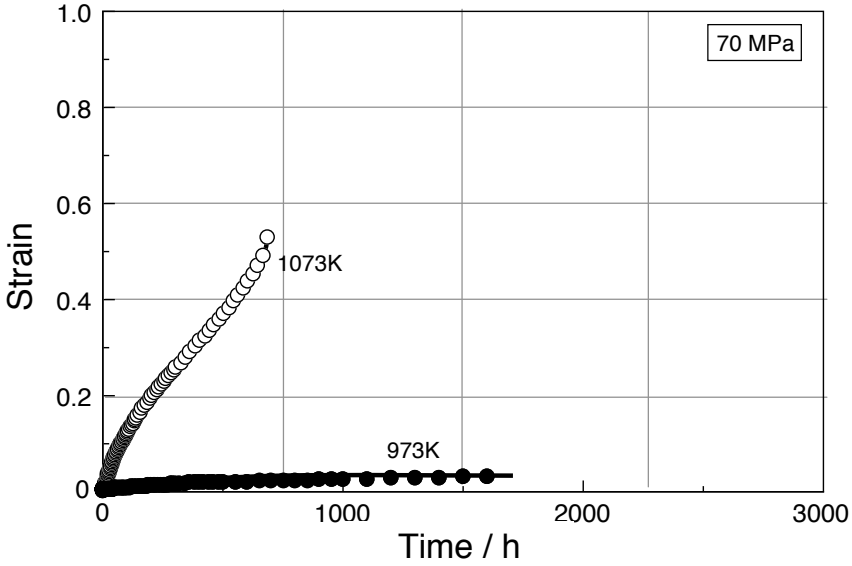

Fig. 4-6 Creep curves of 1073K / 1200h pre-aged B-doped steels tested at stress of 70 MPa and temperature of 973K and 1073 K.

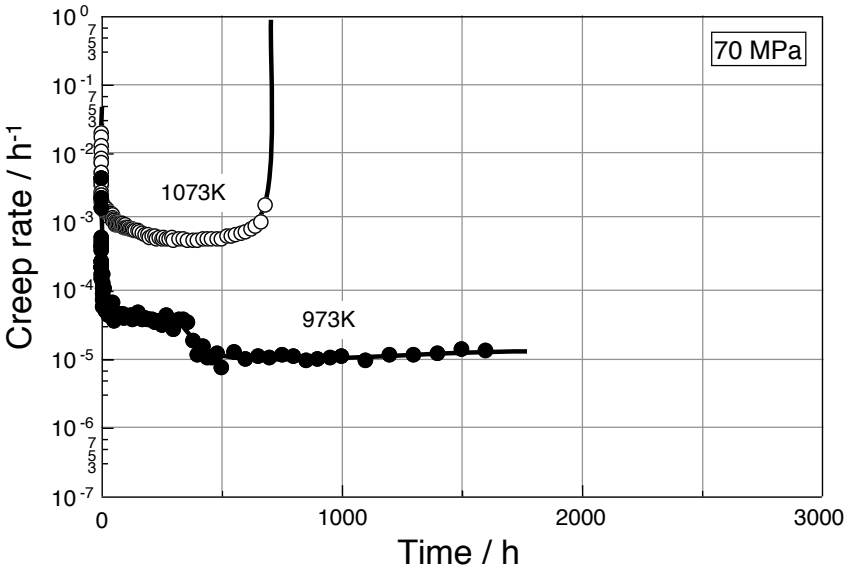

Fig. 4-7 Creep rate / time (linier scale) curves of 1073K / 1200h pre-aged B-doped steels tested at stress of 70 MPa and temperature of 973K and 1073 K.

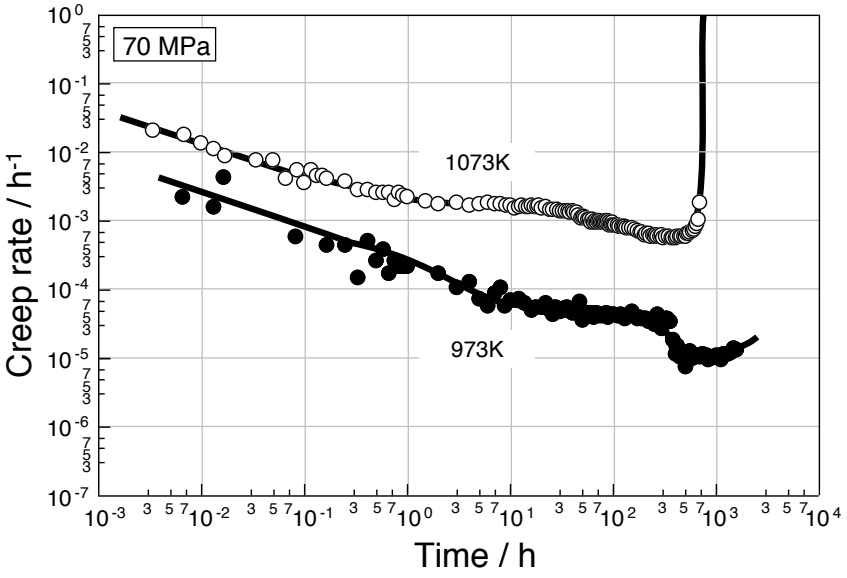

Fig. 4-8 Creep rate / time (logarithmic scale) curves of 1073K/1200h pre-aged B-doped steel tested at stress of 70 MPa and temperature of 973 K and 1073 K.

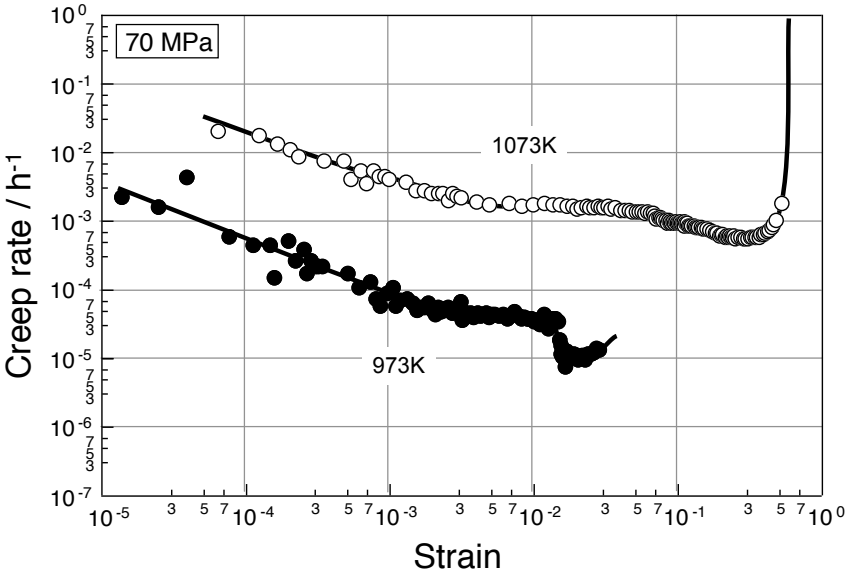

Fig. 4-9 Creep rate / strain curves of 1073K/1200h pre-aged B-doped steel tested at stress of 70 MPa and temperature of 973 K and 1073 K.

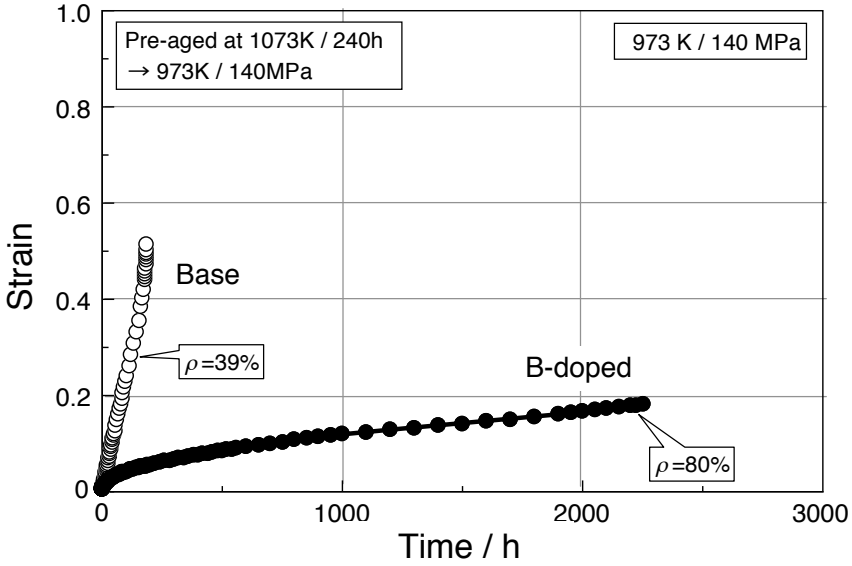

Fig. 4-10 Creep curves of 1073K / 240h pre-aged B-doped and base steels tested at 973K / 140 MPa

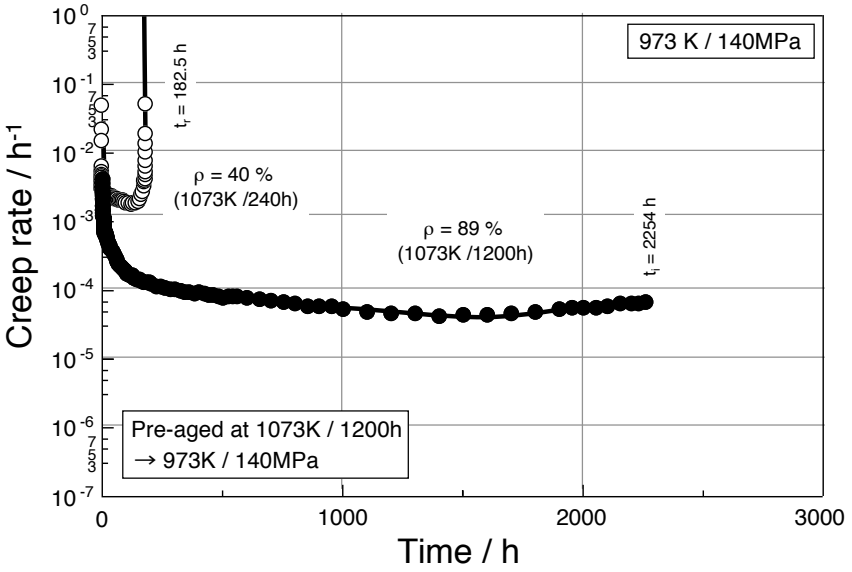

Fig. 4-11 Creep rate / time (linier scale) curves of 1073K / 240h pre-aged base B-doped steels tested at973K / 140 MPa.

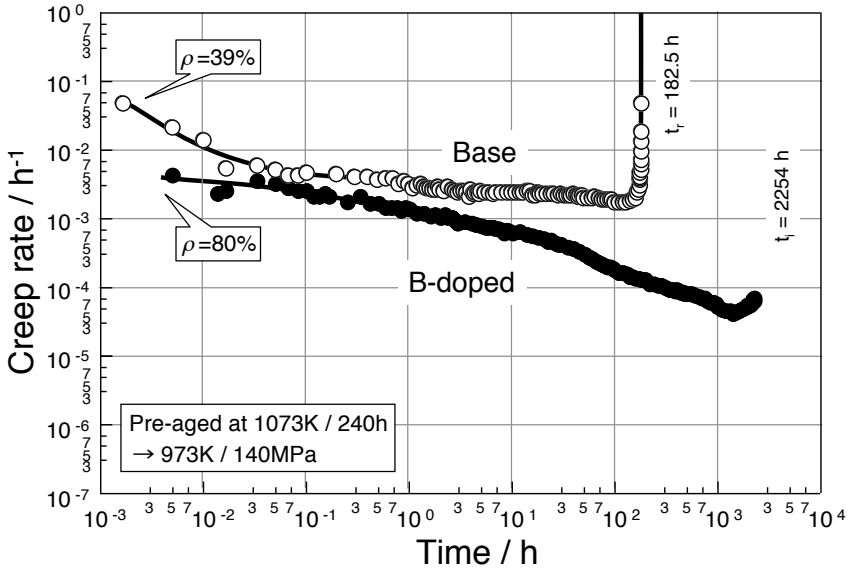

Fig. 4-12 Creep rate / time (logarithmic scale) curves of 1073K/240h pre-aged base and B-doped steel tested at 973K / 140 MPa.

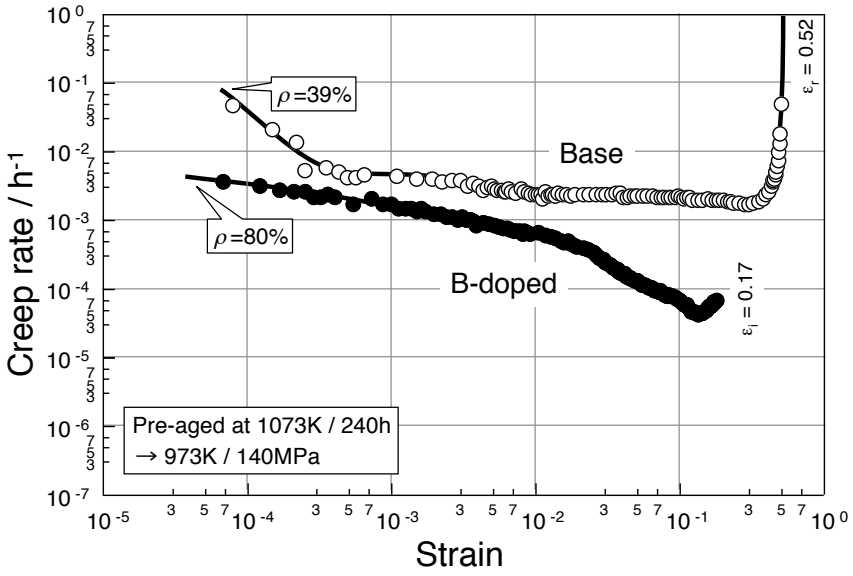

Fig. 4-13 Creep rate / strain curves of 1073K/240h pre-aged base and B-doped steel tested at 973K / 140 MPa.

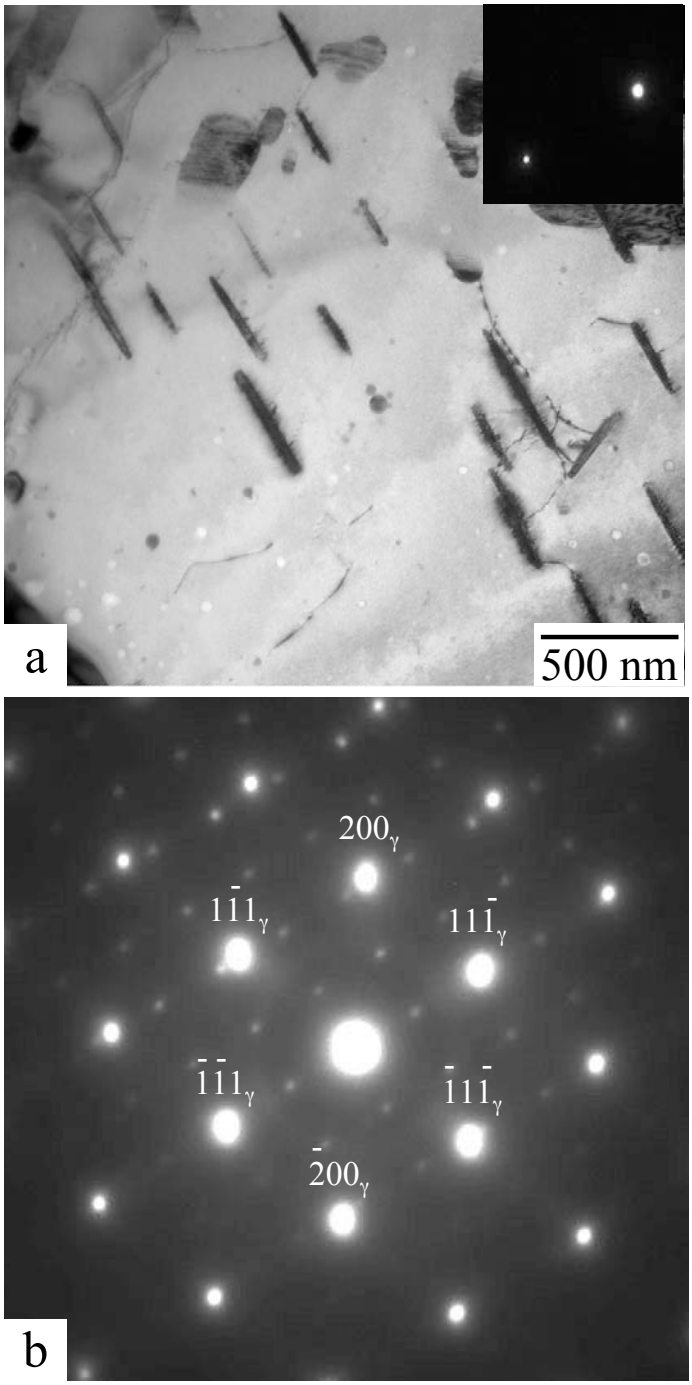

Fig. 4-14 TEM bright field image (**b**=11-1) and selected area diffraction pattern (**B**=011_{γ}) of the precipitations in grain interior of pre-aged B-doped steel (1073K/240h) creep tested at 973 K / 140 MPa (ε = 17%).

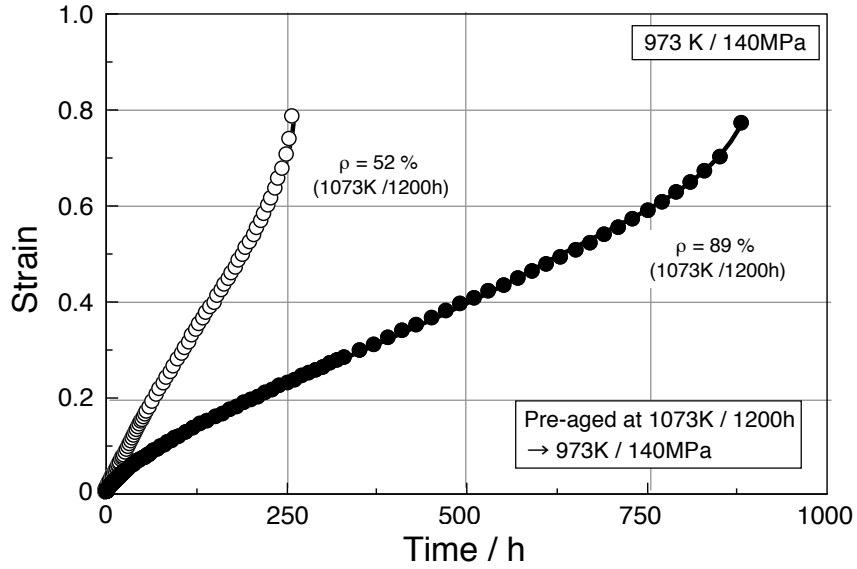

Fig. 4-15 Creep curves of 1073K / 12000h pre-aged B-doped and base steels tested at 973K / 140 MPa

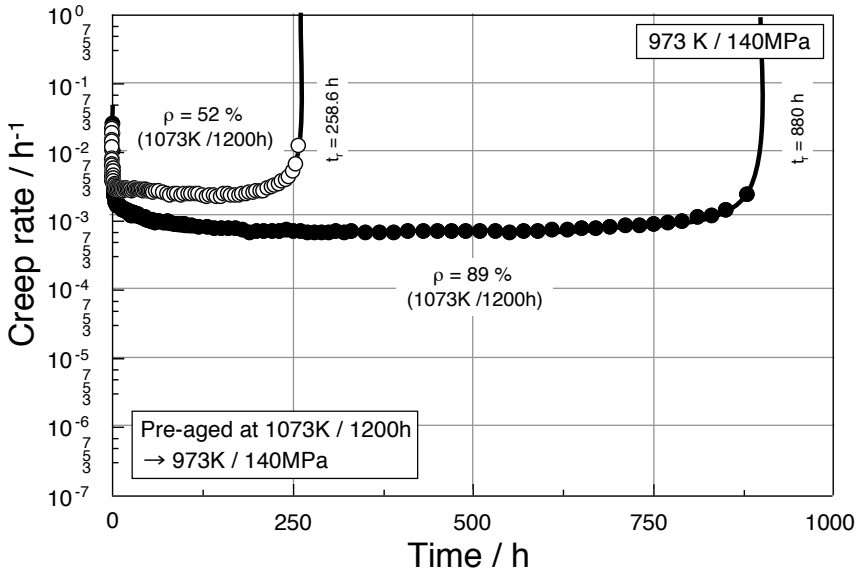

Fig. 4-16 Creep rate / time (linier scale) curves of 1073K / 1200h pre-aged base B-doped steels tested at 973K / 140 MPa.

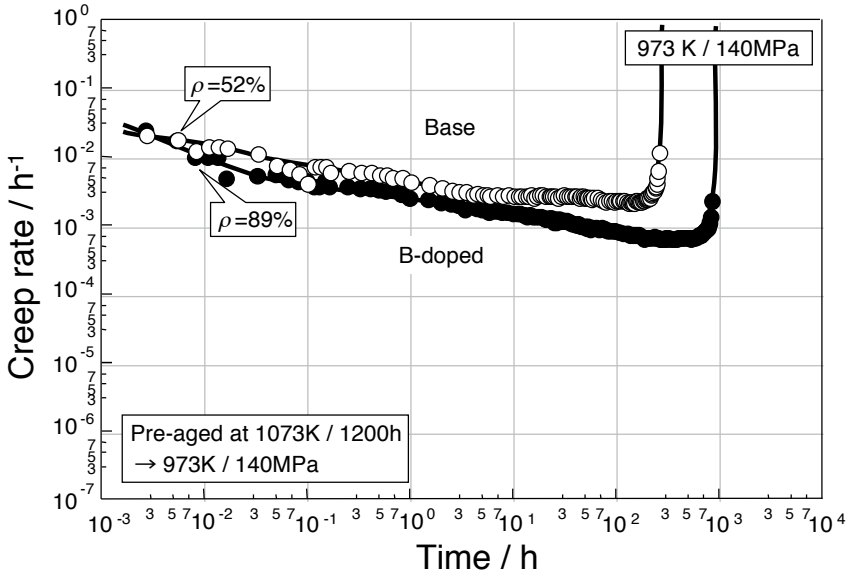

Fig. 4-17 Creep rate / time (logarithmic scale) curves of 1073K/1200h pre-aged base and B-doped steel tested at 973K / 140 MPa.

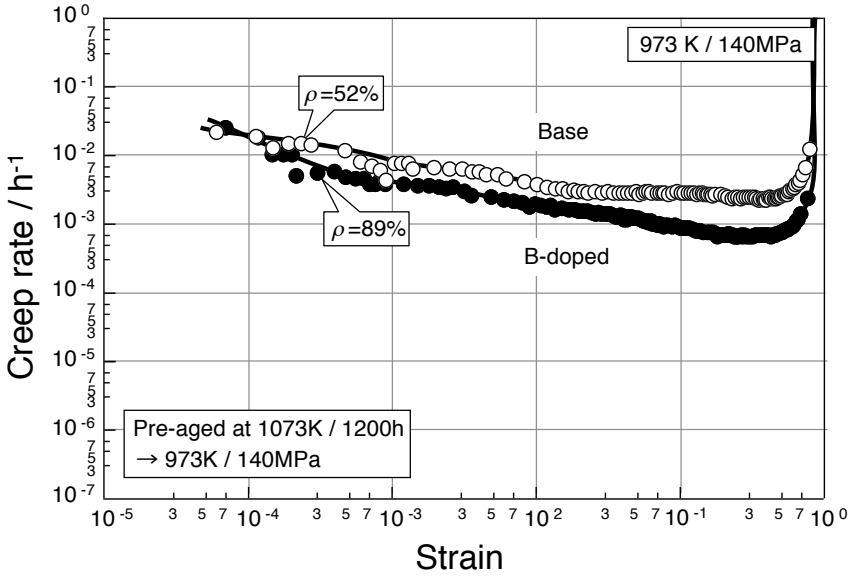

Fig. 4-18 Creep rate / strain curves of 1073K/1200h pre-aged base and B-doped steel tested at 973K / 140 MPa.

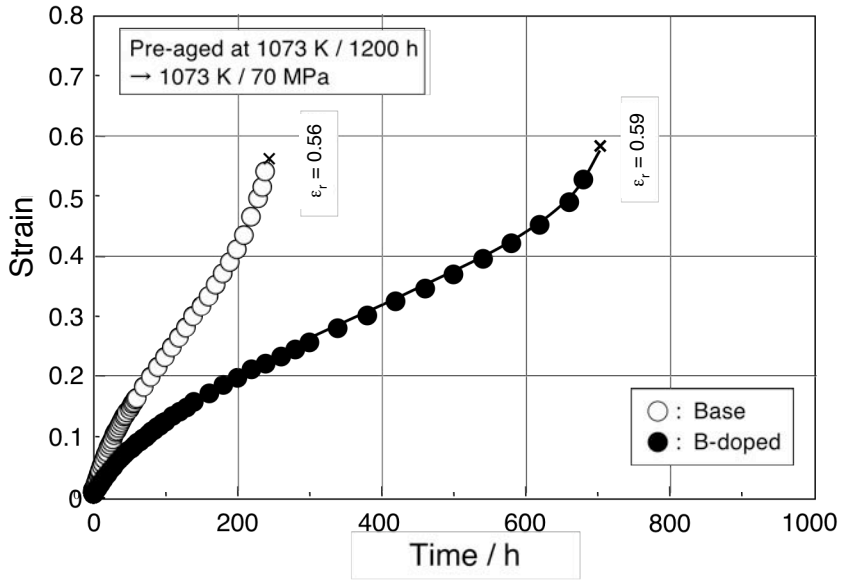

Fig. 4-19 Creep curves of 1073K / 1200h pre-aged B-doped and base steels tested at 1073K / 70 MPa

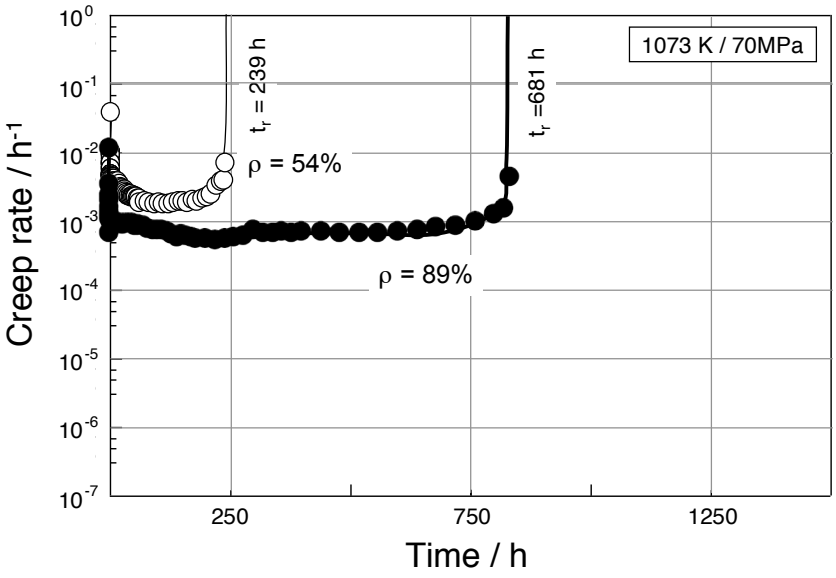

Fig. 4-20 Creep rate / time (linier scale) curves of 1073K / 1200h pre-aged base and B-doped steels tested at 1073K / 70 MPa.

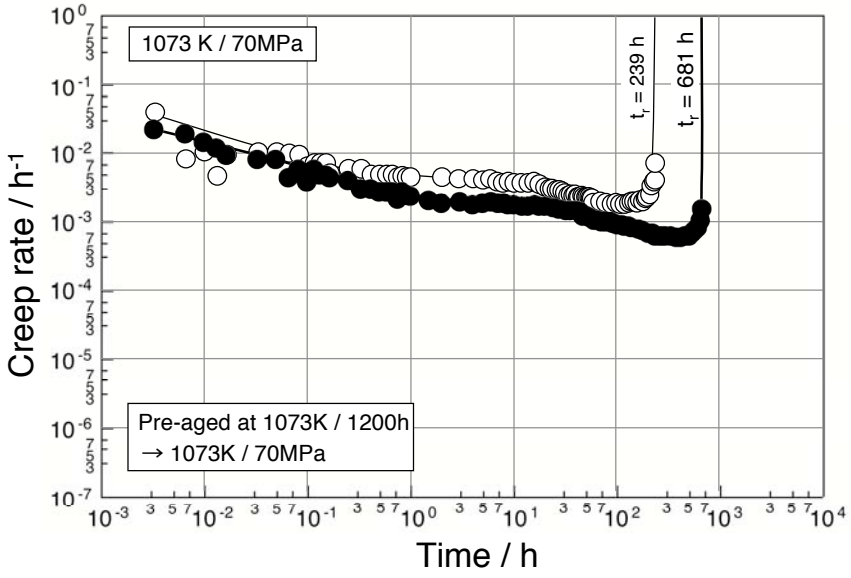

Fig. 4-21 Creep rate / time (logarithmic scale) curves of 1073K/1200h pre-aged base and B-doped steel tested at 1073K / 70 MPa.

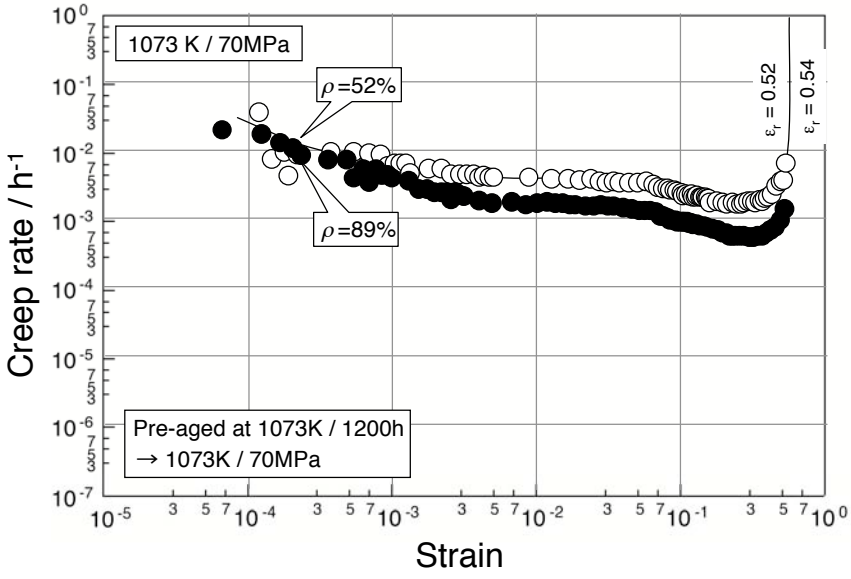

Fig. 4-22 Creep rate / strain curves of 1073K/1200h pre-aged base and B-doped steel tested at 1073K / 70Pa.

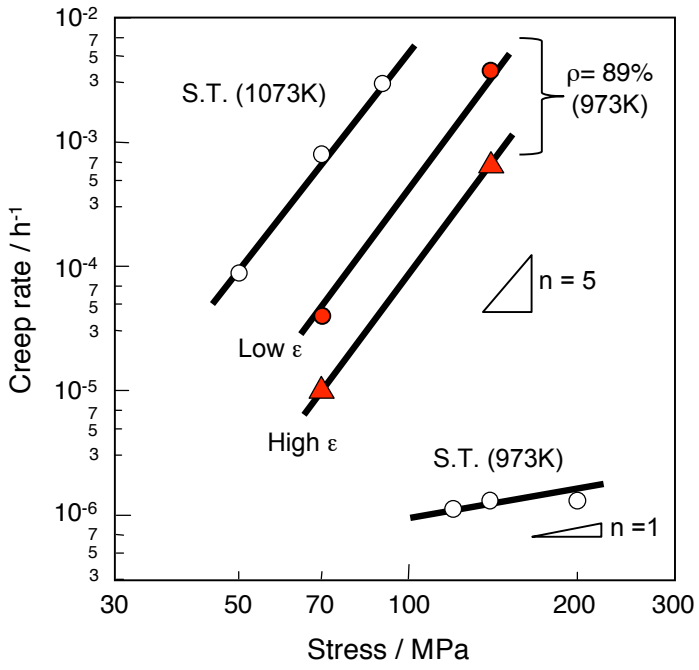

Fig. 4-23 Creep exponent of 1073K / 1200h pre-aged B-doped steel.

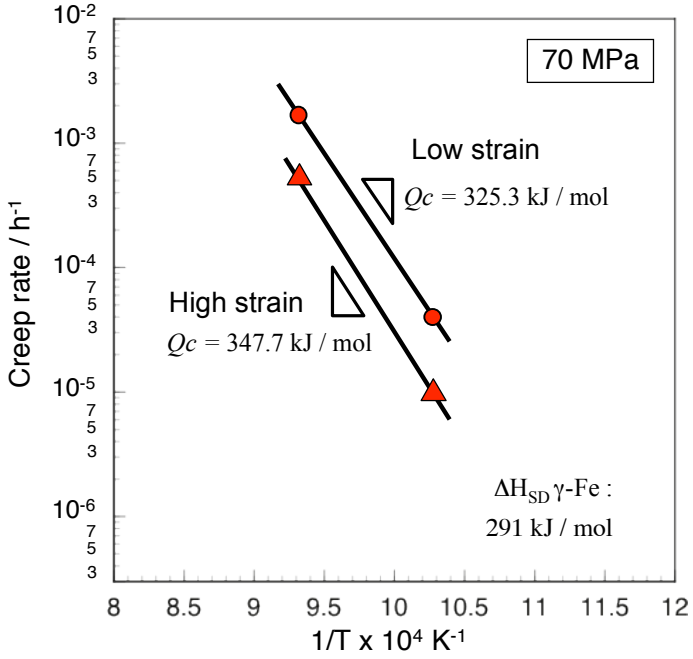

Fig. 4-24 Creep activation energy of 1073K / 1200h pre-aged B-doped steel at 70 MPa.

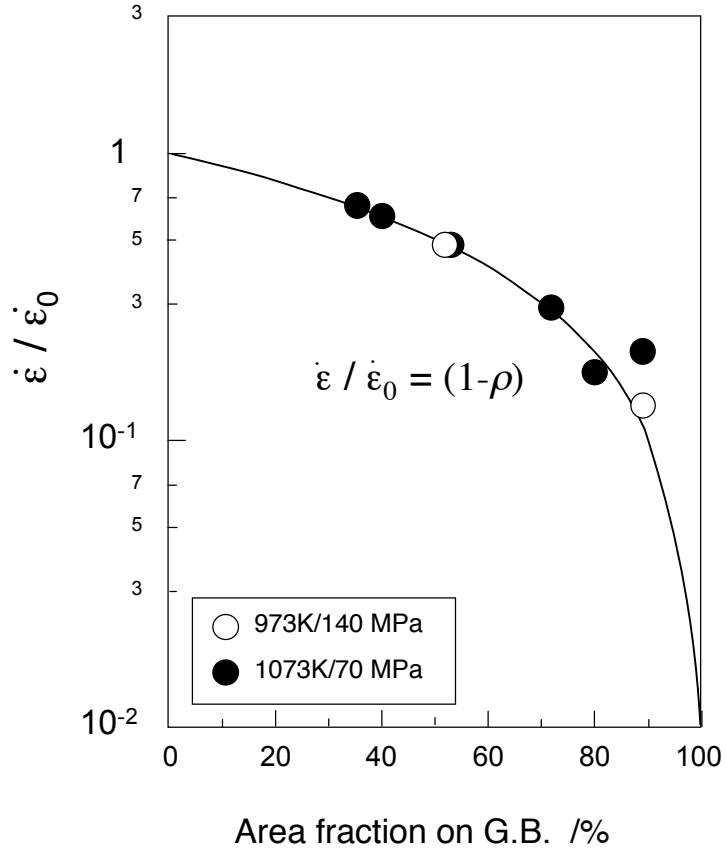

Fig. 4-25 Relationship between creep rate and area fraction of GB Laves phase in Fe-20Cr-30Ni-2Nb austenitic heat resistant steels.

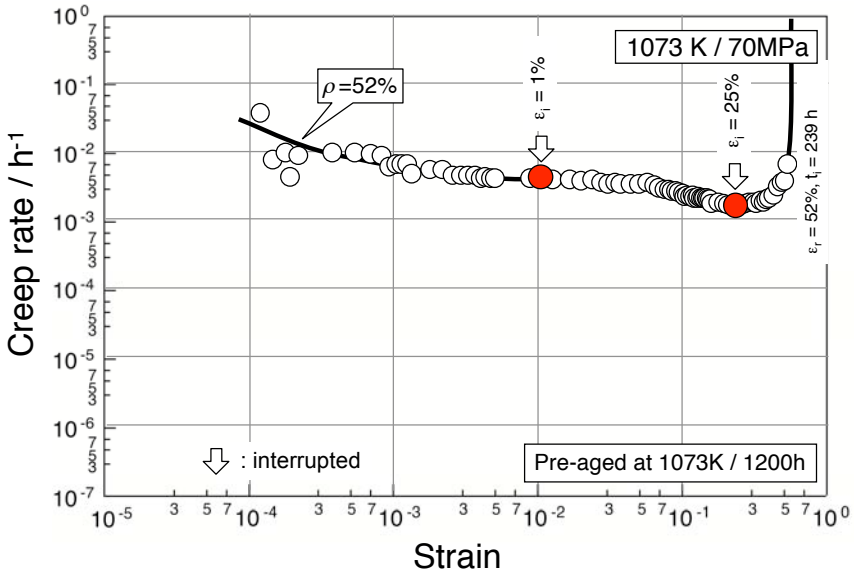

Fig. 4-26 Creep interrupt condition of 1073K/1200 h pre-aged base steel, tested at 1073K / 70 MPa.

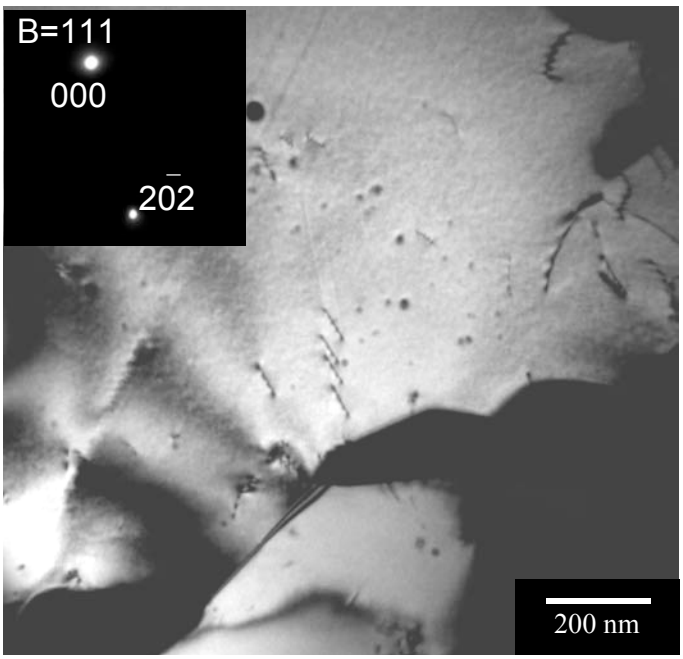

Fig. 4-27 TEM bright field image (**g** = 202_{γ}) of dislocations near grain boundary in the 1073K / 1200h pre-aged base steel creep tested at 1073K / 70 MPa (ε = 1%).

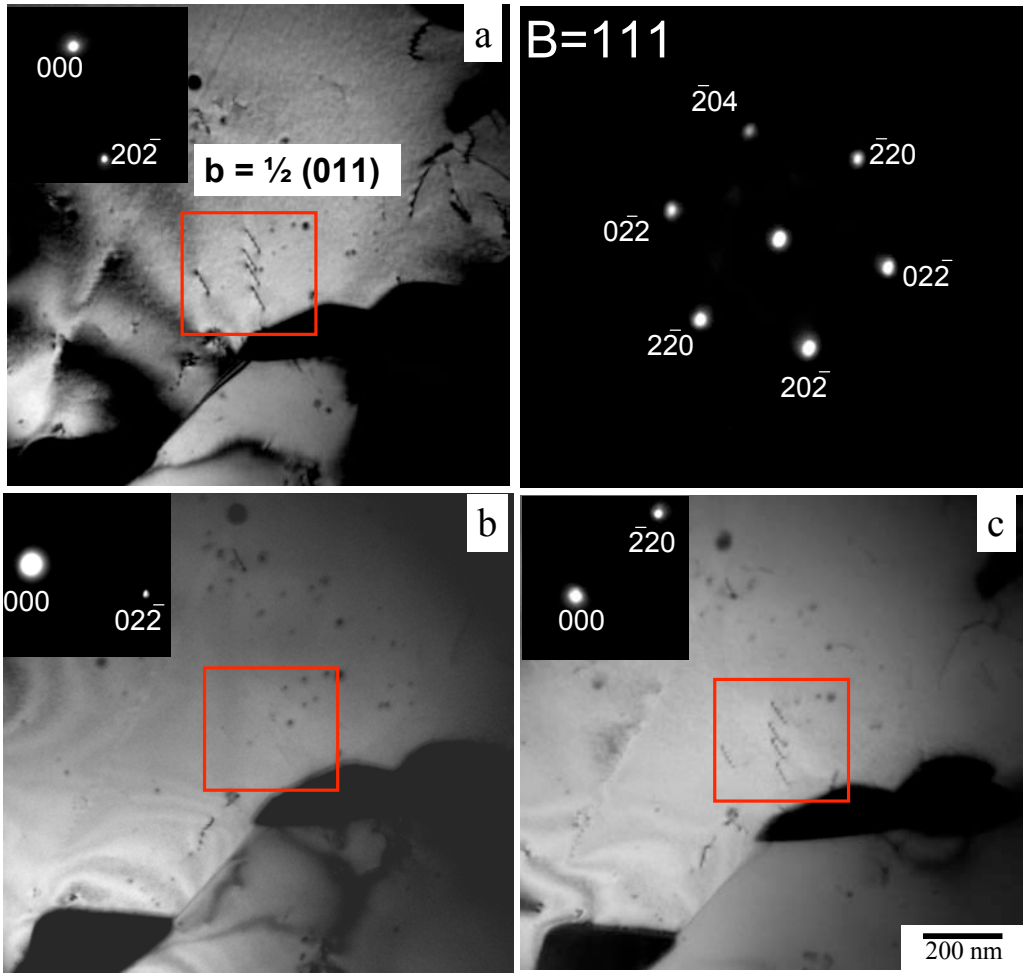

Fig. 4-28 Determination of burgers vector of dislocations near grain boundary in the 1073K / 1200h pre-aged base steel creep tested at 1073K / 70 MPa (ε = 1%): (a) **g** = 202 (b) **g** = 022 (c) **g** = 220

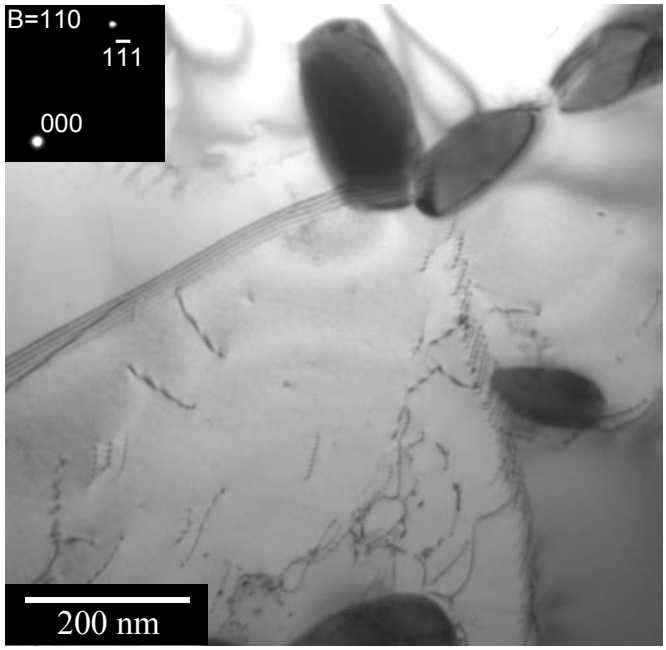

Fig. 4-29 TEM bright field image (**g** = 111_{γ}) of dislocations near grain boundary in the 1073K / 1200h pre-aged base steel creep tested at 1073K / 70 MPa (ε = 25%).

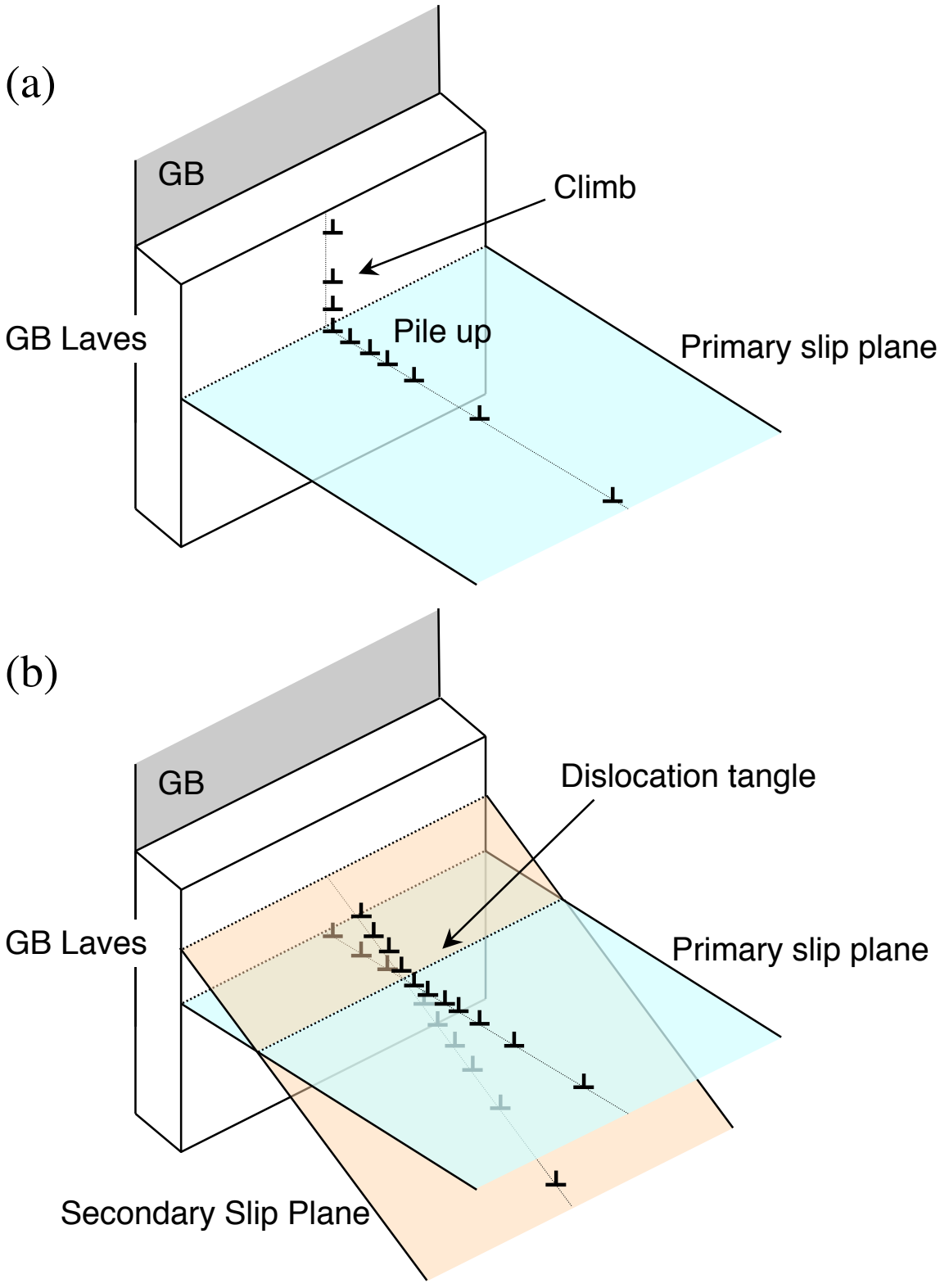

Fig. 4-30 Schematic illustration showing mechanism of creep strengthening by GB Laves : (a) low strain , (b) high strain.

Chapter 5

Role of Grain Boundary Laves Phase on Deformation Mechanism at Accelerating Stage

5.1 Introduction

In previous chapter, it has been revealed that the GB Laves phase increases the creep resistance through "grain boundary precipitation strengthening" mechanism, where it acts as a barrier for dislocation motion around grain boundary. This concept can explain well the second decrease of the creep rate of solution treated B-doped steel tested at 973K /140 and 120 MPa (**Fig. 3-11, 12**), i.e. due to the increasing precipitation of GB Laves phase. However, we still have not yet understood the reason for the creep acceleration after the second minimum. If the precipitation of GB Laves proceeds during creep, the creep rate should have continued to decrease in this stage, but hence it bounces back again and keeps increasing until ruptured. This might be related to the creep deformation mechanism in this steel, but it needs further investigation to reveal it.

We have tried to examine the creep behavior at the high strain region, i.e. the second acceleration stage of the steels. We would like to know whether the GBPS mechanism could be also extended into this stage. For this objective, microstructure change during the second acceleration stage would be the key factor for the investigation. Normally it can be achieved by conducting creep-interrupted tests at this stage. Unfortunately, it would take very long time to reach the second acceleration stage in the solution treated B-doped steel, i.e. more than 4000 h, and thus the creep interrupted test is not the effective method for the investigation. Therefore, we have proposed another approach to investigate the microstructures at this stage, by using single ruptured sample that have been previously tested. On these samples, the cross section diameter along the gauge length is not the same, some area has smaller diameter than the others. It indicates that the deformation is not homogenously distributed across the gauge length. The area with smaller diameter experiences more deformation or higher strain than that of the larger ones. We have assumed that the microstructures at this certain macroscopic strain condition represent the actual microstructures at the same strain during creep. Therefore, the microstructures at the acceleration stages can be observed from the specific location on the gauge length of the ruptured specimens, having the same strain condition.

In this chapter, we first examined the microscopic strain profile across the gauge length of the ruptured specimens. Then based on the microstructure at certain microscopic strain of these specimens, the change in microstructure during acceleration stage has been investigated. From these results, the controlling mechanism for creep deformation in our model steel has been proposed.

5.2 Experimental Procedure

The flowchart of the experimental procedures used in this study is shown in **Fig. 5-1**. The steels used in this study are B-doped and base steels, which have the same compositions as described in Chapter 2. All steels were prepared by the same processes described in chapter 2, followed by solution treatment to obtain the grain size of 150 μm. Then, the some of the steels were aged at 1073K for up to 1200 h, with area fraction (ρ) of

89%, as shown in **Fig. 2-4**.

For the creep test, the all rods were cut into full size creep specimens with the same dimensions specified in **Fig. 3-2**. Tensile creep tests were conduced at 973K at constant stresses of 140 and 120 MPa. The creep tests were also done at 1073 K at constant stress of 70 MPa.

The microstructures were observed by using FE-SEM, with the same specification described in previous chapters. Local microstructures around grain boundary were analyzed by using Electro Back-Scattering Diffraction (EBSD) equipped with Orientation Imaging Analysis (OIM) software. The samples for EBSD observations were prepared by chemical-mechanically polishing by using colloidal silica with size of 0.05 μm. EBSD observations were conducted with step size up to 0.08 μm, which is applied on the surface normal to the stress axis of the creep specimen (TD) direction.

The approach to observe the microstructure on the creep accelerating stage is shown in **Fig. 5-2**. First, we selected the positions on the creep rate–time curves that we intended to observe, for example at t = 7000 h. Then, from the creep rate–strain curve of the steel, we found the corresponding creep strain of this target position, in this example is at 4% of strain. On the creep-ruptured specimen, we measured the macroscopic strain along the gauge length and tried to find out the area, which has the same strain with the target creep strain that we would like to observe. Finally the microstructure at this specific area was examined. The macroscopic strain along the gauge length was calculated by using equation 1, where A_0 and A are the cross section area before and after creep, respectively.

$$\varepsilon = \frac{A_o}{A} - 1 \qquad (1)$$

5.3 Results

5.3.1 Change in area fraction of GB Laves phase with strain

We have tried to observe the microstructures on the creep acceleration stage of solution treated B-doped steel tested at 973K / 140 MPa at three different creep time, i.e. at 3800 h, 7400 h and 8950 h, as shown in the creep rate-time curve of the steel in **Fig. 5-3**. From the creep rate-time curve of the steel, the corresponding creep strains at these specified times are 1.3 %, 4 % and 9.5 %, respectively (**Fig. 5-4**). **Figure 5-5** shows the macroscopic view of the steel after the creep test. The macroscopic strain varies along the gauge length from 36 % to 5 %, although the average strain of the steel is only 11.5 %. From this macroscopic strain measurement, the area with strain of 4 % and 9.5 % can be found at 15 mm and 7 mm, respectively, from the ruptured area. Unfortunately, the strain of 1.3 % cannot be found on this specimen, but since it is very small and can be negligible, we assumed that the microstructure would be the same as that in the unstrained region, or in other words, at screw portion. **Figure 5-6** shows the microstructures on the area with

macroscopic strain of 0 %, 4 % and 9.5 %. All of the microstructures consist of Laves phase at grain boundaries and Ni_3Nb-δ precipitates within grain interior. However, the area fraction of GB Laves phase seems to decrease with increasing the macroscopic strain. The measured ρ in the unstrained region is 81 %, but on the area with 4 % and 9.5 % macroscopic strain, it becomes 75 % and 66 %, respectively.

To clarify these findings, we have conducted the same observation on the solution treated B-doped steel tested at 973 K / 120 MPa. **Figure 5-7** shows the outlook of the ruptured specimen of the steel. The macroscopic strain along the gauge portion varies from 36 % near the ruptured portion to about 5 % near the annular ridges, while the average creep strain is 9.5 %. **Figure 5-8** shows the microstructures of the different portion of the specimen with the strain of 5.7 % (a) and 36% (b) as indicated by the arrows in **Fig. 5-7**. Both show similar precipitation of Ni_3Nb-δ within grain but the ρ at 5.7 % strain is much higher than that at 36 % strain, i.e. 75 % and 56 %, respectively. This result is similar to that found on the steel tested at 973 K / 140 MPa, i.e. the ρ decreases with increasing strain.

We have further investigated the ρ on different macroscopic strained regions of both samples to have better observation on this tendency. **Figure 5-9** shows the ρ as function of macroscopic strain in rupture specimens of solution treated B-doped steel, tested at 973 K / 140 and 120 MPa. At 140 MPa, the ρ decreases continuously with increasing the macroscopic strain from 81 % at unstrained region to 55 % at strain of 36 %. At 120 MPa, the ρ slightly increases from 70 % at unstrained region to 74 % at strain of 5.7 %. However, with further increase in strain, the ρ decreases continuously to 58 % at strain of 15% and then it becomes constant. These results confirm the previous findings that the strain has strong effect on the area fraction of GB Laves phase during creep.

5.3.2 Estimation of creep rate based on macroscopic strain

Based on the previous findings, it can be assumed that the increase of the creep rate after the second minimum might be due the decrease of the area fraction of GB Laves phase during creep deformation, which would be in good agreement with the GBPS equation. **Figure 5-10** shows the estimated creep rate by GBPS equation using ρ obtained from the macrostructure strain observation in solution treated B-doped steel tested at 973 K / 140 MPa, in addition to the actual creep rate and those predicted from simple aged microstructures as comparison. The calculation of the creep rate using ρ from the simple aged microstructures will give the results that have opposite trend to the actual creep rate, since the ρ is not affected by strain. On the other hand, by using the ρ from macroscopic strain observation, the calculated creep rate shows the same trend to that of the actual creep rate, i.e. it increases with increasing creep strain. However, the values are 1 order magnitude lower than the actual measurements. In implies that there is another factor, other than strain, that contributes to the acceleration of the creep rate.

In order to find out the cause of the big difference between the calculated creep rate by GBPS and the actual measurements, we have re-examined the microstructures of the steel. **Figure 5-11** shows the microstructure of the solution treated B-doped steel creep tested at 973 K / 140 MPa at macroscopic strain of 4 %. It can be observed that precipitation of Laves phase at grain boundary is not homogenous. Although the average ρ of this microstructure is 75 %, some of the local area has almost 0 %, while some others can reach almost 100%. This variation of ρ on local microstructure could be the key factor that causes the difference between the calculated creep rate and the actual measurement. For instance, the local area that has low ρ will exhibit much higher creep rate than that with higher ρ, and based on GBPS equation the difference could be 1 order of magnitude, which is the same difference that has been found in our calculation results. If the creep deformation is controlled by the fastest process, the creep rate at local area with the lowest ρ will determine the overall creep rate of the steel.

Figure 5-12 shows the Inverse Pole Figure (IPF) map and corresponding Grain Reference Orientation Deviation (GROD) map of EBSD-OIM analysis for the solution treated B-doped steel tested at 973 K / 140 MPa, at macroscopic strain of 4%. The IPF map, which indicates the relative orientation of each individual grain, shows that the orientation of the grain is randomly distributed, without any preferred orientation. However, the GROD map, which calculates the misorientation between each point of the grain and the average orientation of the grain, shows that some area near the grain boundary has higher misorientation compared to that of grain interior. If we assume that the misorientation is caused by strain, the result implies that the creep deformation is concentrated at some local area near the grain boundary. This further supports our previous assumption that the overall creep rate of the steel might be determined by the creep rate at local area around grain boundary, which has the lowest ρ. However, it needs further examination to confirm it.

5.3.3 Change in local microstructure during creep

The results obtained so far have indicated that the local microstructure might be the key to understand the deformation mechanism in the steels. Therefore, we have tried to examine in more detail the change in local microstructures around grain boundary during creep. To simplify the analysis, we have done the observation using 1073K / 1200 h pre-aged steels, which do not have any precipitation of Ni_3Nb phases. **Figure 5-13** shows the positions on the creep rate-time curves of 1073K / 1200 h pre-aged B-doped steel (ρ = 89%), tested at 973K / 140 MPa, which we would like to examine, i.e. at 200 h, 590 h, and 830 h. Note that the positions at 200 h and 590 h are on the beginning and end of the steady state creep stage, respectively, while 830 h is at the acceleration stage. The corresponding positions on the creep rate-strain curve are shown in **Figure 5-14**. The creep strains at 200 h, 590 h and 830 h are 19 %, 46 % and 68 %, respectively. We have done the

same method that we used previously to observe the microstructures, that is by using the single ruptured specimen having the same macroscopic strain with the creep strain of the positions that we would like to observe.

Figure 5-15 shows the outlook of the ruptured specimen of the steel after the creep test. The macroscopic strain along the gauge portion varies from 250 % near the ruptured portion to 19% near the annular ridge, with the average strain of 77 %. The positions of the microstructures that we would like to observe are located more than 10 mm away from the ruptured surface, as shown in the figure. **Figure 5-16** shows the microstructures along the gauge portion of the specimens with macroscopic strain of 19 %, 46 % and 68 %. Only Laves phase was observed on the grain boundaries and grain interior of all microstructures. However, similar to that observed on that of solution treated steel tested at 973 K, the ρ seems to decrease with increasing strain. From 19 % to 46 % of strain, which are on the steady state creep stage, there was not so much reduction in ρ, i.e. from 92 % to 88 % of ρ. However, at strain of 68 %, which is on the acceleration stage, the ρ significantly drops to 76 %. **Figure 5-17** shows the change in ρ and grain interior hardness as function of strain of the steel. It has been clear that the ρ decreases with macroscopic strain, which shows the same phenomena to that found on the solution treated steel tested at 973 K. On the other hand, the grain interior hardness is constant with strain at about 1.8 GPa, which could imply that there was no significant microstructure change or deformation process occurred at grain interior during creep.

Figure 5-18 shows the GROD maps and line misorientation profiles from grain interior to grain boundary of the microstructures on each observed macroscopic strain. Line A shows the misorientation profiles around uncovered grain boundary, while line B is around the GB Laves phase. At 19% of strain, there is local area near the uncovered grain boundary with high misorientation of 5° and advancing of about 2.5 μm towards the grain interior. On the other hand, there is almost no orientation difference on the area near the GB Laves. At 46 % of strain, we have found similar local high-misorientation area near the uncovered grain boundary but with much higher misorientation, which could reach up to 20°. The width of this local area is about 2.5 μm from the grain boundary, which is almost the same to that at 19 % of strain, while the misorientation near the GB Laves phase only increases slightly to about 5°. At 68% of strain, the local high-misorientation area can also be observed but greater in number compared to that at 46 % and 19 % of strain. The misorientation of these areas is about 20° with the width of about 2.5 μm, which is almost the same to that at 46% strain. However the misorientation on the surrounding of these local high-misorientation areas is higher than that at the lower strain. The misorientation near the GB Laves phase is only about 7° but more spreaded towards grain interior compared to that at 46% of strain. **Figure 5-19** shows the summary of relative misorientation between the area near the uncovered grain boundary and GB Laves phase, in addition to the length of the high-misorientation area near the uncovered grain boundary at strain of 1 to 68 %. The data at lower strain was obtained from the observation on the

steel with ρ of 40 % and creep tested at 973 K / 140 MPa. The difference in misorientation between area near the grain boundary and GB Laves increases with strain up to 12° at 46 % of strain and becomes lower with further increase in strain. The decrease in misorientation after 46 % of strain is due to the increase of misorientation at grain interior or GB Laves phase with increasing strain, while the maximum misorientation of local area near the grain boundary is limited to 20°, which is around the minimum misorientation of high-angle grain boundary [1]. It seems that after reaching misorientation of 20°, the local high-misorientation area near the grain boundary becomes a new subgrain. On the other hand, the width of the local high-misorientation area near the grain boundary increases significantly with strain to about 2 μm and becomes constant beyond 20 % of strain.

5.4 Discussions

5.4.1 Model to estimate local strain distribution along grain boundary

Based on the data obtained by line analysis method, we have tried to convert this misorientation into strain difference between area near grain boundary and grain interior. We have proposed a preliminary model to estimate the local strain [2-4], which is illustrated in **Fig. 5-20**. There are 3 assumptions used in this model, they are:

1. Two deformation zone

The deformation zone on each grain is assumed to be divided into two distinct regions, i.e. grain interior and grain boundary zone. The deformation within each zone is also assumed to be distributed homogeneously. Based on these assumptions, we can calculate the total strain within one grain by using rule of mixture, as follow:

$$\varepsilon = \varepsilon_{gb} \cdot V_{gb} + \varepsilon_{gi} \cdot V_{gi} \qquad (2)$$

where ε, ε_{gb}, ε_{gi}, V_{gb} and V_{gi} are total strain, strain near grain boundary, strain in grain interior, volume fraction of near grain boundary area and volume fraction of grain interior, respectively.

2. Misorientation angle is due to pure shear strain

It is assumed that the misorientation is caused by pure shear strain, thus the it can be related to the strain by using the following equation:

$$\gamma = \tan\Delta\theta = \varepsilon_{gb} - \varepsilon_{gi} \qquad (3)$$

where γ and $\Delta\theta$ are shear strain and misorientation angle respectively.

3. Spherical grain shape

In this model, the grain is assumed to be spherical, thus the volume fraction of grain boundary area and grain interior in equation (2) can be calculated by using the equation:

$$V_{gb} = \frac{4\pi\left(\frac{d}{2}\right)^2 \cdot \delta}{\left\{\frac{4}{3}\pi\left(\frac{d}{2}\right)^3\right\}} \cdot (1-\rho) \quad (4)$$

$$V_{gi} + V_{gb} = 1 \quad (5)$$

where d, δ and ρ are grain size, width of local deformation measured from grain boundary and area fraction of grain boundary Laves phase respectively.

Figure 5-21 shows the calculation results of local strain near the grain boundary and GB Laves of the steel with ρ of 89%, tested at 973 K / 140 MPa, by using the proposed model and the data from line misorientation analysis in **Fig. 5-18**. Based on the calculations, the local strain on grain boundary is higher than that near the GB Laves phase and the difference becomes much larger with increasing strain. Calculation made on the steel with ρ of 40%, tested at 973 K / 140 MPa and interrupted at 17% creep strain also gives the same result that the strain at grain boundary area is much higher compared to the strain in grain interior ($\varepsilon_{gb} / \varepsilon_{gi} \approx 1.7$) [3]. Since the creep rate is a function of strain ($\dot{\varepsilon} = \varepsilon / dt$), these results imply that during creep the local deformation area near the uncovered grain boundary will experience much higher creep rate than that of grain interior. It agrees very well with the GBPS equation, since the uncovered grain boundary will have $\rho = 0$ and thus experience creep rate on order of magnitudes higher than the bulk. If the overall creep deformation is determined by the fastest rate then it can explain the big difference of the creep rate between that calculated from the GBPS, using the average ρ, and the actual results. In other words, the GBPS can also be applied on the acceleration stage by considering the local microstructures.

5.4.2 Creep deformation mechanism at the accelerating stage

Based on these results we have proposed the deformation mechanism at the accelerating stage as shown in **Fig. 5-22**. It has been found that the creep mechanism in the model steel is controlled by dislocation movements. It is with regard to concept that the creep deformation was proposed. At high temperature, the grain boundary becomes the weakening factor for creep since it provides vacancies and site for dislocation annihilation. Thus, the dislocations can easily move around and cause the creep deformation to be concentrated on this area. This is why we could find many local deformation areas around the grain boundary uncovered by the Laves phase. The local deformation area will exhibit much higher creep rate compared to the bulk and, as have been mentioned previously, it will determine the overall creep rate. All in all, we have proposed that the creep deformation in the model steel is due to the creation and evolution of the local deformation

area around the grain boundary.

Figure 5-23 shows the microstructure of the ruptured specimen of 1073 K / 240 h pre-aged steel (ρ = 40%) creep tested at 1073 K / 70 MPa. From the microstructure, it can be observed that the failure of the steel is due the grain boundary fracture. If it is observed more closely, many of the fracture occurs at the uncovered grain boundary, which indicates that the crack initiated on this site during creep. This result agrees very well with our proposed deformation mechanism as the uncovered grain boundary area will experience much higher creep rate and thus firstly reach the failure. **Figure 5-24** shows the change in rupture time and strain as function of ρ on the steels tested at 1073 K. The creep rupture time increases slightly by increasing the ρ from 40 to 80%. However, when more than 80% of grain boundary area is covered by the Laves phase, the creep rupture time improves significantly. These results also strengthen our proposed mechanism. By increasing the ρ more than 80%, almost all the grain boundary area will be protected by the Laves phase, which decreases the possibility for the formation of local deformation area. Since the local deformation around the grain boundary is suppressed, the accelerated region will be extended during creep resulting in much longer creep rupture life. On the other hand, the rupture strain is not affected by ρ. Even at ρ more than 80%, the rupture strain can still reach more than 60%. The constant rupture strain with ρ strongly indicates that the fracture was not initiated at the GB Laves phase, which most people believed to be the embritllement effect of GB Laves phase. Instead, the fracture was initiated at uncovered grain boundary area as suggested by our proposed deformation mechanism and the results of microstructure observation in **Fig. 5-23**.

5.5 Summary

The deformation mechanism at the creep acceleration stage has been investigated. Followings are the conclusions drawn from this chapter:

1) Local deformation area with high misorientation occurs on grain boundary area uncovered by Laves phase
2) The local deformation area exhibits much higher creep rate than other sites in the microstructures and thus become the controlling rate of overall creep rate.
3) The rupture strength significantly increases by protecting more than 80% of grain boundary area with Laves phase.
4) The GBPS mechanism can be extended into acceleration stage by considering the local microstructure change.

References

[1] R. W. Hertzberg: Deformation and Fracture Mechanics of Engineering Materials, John Wiley & Sons, (1976).

[2] K. Kurata: Master Thesis, Tokyo Institute of Technology (2009).

[3] I. Tarigan: Master Thesis, Tokyo Institute of Technology (2010)

[4] I. Tarigan, N. Takata, M. Takeyama: Report of JSPS 123rd Committee on Heat-Resisting Materials and Alloys, **52** (2011), p. 63.

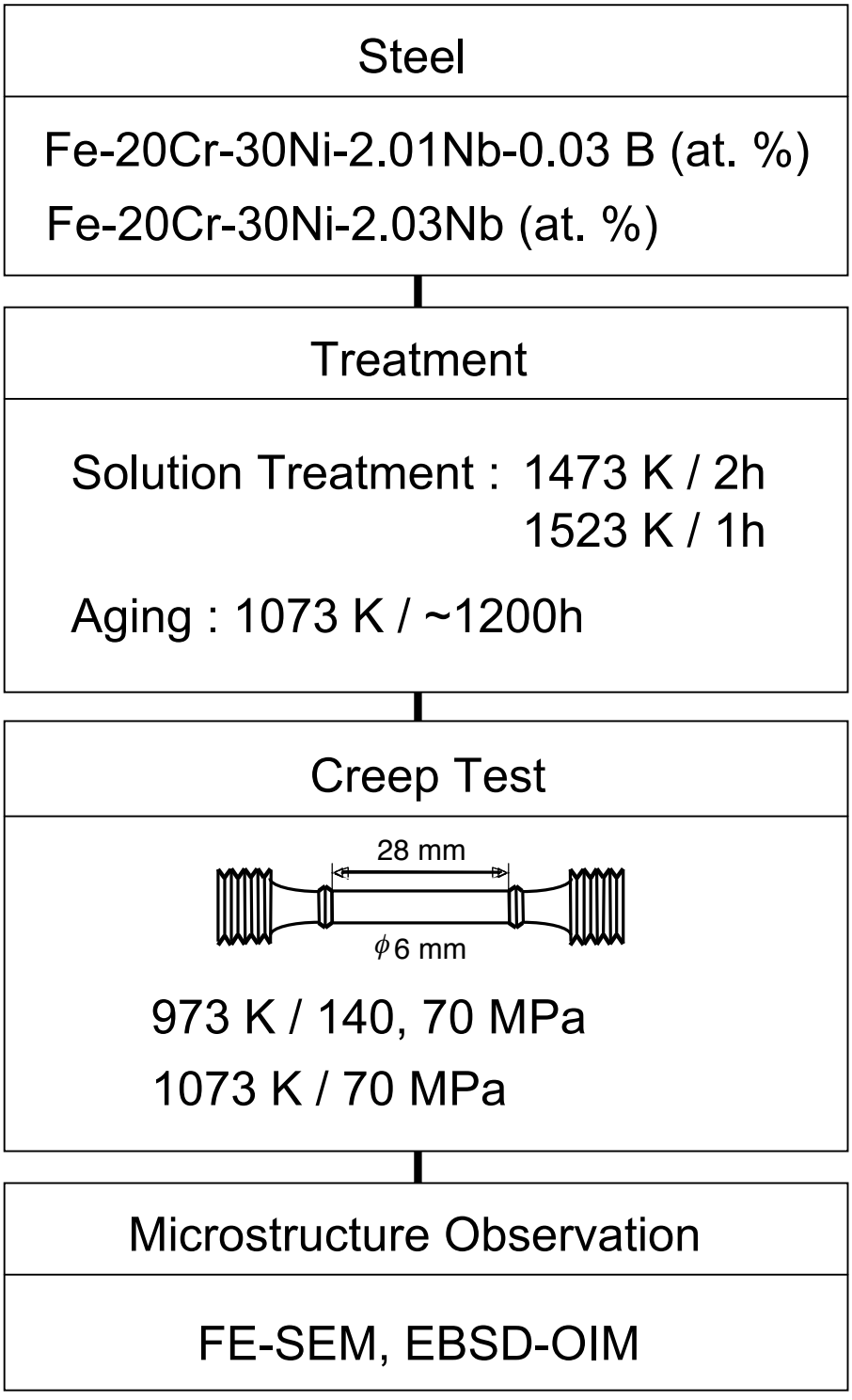

Fig. 5-1 Flow chart of the experimental procedures in the chapter 4.

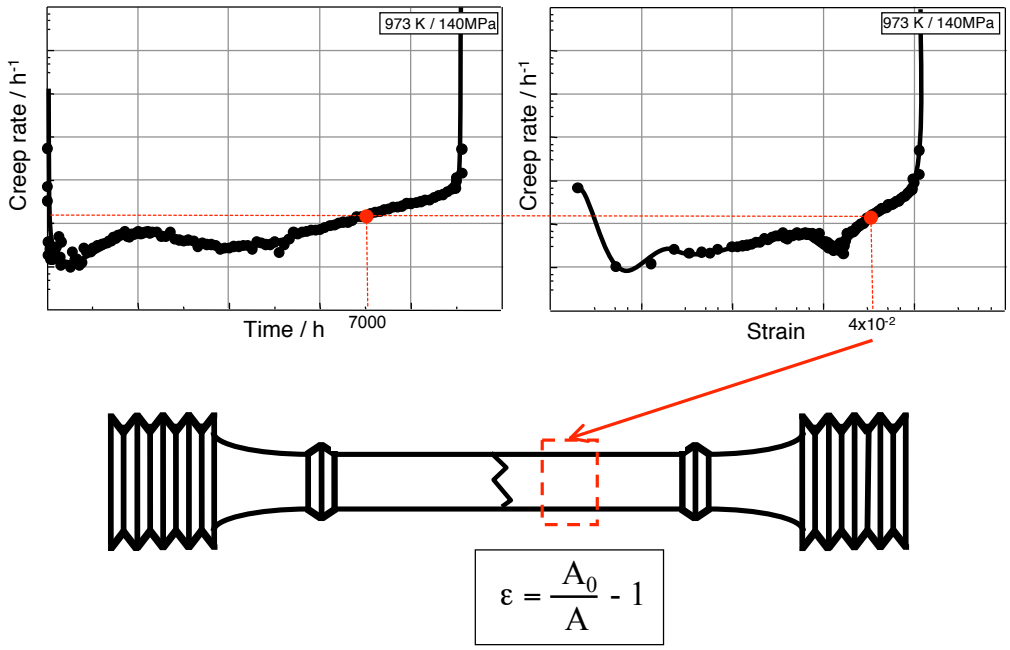

Fig. 5-2 Schematic illustration showing the method to observe microstructure at the accelerating stage based on local strain of the ruptured specimens

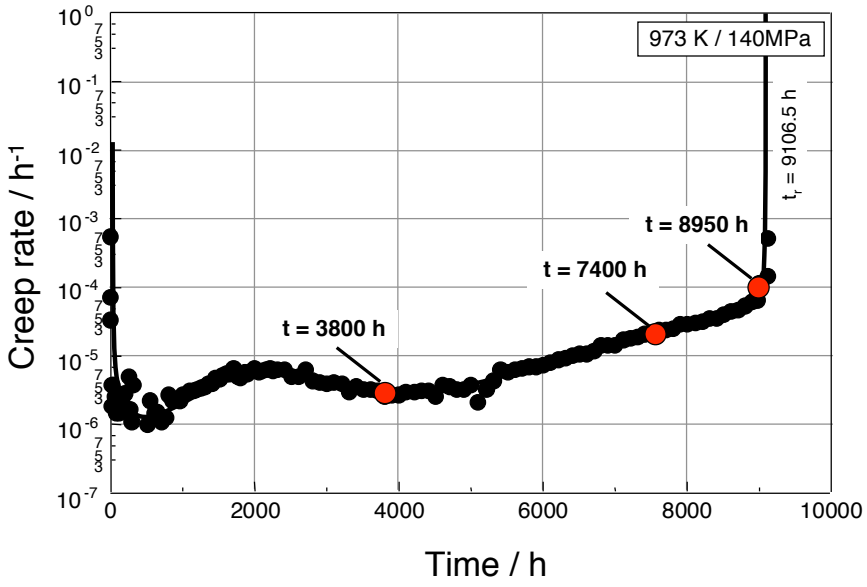

Fig.5-3 Creep rate time curve of as solution treated B-doped steel tested at 973K / 140 MPa.

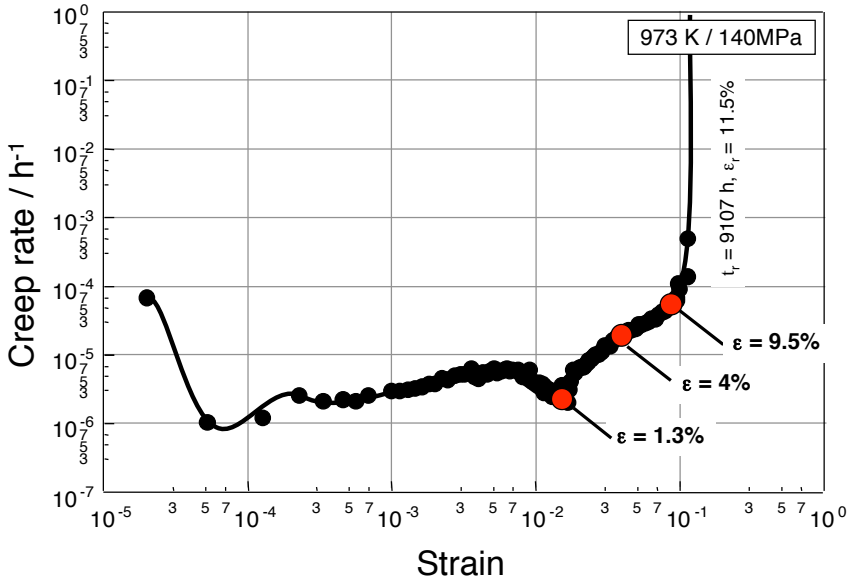

Fig. 5-4 Creep rate strain curve of as solution treated B-doped steel tested at 973K / 140 MPa.

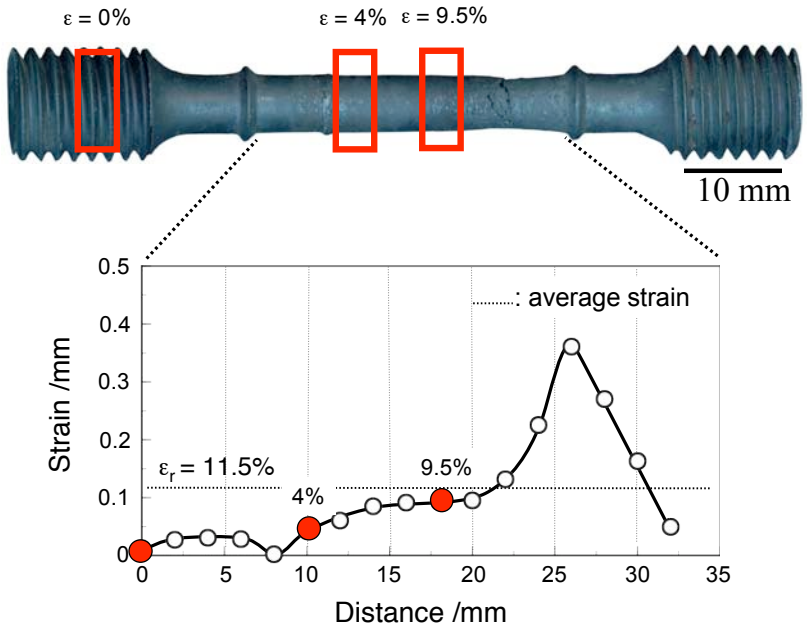

Fig. 5-5 Outlook of fractured B-doped steel at 973K/140 MPa and variation in macroscopic strain along the gauge length

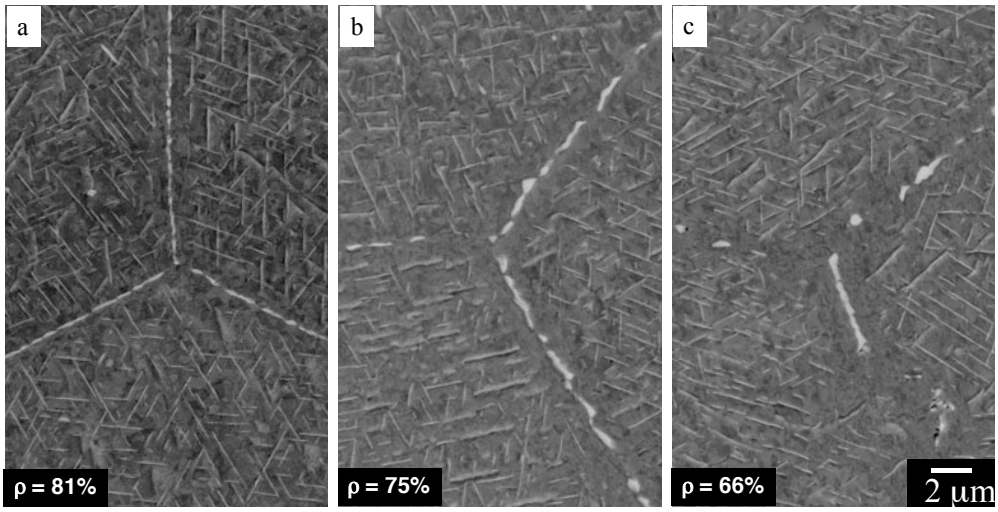

Fig. 5-6 Local microstructures of solution treated B-doped steel after creep tested at 973K / 140 MPa: (a) ε = 0%, (b) ε = 4%, (c) ε = 9.5%

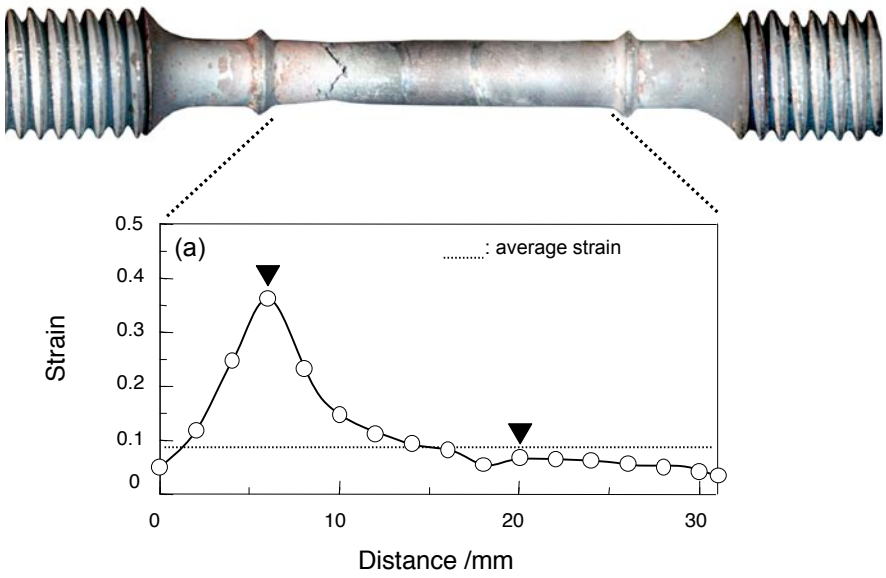

Fig. 5-7 Outlook of fractured B-doped steel at 973K/120 MPa and variation in macroscopic strain along the gauge length

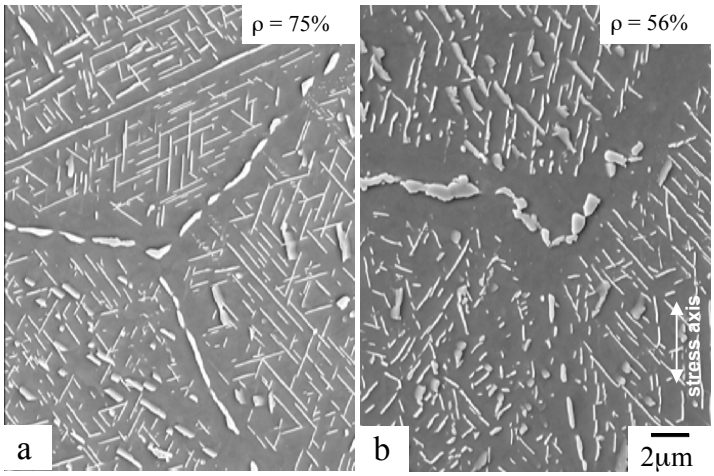

Fig. 5-8 Local microstructures of solution treated B-doped steel after creep tested at 973K / 120 MPa: (a) ε = 5.7%, (b) ε = 36%

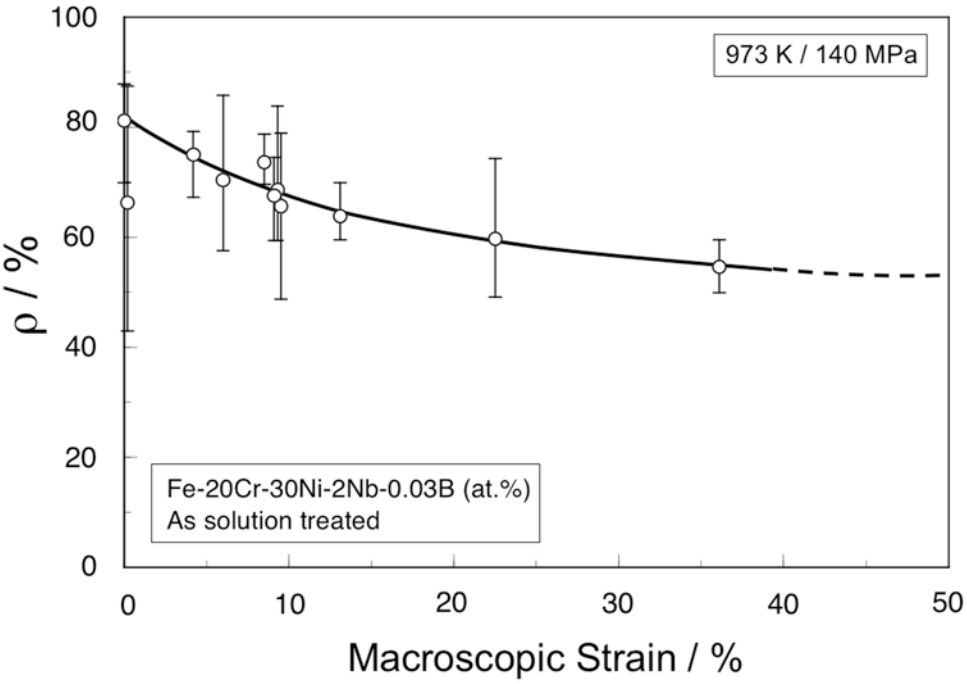

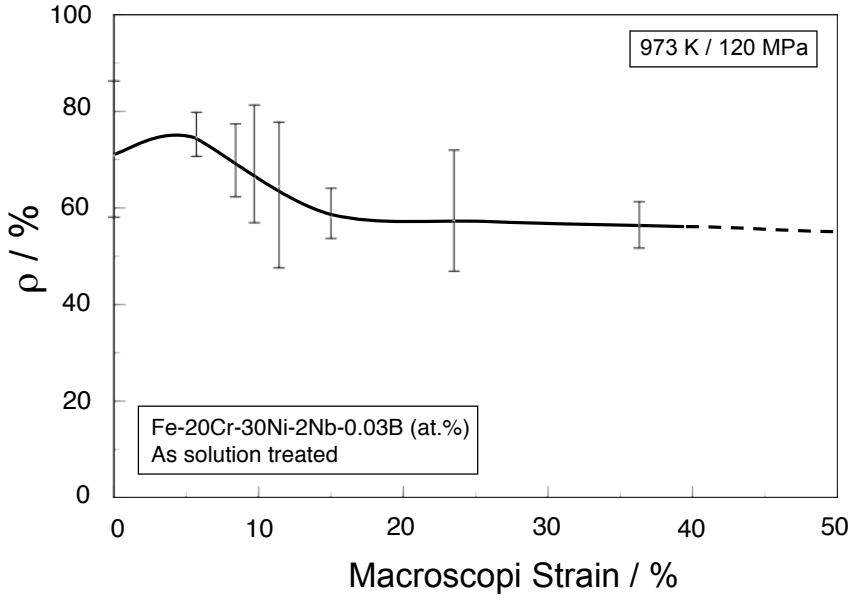

Fig. 5-9 Change in area fraction of GB Laves phase with macroscopic strain in B-doped steel creep tested at 973K /140,120 MPa

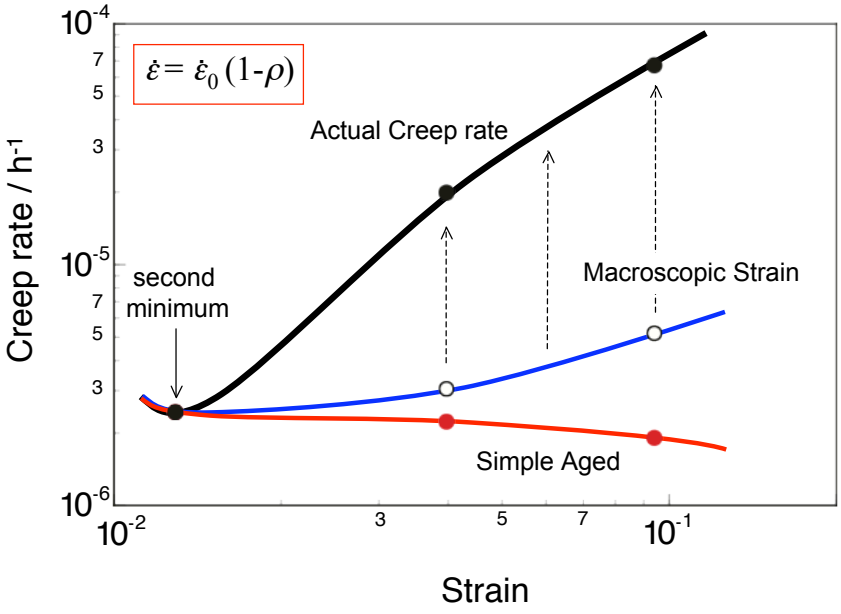

Fig. 5-10 Estimated creep rate by GBPS equation using area fraction obtained from ruptured specimen of B-doped steel tested at 973K/140 MPa.

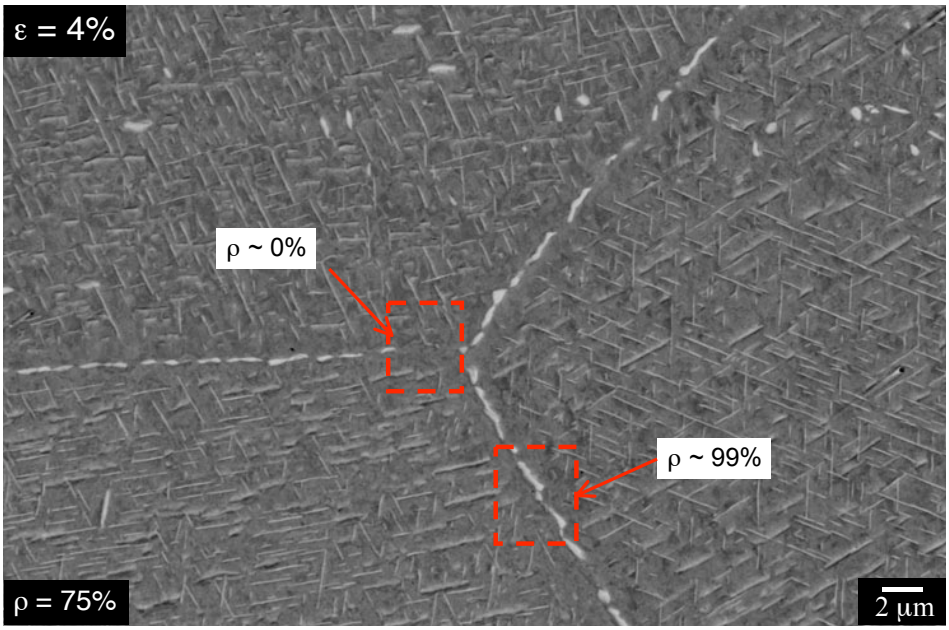

Fig. 5-11 Microstructure of solution treated B-doped steel creep tested at 973K /140 MPa at macroscopic strain of 4%.

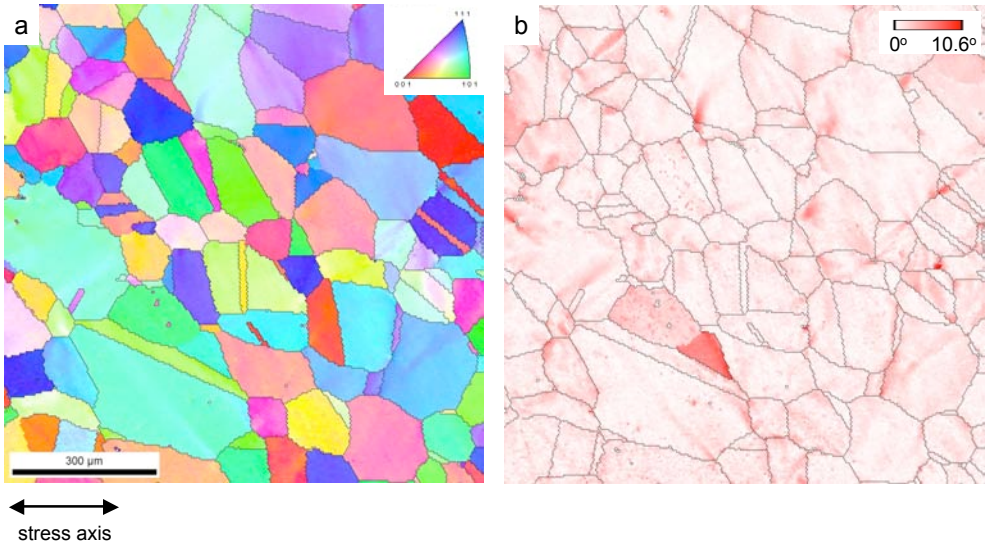

Fig. 5-12 EBSD-OIM analysis of solution treated B-doped steel tested at 973K / 140 MPa at macroscopic strain of 4%: (a) IPF map (b) GROD map.

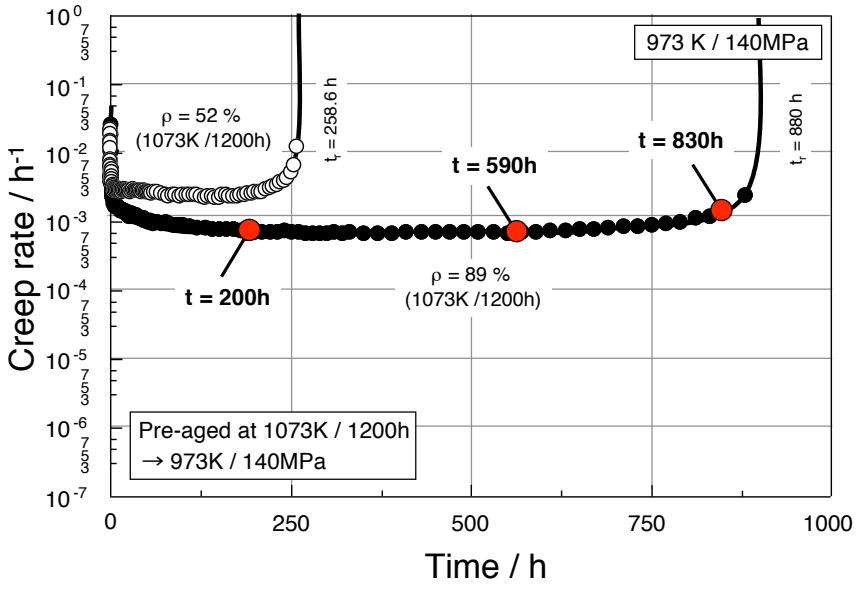

Fig. 5-13 Creep rate time curve of as 1073K/1200h pre-aged B-doped steel tested at 973K / 140 MPa.

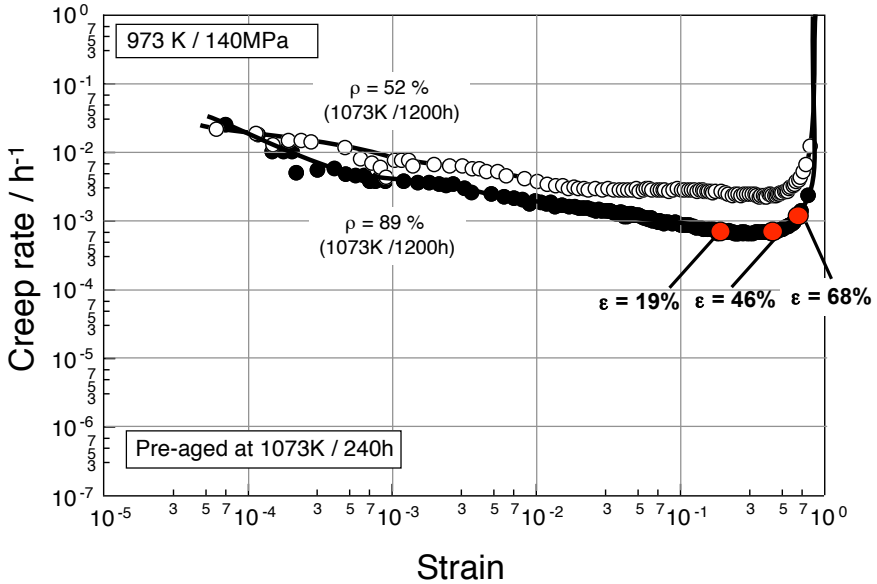

Fig. 5-14 Creep rate strain curve of as 1073K/1200h pre-aged B-doped steel tested at 973K / 140 MPa.

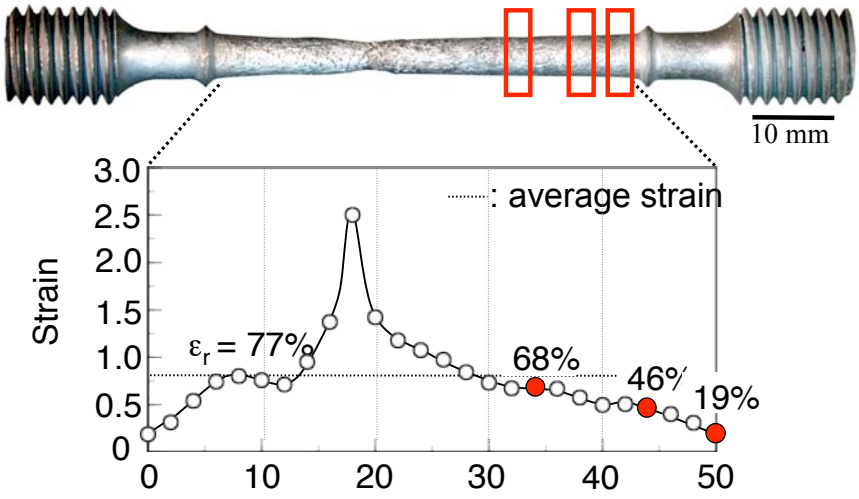

Fig. 5-15 Outlook of fractured 1073K/1200h pre-aged B-doped steel at 973K/140 MPa and variation in macroscopic strain along the gauge length

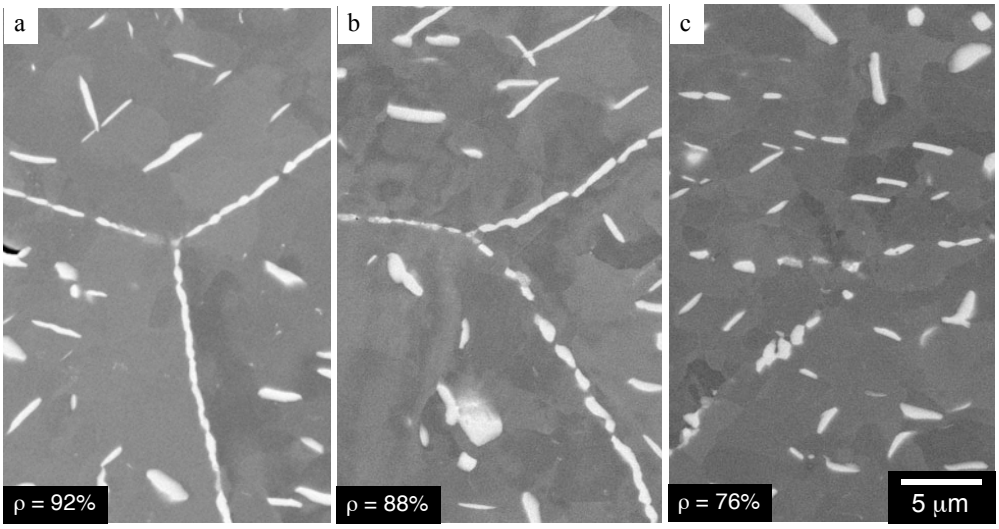

Fig. 5-16 Local microstructures of 1073K/1200h pre-aged B-doped steel after creep tested at 973K / 140 MPa: (a) ε = 19%, (b) ε = 46%, (c) ε = 68%.

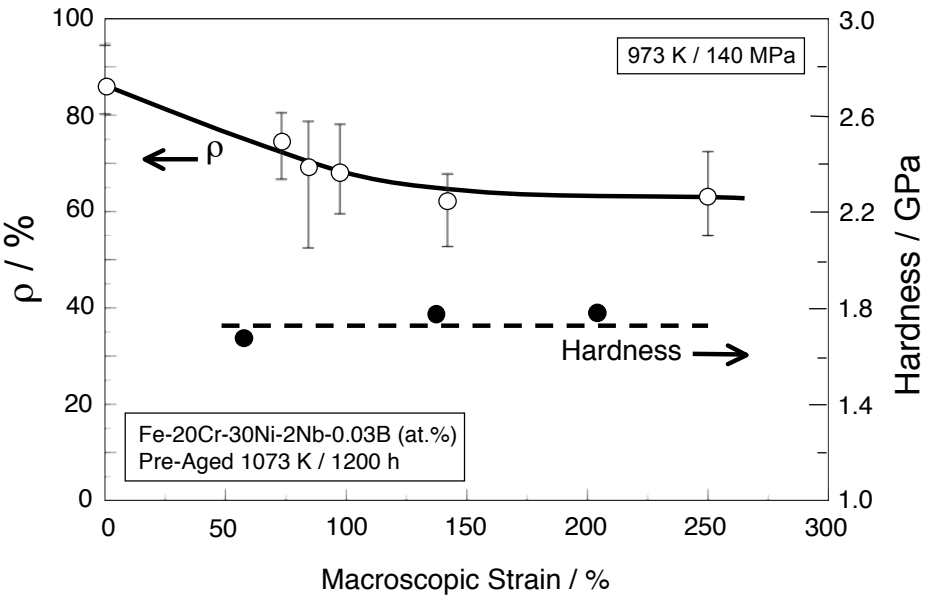

Fig. 5-17 Change in area fraction of hardness with increasing strain in 1073K /1200 h pre-aged B-doped steel creep tested at 973K/140 MPa.

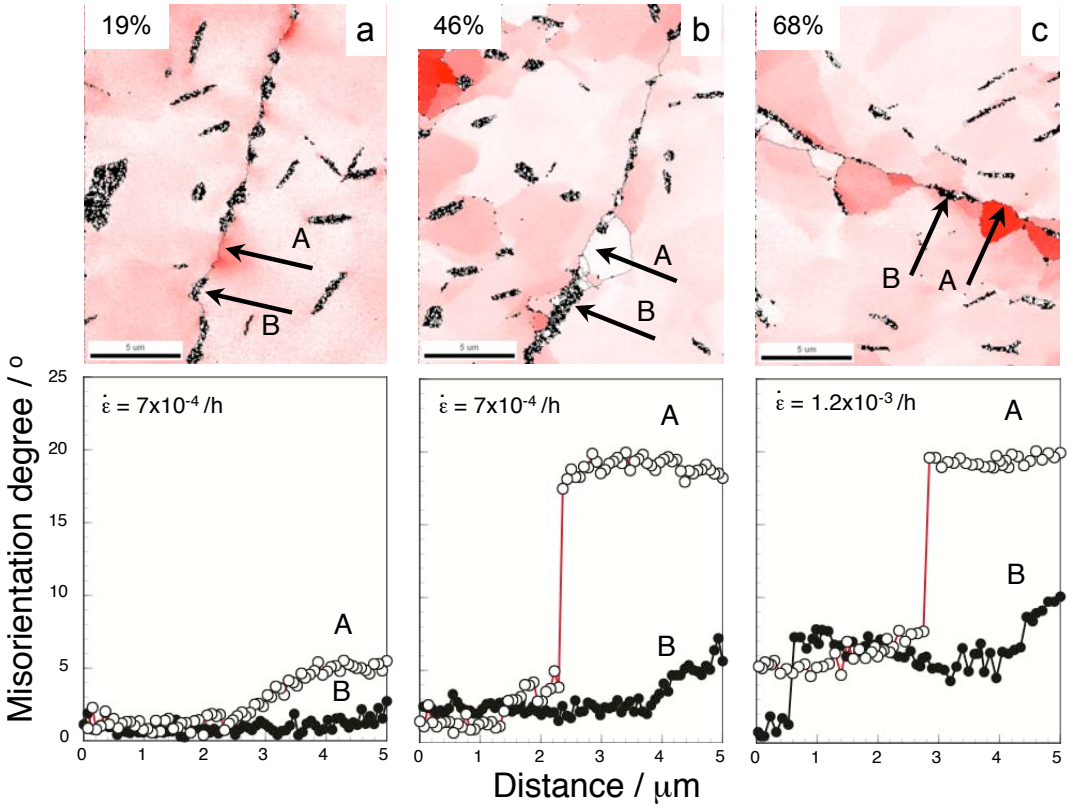

Fig. 5-18 GROD maps and misorientation profiles frrom grain interior to grain boundary (A: G.B. without Laves phase, B: with Laves phase) of 1073K/1200h preaged base steel creep tested at 973K/140 MPa : (a) ε = 19%, (b) ε = 46%, (c) ε = 68%.

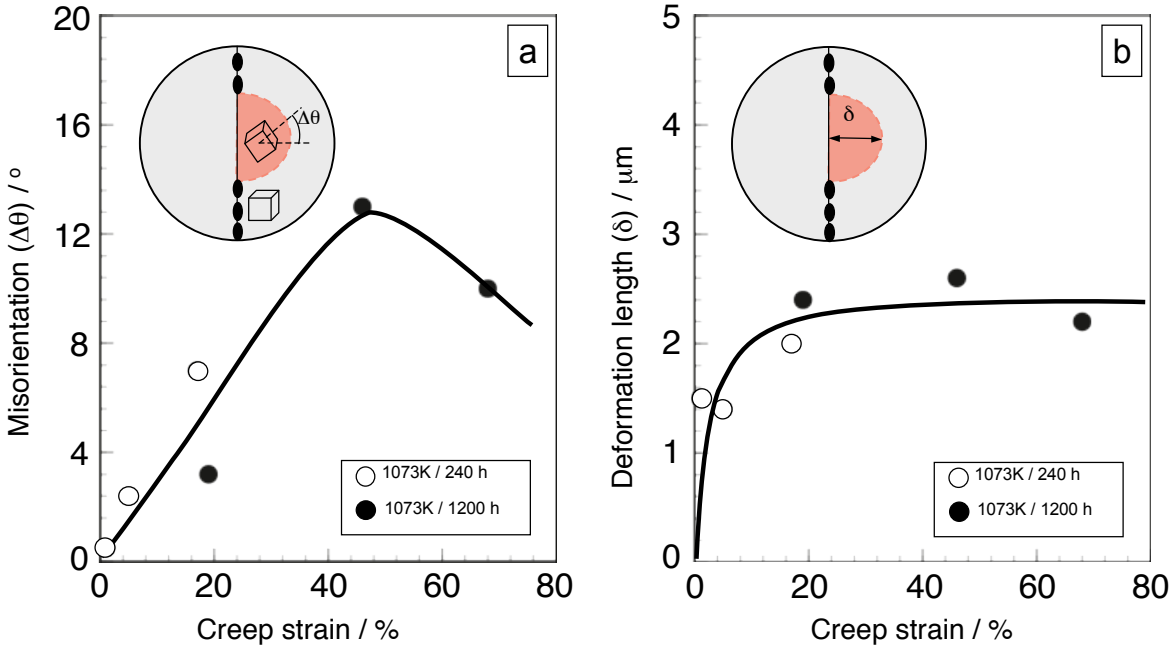

Fig. 5-19 Change in local deformation area with increasing creep strain of 1073 K / 240 h, 1200 h pre-aged B-doped steel creep tested at 1073K / 973 K: (a) misorientation (b) deformation length.

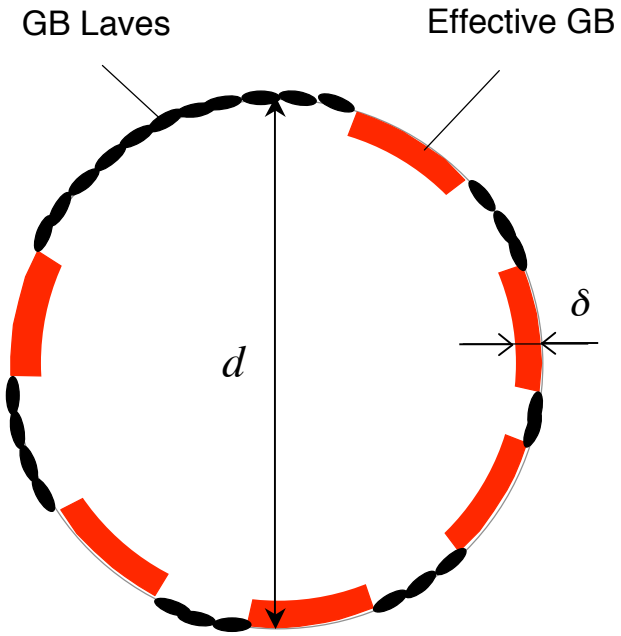

Fig. 5-20 Schematic illustration of the model to estimate strain near the grain boundary.

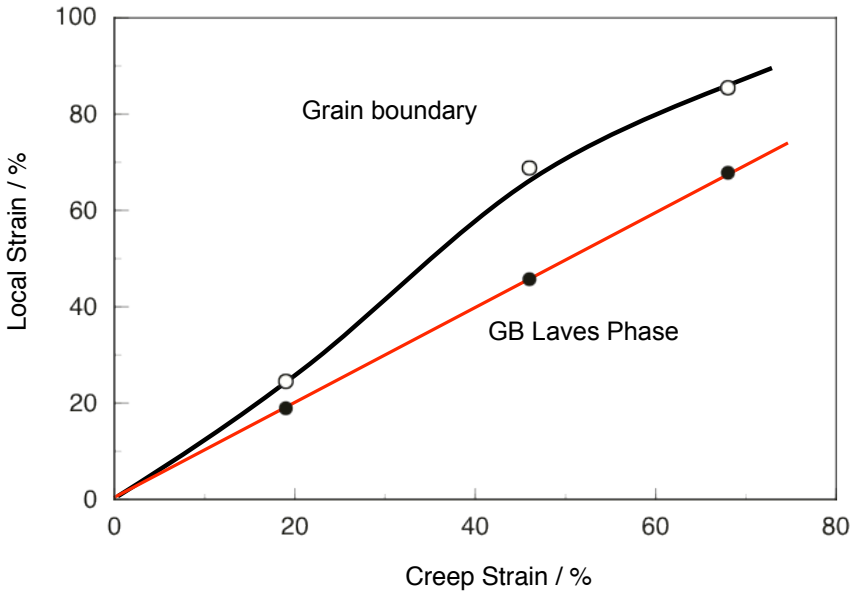

Fig. 5-21 Calculated local strain near grain boundary and GB Laves with increasing creep strain.

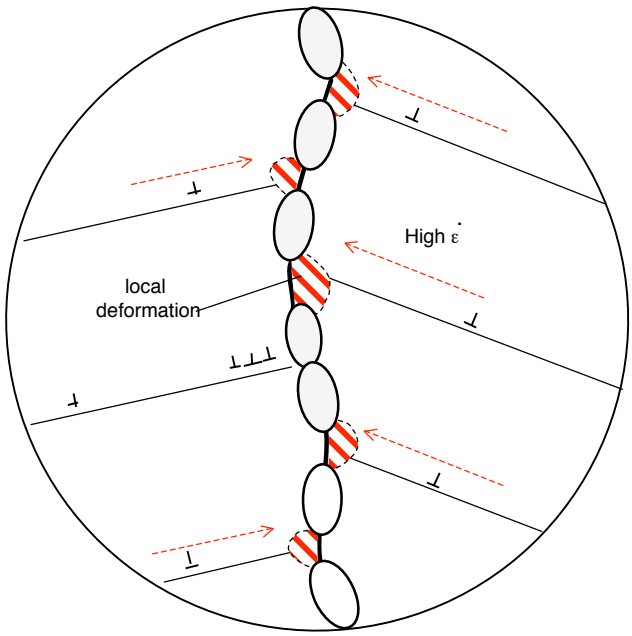

Fig. 5-22 Schematic illustration showing the rate controlling deformation mechanism in the model steel.

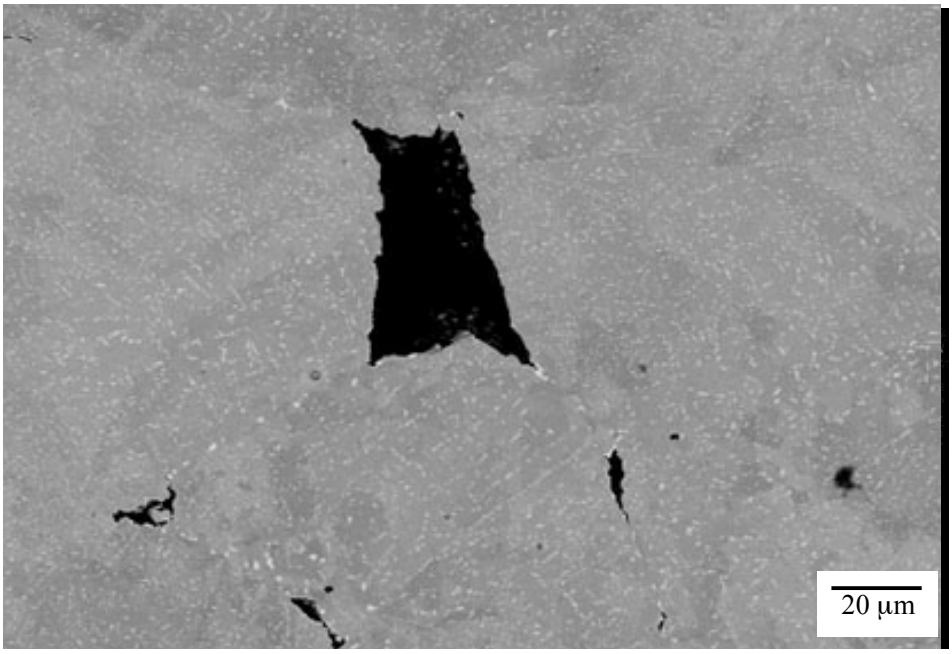

Fig. 5-23Microstructure of ruptured specimen of 1073 K / 240 h pre-aged steel (ρ = 40%) creep tested at 1073 K / 70 MPa

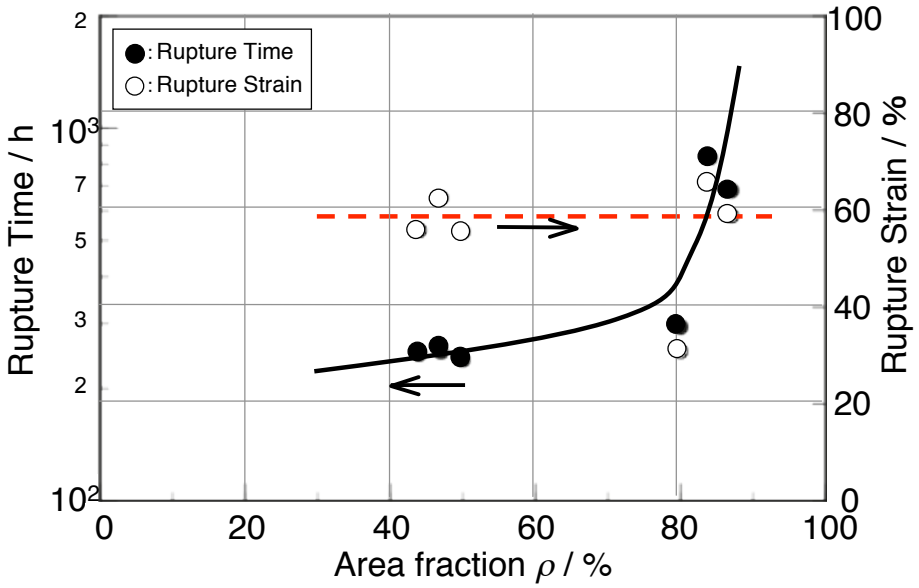

Fig. 5-24 Efffect of GB Laves on creep rupture strength and ductility.

Chapter 6

Application of GBPS Mechanism to Engineering Materials for A-USC Power Plants

6.1 Introduction

In the previous chapters it has been clear that the GB Laves phase is very effective to be used as a strengthener for creep in austenitic heat resistant steels. Increasing the area fraction of GB Laves more than 80% can dramatically improves the creep rupture strength as well as the creep resistance. The strengthening mechanism by GB Laves phase has also been revealed, i.e. it acts as a barrier for dislocation motion in creep, which reduces the creep rate significantly. We have proposed it as "grain boundary precipitation strengthening" (GBPS) mechanism. We have also found that the GBPS can be applied at the accelerating stage, where the GB Laves phase suppress the formation of local deformation area around grain boundary, which we proposed as the main deformation process, and thus extends the creep acceleration stage that leads to much higher creep rupture life.

From the science point of view, the role of GB Laves phase in creep of austenitic heat resistant steel has been clearly revealed. However, the next important question might arise regarding the usefulness of these findings: how could we utilize the knowledge that has been obtained so far for the development of austenitic heat resistant steels?

With regards to this matter, in this chapter we have tried to review the GBPS mechanism from engineering perspective. In the first part we will discuss the effect of combining the GBPS mechanism with the grain interior strengthening by GCP phase, for instance Ni_3Nb-γ" in our model steel. Then, we have proposed the possibility to design a new austenitic heat resistant steels, capable to be used at 1073 K, based on the GBPS mechanism. In the last part, we have tried to propose an idea how to predict a lifetime of austenitic heat resistant steels under the GBPS.

6.2 Role of GCP phase within grain for GBPS

The difference between the concept of GBPS in our model steel and the strengthening mechanism that commonly used in commercial austenitic heat resistant steel is schematically illustrated in **Figure 6-1**. In GBPS, basically we have proposed that the grain boundary design is very important for creep strengthening, since it is the weakest site in the microstructure for creep deformation. Therefore by eliminating the weakening site by means of covering it with stable phase will significantly increase the long-term creep strength. On the other hand, the common practice in designing conventional austenitic heat resistant steel, the metallic carbides are used to strengthen the grain interior. The metallic carbides can significantly increase the creep rupture strength and decreases the creep rate, but it is only for short period of time and limited to temperature below 973 K. At high temperature, carbide is not stable phase and readily coarsens, thus causing the creep strength to drop drastically at long time.

The concept to strengthen the grain interior itself is not a deficient method, since the grain interior has the largest volume fraction within the microstructure. Also, most of dislocation movements at the early stage of creep occur within grain. Therefore, by putting

precipitates at the grain interior can significantly restricts dislocation movements and cause big increase in the creep rupture strength at the early stage. However, in order to utilize this strengthening method effectively, it has to be combined with the grain boundary strengthening, since the dislocations will eventually reach the grain boundary at the long term. It also has been revealed in previous chapter that although the grain boundary only occupies small volume fraction in the microstructures, it becomes the preferential site for creep deformation at the accelerating stage.

In our model steel, at 973 K, both GBPS by the TCP (Topologically Closed Packed) Fe_2Nb-Laves phase and grain interior strengthening by the intermetallics GCP (Geometrically Closed Packed) Ni_3Nb-γ" phase are used. It has been proved to have superior creep rupture strength compared to the conventional austenitic heat resistant steel that only strengthened by metallic carbides within grain. The Ni_3Nb-γ" is effective to increase the creep resistance at the transient stage by reducing the creep rate up to 6 orders of magnitude, while the GB Laves phase significantly improves the creep rupture strength at the acceleration stage.

But unfortunately, the strengthening effect of Ni_3Nb-γ" can only last for several hundreds of hours due to the instability of this phase that readily transforms into coarse Ni_3Nb-δ phase. We have tried to stabilize the precipitation of Ni_3Nb-γ" by adding Zr into our model steel [1]. **Figure 6-2** shows the microstructure of the model steel with 0.1 at. % addition of Zr in comparison to that of the base, after aged at 973 K for 3600 h. At grain boundary, the precipitation of GB Laves phase is the same in both microstructures. However, even after 3600 h of aging, high-density of fine Ni_3Nb-γ" precipitates are still observed in grain interior of Zr-doped steel, while in base steel it has fully transformed into Ni_3Nb-δ phase. This result clearly indicates that small addition of Zr can be used as a tool to stabilize the precipitation of Ni_3Nb-γ" within grain interior. While the mechanism has not yet fully understood, there is indication the addition of Zr reduces the misfit of γ–γ" interface [1, 2]. It might be the reason why the addition of Zr could suppress the transformation of Ni_3Nb-γ" into Ni_3Nb-δ phase.

Based on these results, we have proposed new model steel with composition of Fe-20Cr-30Ni-2Nb-0.1Zr-0.03B, which has been referred to as Combined steel [3]. **Figure 6-3** shows the stress-time to rupture curve of the Combined steel in comparison to that of B-doped and base steels at 973 K. The combined steel has higher creep rupture strength compared to that of B-doped steel and the estimated rupture life at 10^5 h surpasses the requirement of the A-USC power plant. **Figure 6-4** shows the semi-logarithmic plot of creep rate-time curves of combined steel, in comparison to that B-doped and base steel, creep tested at 973 K / 140 MPa. At the transient stage, the creep rate of combined steel decreases up to 3×10^{-7} h^{-1}, which is lower than that of B-doped and base steels. The creep rate of combined steel keep at this minimum value up to 2000 h, while the creep rate of base of B-doped steels have already accelerated after few hundreds hours reaching the minimum. Although the combined steel does not exhibit secondary minimum, the creep

rate of the steel intersects with the second minimum of B-doped steel. The creep rate of combined steel at accelerating stage increases at slower rate compared to the B-doped steel and ruptured at 14281 h, which is longer than that of B-doped steel (9107 h). Interestingly, the combined steel ruptured at strain of 34.9 %, which is more than 3 times longer than that of the base (11.5 %). These results clearly confirm that the stabilization of Ni_3Nb-γ", through the addition of Zr, further increases the creep rupture strength of the steel. The lower slope and the longer accelerating stage of combined steel compared to that of B-doped steel indicates that the grain interior strengthening by GCP phase can be combined effectively with the GBPS. The stabilization of Ni_3Nb-γ" might restrict the dislocations movement around grain interior for longer period of time and thus allowing few dislocations to be able to reach the grain boundary. This will allow more precipitation of GB Laves phase before the deformation at grain boundary finally becomes dominant process. This is the possible reason of the lower slope in the creep accelerating stage of combined steel.

6.3 Design approaches of 1073 K austenitic heat resistant steels using the GBPS mechanisms

The combination of GBPS by TCP Laves phase and grain interior strengthening by GCP Ni_3Nb-γ" phase has been proven to be effective to increase the creep rupture strength at 973 K. By using the same concept, we have tried to challenge to design austenitic heat resistant steel capable to be used at 1073 K. In order to have the same strengthening effect to that at 973 K, the same microstructures have to be obtained at 1073 K, i.e. both GB Laves phase and GCP Ni_3Nb-γ" must precipitate at this temperature. In the current model steel, this is not possible to be achieved since at 1073 K only Laves phase can precipitate. However, from the vertical section of the Fe-20Cr-2Nb-Ni quartenary phase diagram shown in **Fig. 6-5** [4], at 1073 K, the γ + ε + δ three-phase region still exist at around 35 at. % of Ni. It indicates that there is possibility to have precipitation of both TCP Laves phase and GCP Laves phase even at 1073 K.

We have tried to examine the microstructure of the steel with composition of Fe-20Cr-35Ni-2.5Nb (at. %) as shown in **Fig. 6-6** [5]. After aged at 1073 K for 3600 h, the steel shows precipitation of TCP Laves phase at grain boundary, while two types of particles with different sizes precipitate within the grain interior. The Widmanstatten structure of the particles indicates that one of the precipitates at grain interior is GCP Ni_3Nb-δ phase, while the other is most likely the Laves phase. The result proves the feasibility to produce the steel strengthened by both GBPS and grain interior GCP phase at 1073 K.

However, the precipitation on the microstructure shown in **Fig. 6-6** is still coarse and has lower ρ compared to that at 973 K. **Figure 6-7** shows the outlook of the ruptured specimen of the steel with ρ of 40% and 80% after creep tested at 1073 K / 70 MPa. The steel with higher ρ shows fewer cavities around grain boundaries compared to that of lower

ρ steel. It indicates that the GBPS is effective to suppress the cavities formation at 1073 K, which presumably leads to longer rupture life. Therefore the ρ of the proposed steel has to be further increased in order to exhibit the same creep rupture strength to that at 973 K. It needs further research to optimize the microstructure of this steel.

6.4 Life prediction of the Austenitic Heat Resistant Steels under GBPS

In power plant design, it is important to be able to estimate the remaining life of component before failure in order to ensure the safety and sustainability of the operation. In order to predict the life of components, the most reliable way is through microstructure observation. However, the problem is how to input the microstructure factor into the calculation of the residual life?

The most common practice to estimate the rupture life is through stress or temperature accelerated test. However these methods may mislead the assessment in our model steel since the GCP formation is strongly affected by stress [1] and the temperature change may alter the type of precipitates present within the steel. Another factor that has to be considered is that in the model steel change in the local microstructure is the key for deformation process, as described in Chapter 5. Therefore, to utilize the microstructure to predict the rupture life, the observation should be done based on the local microstructure not the bulk.

One of the microstructure factors that have been commonly observed in our model steel, regardless of the type of precipitations, is the formation and evolution of local deformation area near the grain boundary, as described in Chapter 5. Based on these results, the local deformation area could be possibly used as the key parameter for estimating the life of the steel. It has been found that the size and misorientation of local deformation area increase with increasing strain in the steady state stage. However, at the accelerating stage, the size and misorientation of the local deformation area become constant at 2 μm and 20^{O}, respectively. The only parameter that changes with strain is only the number of the local deformation area at this stage. Therefore, by thorough investigation of the change of these parameters with respect to time, it is possible to estimate the rupture life of the steel based on the evolution of local deformation area.

6.5 Summary

The Grain Boundary Precipitation Strengthening mechanism has been reviewed from the engineering perspective. Followings are the conclusions drawn from this chapter:

1) The grain interior strengthening by GCP can further improve the effectiveness of the GBPS by suppressing the dislocation motion at grain interior.
2) The application temperature of the model steel could be extended into 1073 K by using the same strengthening mechanism to that at 973 K.
3) The life prediction of the model steel can be made based on the formation and evolution of local deformation area near the grain boundary.

References

[1] K. Yoshimura: Master Thesis, Tokyo Institute of Technology (2009).

[2] N. Kanno: Master Thesis, Tokyo Institute of Technology (2012).

[3] Y. Misosaku: Master Thesis, Tokyo Institute of Technology (2013).

[4] Y. Hasebe: Master Thesis, Tokyo Institute of Technology (2011).

[5] F. Gao: Master Thesis, Tokyo Institute of Technology (2012).

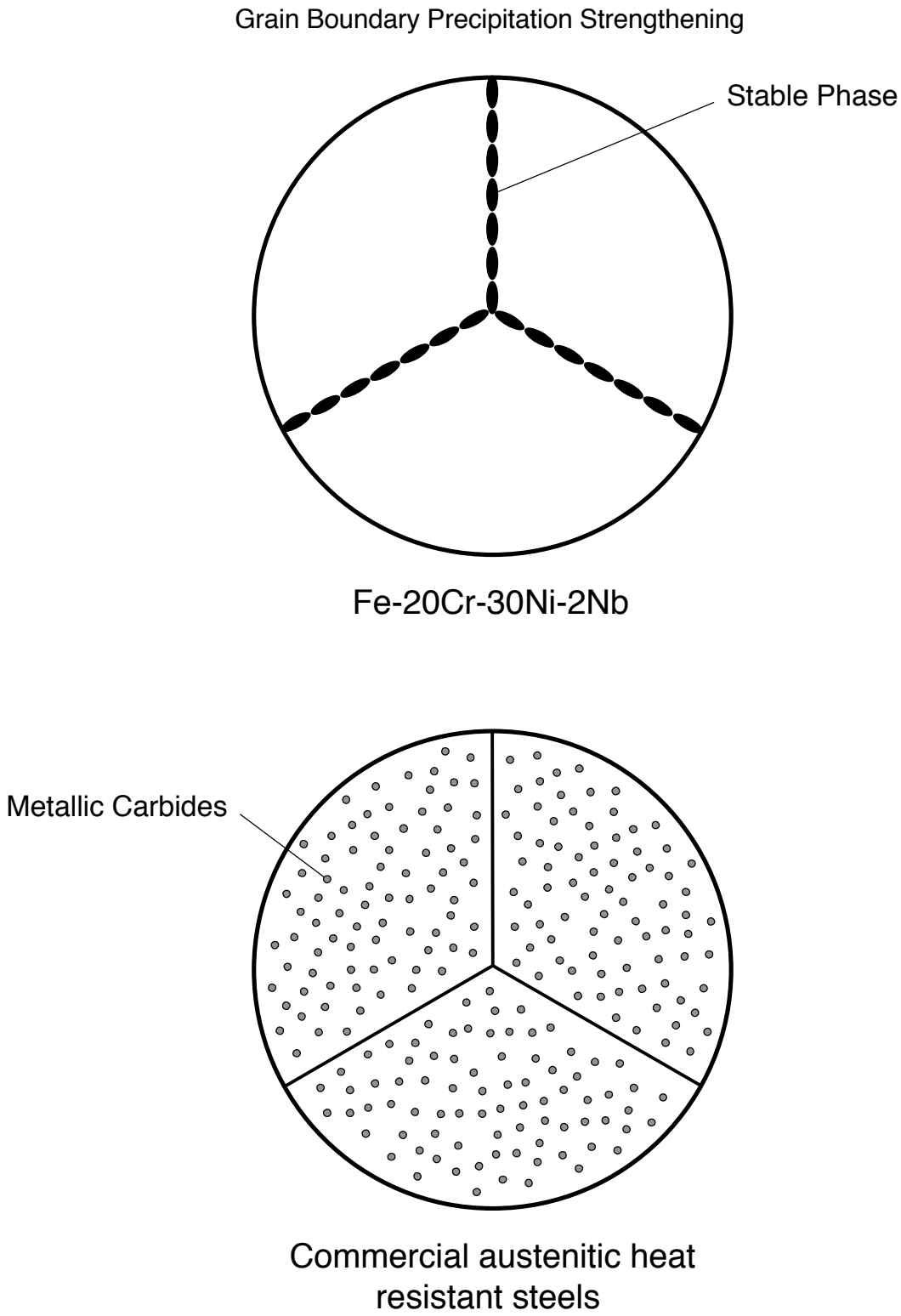

Fig. 6-1 Design concept of GBPS in comparison with commercial austenitic heat resistant steels.

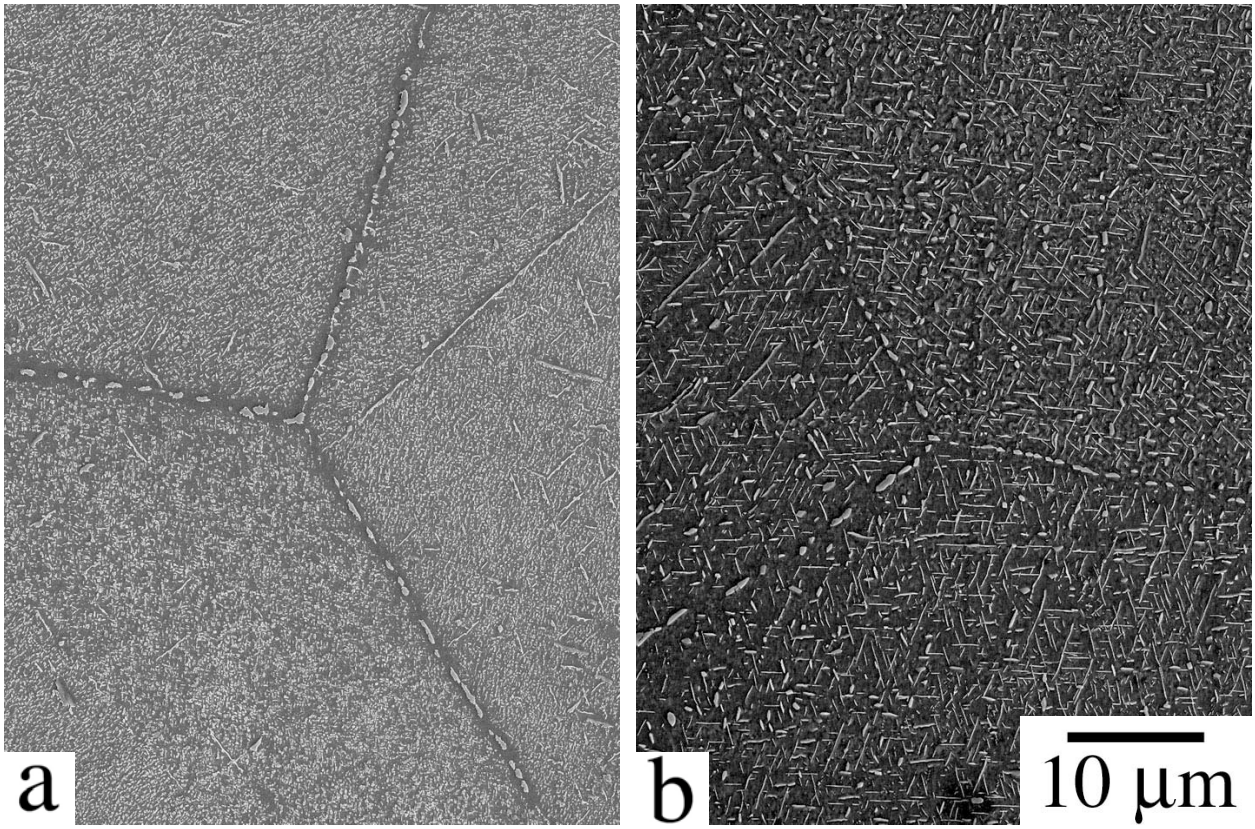

Fig. 6-2 SE images of (a) Zr doped and (b) Base steel aged at 973 K/3600 h.

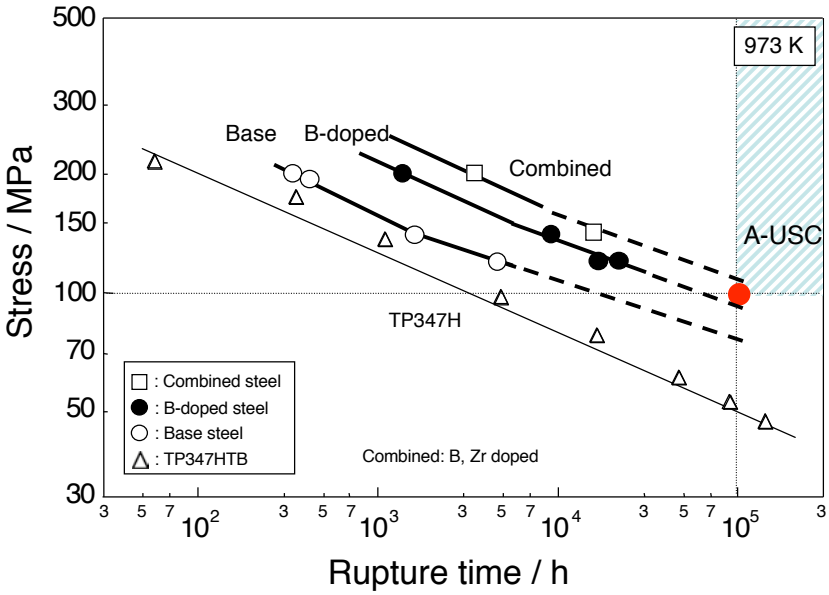

Fig. 6-3 Stress / rupture time curves of solution treated combined, B-dope and base steels in comparison to the commercial heat resistant alloys.

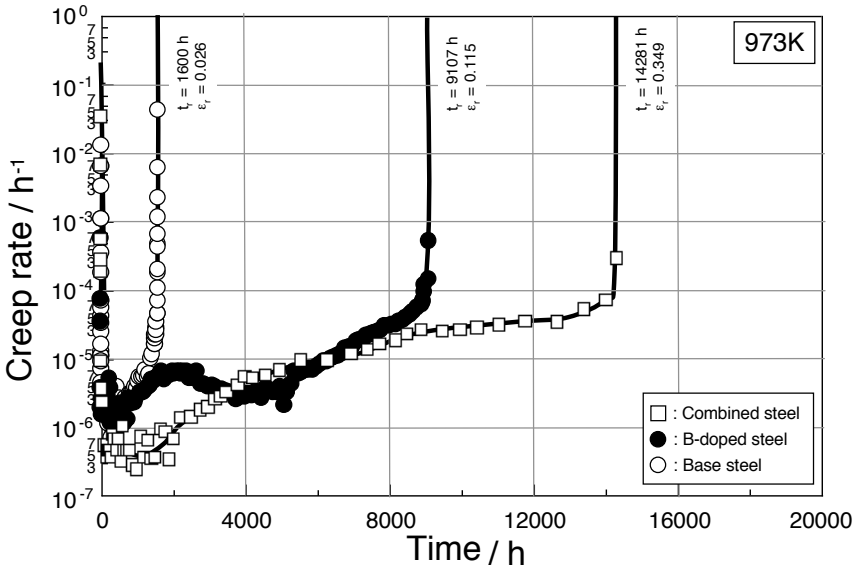

Fig. 6-4 Creep rate / time (linier scale) curves of solution treated combined, B-dope and base steels tested at 973 K / 140 MPa.

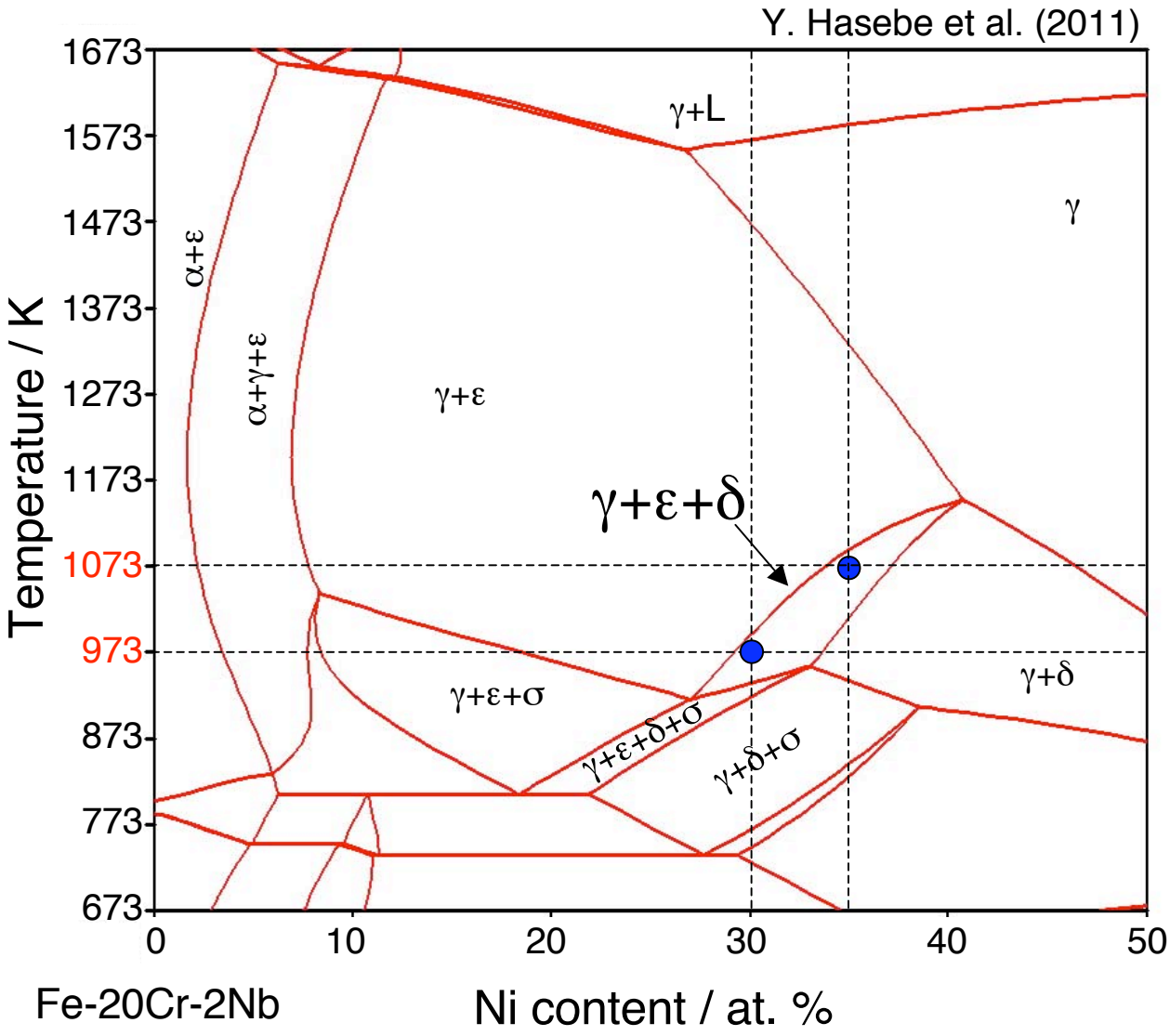

Fig. 6-5 Vertical section of the Fe-Cr-Ni-Nb quaternary system cut along Fe-20Cr-2Nb-Ni. (γ+TCP+GCP) three phase resion exists at 1073 K.

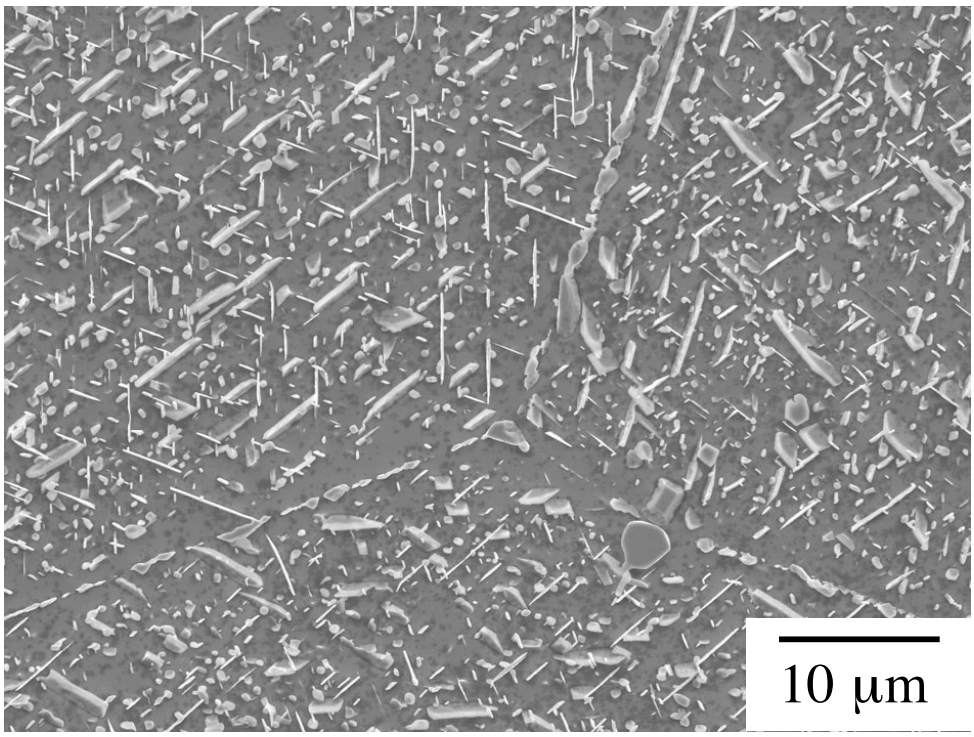

Fig. 6-6 SE images of Fe-20Cr-35Ni-2.5Nb at 973 K/3600 h.

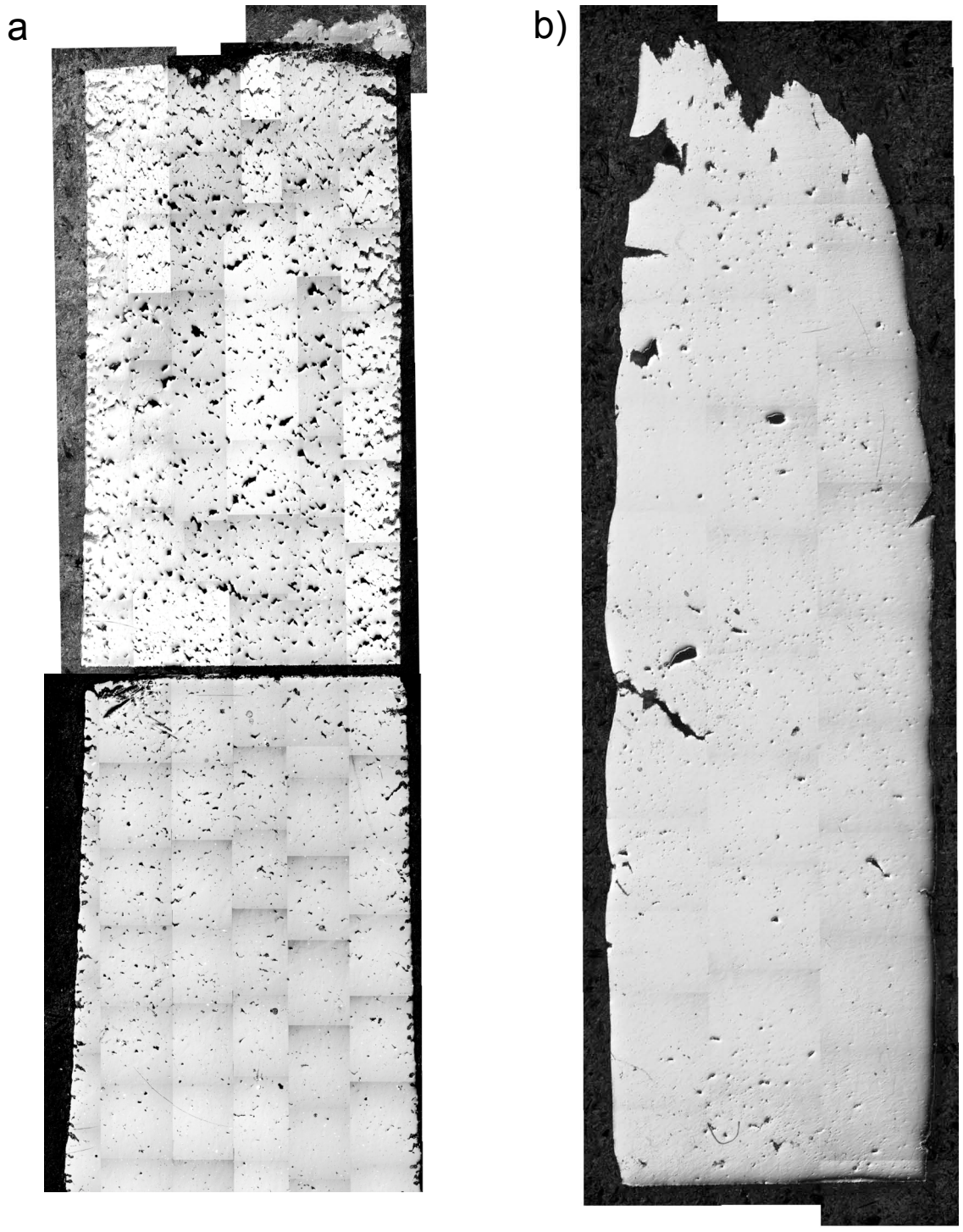

Fig. 6-7 Outlook of the ruptured specimens of 1073K / 240h pre-aged steels creep tested at 1073K / 70 MPa: (a) ρ = 40%, (b) ρ = 80%.

Chapter 7

General Conclusions

7.1 Conclusions

The novel concept for long-term creep strengthening mechanism by TCP Laves Phase in Austenitic Heat Resistant Steels has been proposed in this thesis. Followings are the conclusions obtained in this study:

In Chapter 1: "General Introduction", the superiority of the creep rupture strength of the Fe-20Cr-30Ni-2Nb austenitic heat resistant steel to that of conventional austenitic heat resistant steel has been reviewed. The microstructure observation indicates that the superiority of this steel is due to the grain boundary precipitation strengthening by grain boundary Laves phase. However the mechanism how the GB Laves phase can increase the creep properties has still unknown. Therefore, strategy and objective of this thesis have been outlined

In Chapter 2: "Precipitation Behavior and Morphology Control of Fe_2Nb Laves Phase at Grain Boundary", it has been found that the boron can be used as an effective tool to increase the precipitation of Fe_2Nb Laves phase at grain boundary (GB). The B-doped steel shows higher precipitation of GB Laves phase but lower precipitation density within grain interior compared to that of the base steel. Investigation of the microstructures at various grain boundary angle shows that the boron increases the precipitation kinetics at low angle grain boundary. Furthermore, it has been revealed that the boron does not change the morphology of GB Laves phase.

In Chapter 3: "Effect of GB Laves phase on Creep Behavior", it has been found that the B-doped steel shows higher creep resistance as well as creep rupture strength compared to that of the base steels. The creep tests of B-doped steel at lower stress at 973 K revealed two minimum creep rates that would be related to the enhancement of precipitation of GB Laves phase. It was further revealed that the B-doped steel exhibits lower minimum creep rates than the base steel at 1073 K, where only Laves phase present within the microstructure. This clearly confirms the effectiveness of GB Laves phase in increasing the creep resistance of the present steels.

In Chapter 4: "Creep Strengthening Mechanism by Grain Boundary Laves Phase", it has been found that the creep exponent of the steel is equal to 5 and the creep activation energy is close to that of lattice self-diffusion of γ-Fe, indicating that the creep process is governed by dislocation creep mechanism. The creep rate has been found to decreases with increasing the area fraction of GB Laves phase according to the equation: $\dot{\varepsilon} = \dot{\varepsilon}_o (1-\rho)$, which is proposed as Grain Boundary Precipitation Strengthening Mechanism. The GB Laves phase increases the creep resistance by restricting dislocation motion around grain boundaries.

In Chapter 5: “Role of Grain Boundary Laves Phase on Deformation Mechanism at Accelerating Stage”, it has been found that local deformation area with high misorientation occurs on grain boundary are uncovered by Laves phase. The local deformation area exhibits much higher creep rate than other sites in the microstructures and thus become the controlling rate of overall creep rate. The creep rupture strength significantly increases by protecting more than 80 % of the grain boundary area with Laves phase. The GBPS mechanism can be extended into the accelerating stage by considering the local microstructure change.

In Chapter 6: “Application of GBPS Mechanism to Engineering Materials for A-USC Power Plants”, it has been found that the grain interior strengthening by GCP can further improve the effectiveness of the GBPS by suppressing the dislocation motion at grain interior. The application temperature of the model steel could be extended into 1073 K by using the same strengthening mechanism to that at 973 K. The life prediction of the model steel can be made based on the formation and evolution of local deformation area near the grain boundary.

In Chapter 7: “General Conclusions”, conclusions obtained from each Chapter has been summarized. In addition, possible future works of this study has been proposed.

7.2 Future Works

Although the mechanism and application of Grain Boundary Precipitation Strengthening has been clearly investigated, there is still remaining question regarding the effect of the grain size. Supposed that the grain size is decreased but the area fraction of GB Laves phase is the same, what is the effect on the creep behavior of the steel? Based on our model, decreasing the grain size will increase the local strain around grain boundary, and therefore increase the creep rate. However, we need further research to observe about the actual effect of grain size on the GBPS. Therefore, this study can be extended by comparing the creep behavior of the steels with different grain size but the same ρ.

Acknowledgement

First of all, I would like to thank to my supervisor, Professor Masao Takeyama, for his encouragement, guidance and support throughout my study in Doctoral course. I am really grateful for his kind concern regarding my attitude toward research and also the opportunity that he gave me to study in his lab. I really appreciate his continuous effort and persistence to encourage me to go through all the difficulties that I had experienced during my study. I do not think I cannot thank him enough for all his help and chance that he has given to me. I really hope I can return his kindness in the future.

Assistant Prof. Naoki Takata, for his patience and unfailing support to complete this study. I really appreciate his valuable assistance and advice in completing my doctor thesis. I am very sorry for putting you in troubles so many times.

Taga-san, for her patience and encouragement during my difficult time. Thank you very much for all your kindness. I am sorry for all the troubles I made. I promise to become a better person and not easily give up in facing my problems in the future.

I am indebted to many of my colleagues who help me preparing this thesis: Taro, Iwasaki, Kimura for their unselfish and untiring support in preparing figures. Hashizume-san, Kurata-san, Misosaku, Zhang, Gao who provides beautiful data for my thesis. Ishikawa-san for his kind advice and help regarding my analysis. This thesis would have remained a dream had it not been for their kind support.

I also would like to express my gratitude to all my fellow students in Takeyama laboratory who I cannot describe one by one. Thank you very much for the friendship and help during my study. I am sorry for all the troubles and ignorance that I did during my last year of doctor course. I really hope to talk with all of you more if my condition allows. Wish you all the best for your future researches.

All of my friends in GIII-Tokyo for the fellowships and the prayer that strengthened me up to this point.

Last but not the least, my parents, families and the one above all of us, Jesus Christ, for giving me the strength and patience to keep moving forward through the hard times, thank you so much Dear Lord.

March, 2014

Imanuel Tarigan